

**NEW MRI CONTRAST AGENTS THROUGH SPIN EXCHANGE
OPTICAL PUMPING OF NOBLE GASES WITH A NUCLEAR
ELECTRIC QUADRUPOLE MOMENT**

JOSEPH STEVEN SIX

**Thesis submitted to the University of Nottingham
for the degree of Doctor of Philosophy**

July 2014

Abstract

Hyperpolarized ^{83}Kr has previously demonstrated MRI contrast that is sensitive to the chemical composition of the surface in a porous model system. One-dimensional nuclear magnetic resonance spectroscopy of hyperpolarized ^{83}Kr has also revealed distinctive longitudinal relaxation times from selected regions of an ex vivo rat lung originating from differences in surface to volume ratio. However, at the time, MRI using longitudinal relaxation for contrast was not attempted due to limited signal intensities.

Methodological advances of the spin exchange optical pumping process have led to a substantial increase in the ^{83}Kr hyperpolarization and the resulting signal intensity. This methodology originates from a below-ambient pressure hyperpolarization technique explored and developed in this work. Using the improved methodology for spin exchange optical pumping of isotopically enriched ^{83}Kr has resolved anatomical details of ex vivo rodent lungs using hyperpolarized ^{83}Kr MRI for the first time. Different ^{83}Kr longitudinal relaxation times were found between the main bronchi and the parenchymal regions of the lung. The T_1 weighted hyperpolarized ^{83}Kr MRI provided the first demonstration of surface quadrupolar relaxation pulmonary MRI contrast.

Novel hyperpolarization techniques of ^{129}Xe have also been explored resulting a study into the combustion process of methane. Using ^{129}Xe as a probe into the combustion process permitted the first in situ MRI of combustion and enabled spatial-velocity profiles.

Relevant publications

[1] J.S. Six, T. Hughes-Riley, D.M.L. Lilburn, A.C. Dorkes, K.F. Stupic, D.E. Shaw, P.G. Morris, I.P. Hall, G.E. Pavlovskaya, T. Meersmann, Pulmonary MRI contrast using Surface Quadrupolar Relaxation (SQUARE) of hyperpolarized ^{83}Kr , *Magnetic Resonance Imaging*, 32 (2014) 48-53.

[2] T. Hughes-Riley, J.S. Six, D.M.L. Lilburn, K.F. Stupic, A.C. Dorkes, D.E. Shaw, G.E. Pavlovskaya, T. Meersmann, Cryogenics free production of hyperpolarized ^{129}Xe and ^{83}Kr for biomedical MRI applications, *Journal of Magnetic Resonance*, 237 (2013) 23-33.

[3] D.M.L. Lilburn, T. Hughes-Riley, J.S. Six, K.F. Stupic, D.E. Shaw, G.E. Pavlovskaya, T. Meersmann, Validating Excised Rodent Lungs for Functional Hyperpolarized Xenon-129 MRI, *PLoS ONE*, 8 (2013) e73468.

[4] K.F. Stupic, J.S. Six, M.D. Olsen, G.E. Pavlovskaya, T. Meersmann, Combustion resistance of the Xe-129 hyperpolarized nuclear spin state, *Phys. Chem. Chem. Phys.*, 15 (2013) 94-97.

[5] J.S. Six, T. Hughes-Riley, K.F. Stupic, G.E. Pavlovskaya, T. Meersmann, Pathway to Cryogen Free Production of Hyperpolarized Krypton-83 and Xenon-129, *PLOS ONE*, 7 (2012) e49927.

Acknowledgements

There are many people who have contributed greatly to this work, either through direct assistance in the experiments or through encouragement and moral support. I would like to start by acknowledging my supervisor Thomas Meersmann for his hard work and guidance the past three years. I am greatly indebted to my fellow postgraduate students with whom I have spent many late nights and early mornings in the laboratory. I specifically would like to thank Karl Stupic for his training and patience when I was first learning the concepts of spin exchange optical pumping and how to use the equipment in the laboratory. Theodore Hughes-Riley deserves the deepest thanks for working with me on projects, editing manuscripts, and for the stimulating conversations we had about Britain's magnificent history in order that I understand some of the *finer things* in life. I appreciate David Lilburn for his friendship and straightforward honest attitude that has helped significantly in facing life's trials the past three years. I also want to thank Clémentine Lesbats and Mathieu Baudin for their assistance in experiments and camaraderie in the laboratory. Thanks to Galina Pavlovskaya for teaching me the fundamentals of writing magnetic resonance imaging pulse programs, using our data analysis software, and other helpful discussions. I appreciate the work of my co-supervisors Ian Hall and Peter Morris for their vital feedback throughout the course of this

degree. Special thanks to Robert Chettle, Clive Dixon, Mike Olsen, Ian Taylor, and particularly Alan Dorkes for the fabrication of specialized glassware and equipment used in this work. I would also like to thank Simon, Ed and Ben for their Thursday morning radio show (which at the moment of writing has been changed to Tuesday).

On a personal note, I am sincerely grateful for my wife Marcella who is and always will be the joy of my life. I hope that over the next several decades I can love and support her as much as she has already loved and supported me. I also want to thank my family across the Atlantic Ocean on the far side of the North American continent for always being supportive of my time here in Nottingham.

Table of contents

	Page
Abstract	ii
Relevant publications	iv
Acknowledgements	v
Chapter 1: Introduction	1
1.1 Motivation	1
1.2 Lung MRI using hyperpolarized noble gases	2
1.2.1 Imaging using ^3He and ^{129}Xe	2
1.2.2 Hyperpolarized ^{83}Kr MRI	6
1.3 Aims of this work	12
1.4 References	13
Chapter 2: Background and theory	17
2.1 Purpose of chapter	17
2.2 Introduction to Nuclear Magnetic Resonance	18
2.2.1 Nuclear spin in a magnetic field	18
2.2.2 Signal and population distribution at thermal equilibrium	23
2.2.3 Hyperpolarization through spin exchange optical pumping	26
2.2.4 Relaxation mechanisms	33
2.2.4.1 Longitudinal relaxation	34
2.2.4.2 Transverse relaxation	35
2.2.5 Systems with spin $> 1/2$	38
2.3 Concepts of Magnetic Resonance Imaging	42
2.3.1 Spatial encoding	42
2.3.2 Gradient echo imaging	43

2.3.3	Non-equilibrium imaging (variable flip angle)	45
2.4	References	47
Chapter 3:	Pathway to cryogen-free production of	51
	hyperpolarized ^{83}Kr and ^{129}Xe	
3.1	Introduction	51
3.2	Experimental	54
3.2.1	Stopped flow spin exchange optical pumping	54
3.2.2	Laser power adjustment and optical measurements	56
3.2.3	Temperature control	57
3.2.4	Gas mixtures	58
3.2.5	Determination of obtained polarization values	58
3.2.6	Accuracy of polarization measurements	59
3.2.7	Data analysis	60
3.3	Background to the ^{83}Kr and ^{129}Xe SEOP experiments	61
3.3.1	Expected pressure dependence	61
3.3.2	Contribution of rubidium-rubidium collisions	63
3.3.3	Radiation trapping	65
3.3.4	Rubidium depolarization caused by spin-rotation interactions	66
3.3.5	Spin exchange rate	68
3.4	Results and discussion	69
3.4.1	Noble gas polarization as a function of SEOP gas pressure	69
3.4.2	Spin exchange optical pumping temperature	75
3.4.3	Results from inversion recovery ^{83}Kr SEOP experiments	76
3.4.4	^{83}Kr polarization as a function of SEOP pressure	86
3.4.5	Result from inversion recovery ^{129}Xe SEOP experiments	87
3.4.6	^{129}Xe polarization as a function of SEOP pressure	89

3.4.7	Non-linear pressure broadening of the rubidium D ₁ absorption linewidth	91
3.4.8	Non-linear pressure broadening of the rubidium D ₁ absorption linewidth	95
3.4.9	Effect of laser power and laser linewidth	97
3.4.10	Rapid decrease of polarization with decreasing pressure below P ^{max}	101
3.5	Conclusions	103
3.6	References	106
Chapter 4: Pulmonary MRI contrast using surface quadrupolar relaxation of hyperpolarized ⁸³Kr		111
4.1	Introduction	112
4.2	Materials and methods	114
4.2.1	⁸³ Kr spin exchange optical pumping	114
4.2.2	Hyperpolarized gas extraction, compression and transfer	116
4.2.3	Hyperpolarized gas inhalation	119
4.2.4	MRI protocol	119
4.2.5	Image reconstruction and analysis	120
4.2.6	Animal care and preparation	121
4.3	Results and discussion	122
4.4	Conclusion	129
4.5	References	132
Chapter 5: Diffusion of ¹²⁹Xe and ⁸³Kr through internal magnetic field gradients		135
5.1	Introduction	135
5.2	Background	136
5.3	Transverse relaxation of ¹²⁹ Xe in a single pore	142
5.3.1	Materials and methods	142
5.3.1.1	¹²⁹ Xe spin exchange optical pumping	142
5.3.1.2	CPMG experiments	143
5.3.1.3	Data analysis	144
5.3.2	Results and discussion	145

5.4 Transverse relaxation of ^{129}Xe and ^{83}Kr in porous media	152
5.4.1 Materials and methods	152
5.4.1.1 Animal care and preparation	152
5.4.1.2 Preparation of glass beads	153
5.4.1.3 Animal care and preparation	154
5.4.1.4 CPMG experiments	155
5.4.1.5 Data analysis	155
5.4.2 Results and discussion	156
5.4.2.1 Transverse relaxation of ^{129}Xe in glass beads	156
5.4.2.2 Transverse relaxation of ^{83}Kr in glass beads	163
5.4.2.3 Transverse relaxation of ^{129}Xe and ^{83}Kr in ex vivo rat lungs	165
5.5 Conclusions	166
5.6 References	170
Chapter 6: In situ MRI of combustion	173
6.1 Introduction	173
6.2 SEOP of fuel-xenon mixtures	175
6.3 In situ MRI of combustion	183
6.4 References	193
Chapter 7: Conclusions	195
7.1 References	202

Chapter 1: Introduction

1.1 Motivation

There has been limited development in the diagnoses and treatment of pulmonary diseases in the past few decades. The lack of advancements can be seen in the prevalence of respiratory conditions, which in 2001 were found to be three of the top five causes of death in high-income countries [1]. Furthermore, respiratory related deaths are currently on the rise. For example, the prevalence of chronic obstructive pulmonary disease (COPD) has increased in the United Kingdom [2] and the United States of America [3], and is projected to become the third leading cause of death worldwide by 2020 [4].

One reason that the prevalence of lung diseases is increasing stems from the delicate nature of the organ. The lung maintains a balance of maximizing the surface area, for gas exchange during respiration, while minimizing supporting tissue to efficiently utilize limited space [5]. Disruptions to this balance leads to a multitude of conditions that are known to affect the lungs, airways, and breathing processes making the organ prone to various diseases of numerous origins. Major contributing factors to lung diseases, including but not limited to COPD, are subject to environmental influences such as inhalation of tobacco smoke [6] which is increasing in many developing nations [7]. Additionally, the global decline of deaths related to infections has led to an increase in chronic diseases, such as COPD, which develop gradually and are increasingly prevalent in the aging world population [4, 8-10].

With the growing prevalence of lung related diseases, improved tools to diagnose and evaluate progression of the diseases are necessary. Unfortunately the most developed imaging techniques for evaluating lung function involve ionizing radiation in scintigraphy (and other techniques that require the use of a radionuclide such as single-photon emission computed tomography and positron emission tomography) or high-resolution X-ray computed tomography. The invasive natures of these imaging modalities prevent prolonged studies that can track disease progression. Therefore, diagnoses and treatment of respiratory diseases such as COPD, asthma, and pulmonary fibrosis could greatly benefit from the existence of an accurate biomarker that does not require harmful ionizing radiation to observe not only disease progression but also the legitimacy of drug administration.

1.2 Lung MRI using hyperpolarized noble gases

1.2.1 Imaging using ^3He and ^{129}Xe

Magnetic resonance imaging (MRI) is a possible non-invasive tool to explore pulmonary diseases. However, conventional MRI of the pulmonary system is challenging because low proton density in the lung [11]. Very short relaxation times caused by magnetic field variations at the air-tissue interface also strain common imaging techniques [12-14]. Continued effort to overcome the fast relaxation has greatly improved image quality [11, 15, 16], however, the fundamental problem comes from the fact that conventional proton MRI cannot image the airspaces in the lung [17]. An alternative method has been developed where a noble gas is inhaled into the lung and the gas itself is imaged; this requires hyperpolarization techniques that increase MRI signal intensity of the gas before inhalation. Hyperpolarized ^3He [18] and hyperpolarized ^{129}Xe [19] are possible contrast

agents that allow for resolved measurement of lung ventilation and function through various MRI protocols.

The use of hyperpolarized noble gases for pulmonary MRI enables high-resolution ventilation images. Improvements in signal intensities are apparent in Figure 1.1 where the image of hyperpolarized ^3He (Figure 1.1A) reveals significant lung structure and the conventional proton image has limited information of the region (Figure 1.1B).

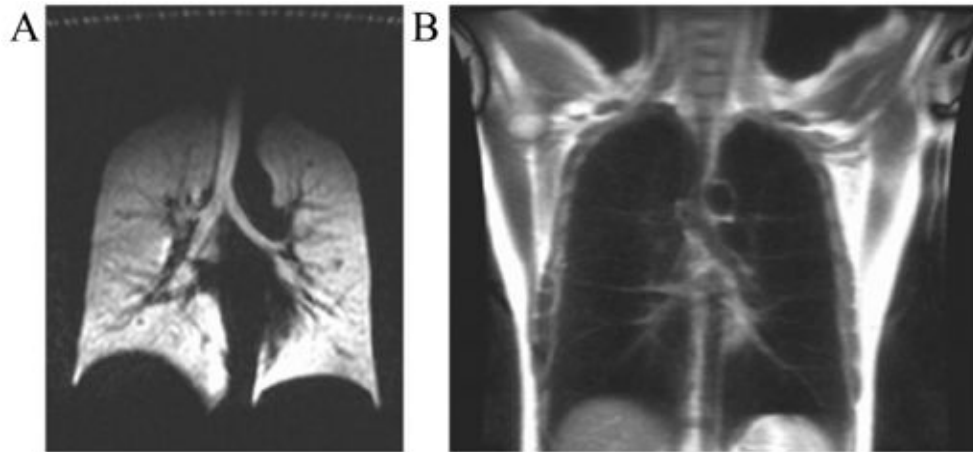


Figure 1.1. Comparison between (A) a hyperpolarized ^3He image and (B) a conventional proton image. Figure courtesy of ref. [20].

Ventilation images have helped with understanding lung structure and reveals ventilation defects in advanced stages of pulmonary diseases [21-23] but struggle to provide justification for wide spread implementation over commonly performed, much less expensive, spirometric tests for lung function. Therefore, the development of hyperpolarized noble gases is not solely the pursuit of higher signal intensities that lead to higher resolution ventilation images but also a search for techniques that acquire additional functional information from the lung.

One method to extract functional information is to exploit the high diffusivity of ^3He for contrast relating to abnormalities in alveolar lung structure by observing the apparent diffusion coefficient (ADC) [24-27]. ADC measurements probe the distance that ^3He can diffuse over the acquisition time by observing transverse relaxation that occurs from the movement of ^3He in an externally applied (pulsed) magnetic field gradient. The root mean square distance that the atom may freely move along a single axis is determined by the diffusion coefficient (D) and the time allowed for diffusion (t) as shown by $\Delta X = \sqrt{2Dt}$. In the case of restricted diffusion, where the characteristic length of the container (i.e. the size of the pore) is less than ΔX , collisions with the pore wall reduce the permitted diffusion thereby measuring the effective diffusivity (*apparent diffusion*). Human lungs are a system with restricted diffusion for ^3He and ADC can probe the alveolar size and gain insight into the network of alveolar ducts [24]. This technique is useful for lung diseases such as emphysema where the altered alveoli architecture can be observed [24, 28, 29] and quantified [30]. A spin-tagging method [31] may be used to further increase the distance that can be probed by ^3He allowing measurement of convection during inhalation and exhalation.

In addition to ADC experiments, ^3He can investigate lung function through partial pressure measurements of pulmonary oxygen [32-34]. These measurements are possible because longitudinal relaxation of ^3He in the presence of O_2 is well understood [35] and O_2 is the principal cause for ^3He relaxation in lung imaging experiments [36]. Spatially resolved determination of the ^3He longitudinal relaxation rate can be used to generate

pO_2 (partial pressure of O_2) maps and subsequently determine the rate of O_2 uptake. The presence of paramagnetic O_2 affects 3He spin relaxation more than that of any of the other noble gas isotopes making it the best candidate for O_2 relaxation measurements. It is worthy to note that this technique is imperfect in patients with COPD because delayed ventilation in the seriously diseased regions during a breath hold causes unreliable results in these areas [37].

Unfortunately 3He occurs naturally in trace quantities: only 1.38 parts per million (0.000138%) of total natural helium. The primary source of 3He is currently its manufacture through tritium decay in nuclear fusion limiting its supply [38]. Furthermore, 3He has a number of useful applications beyond hyperpolarized noble gas imaging leading to a supply crisis that has been discussed in congressional hearings of the United States of America [39].

As a substitute for 3He , ^{129}Xe has a natural abundance 26.4% of all xenon and is isolated using air liquefaction and isotopic enrichment. In fact the first demonstration of hyperpolarized noble gases for pulmonary imaging was completed using ^{129}Xe [19]. However, 3He quickly became the isotope of choice because of greater inherent signal intensity and efficient hyperpolarization techniques developed more quickly. The supply crisis of 3He has rejuvenated interest in hyperpolarized ^{129}Xe for pulmonary imaging. Hersman and colleagues have recently developed a ^{129}Xe hyperpolarizer that achieve spin-polarization levels and quantities comparable to 3He [40]; however, substantial monetary investment is required. Even with similar spin-polarization levels to 3He , there are a number of challenges and

potential opportunities using hyperpolarized ^{129}Xe for pulmonary imaging due to the physics governing the behavior of the isotope.

The first challenge to overcome is that ^{129}Xe has a higher atomic mass than ^3He limiting the diffusion of the atom, when present in dilute quantities within air, to about 1/6 of ^3He [41] for ADC measurements. The limited diffusion hinders studies involving large diffusion distances such as the peripheral airways in severely emphysematous lungs [42]. However, it may be possible to investigate larger distances using a spin-tagging method as done with ^3He [31]. Preclinical [43, 44] and recent clinical [45-47] studies have demonstrated the feasibility of ^{129}Xe ADC measurements as research focus shifts from ^3He to ^{129}Xe [48].

A second challenge is that xenon readily dissolves in the tissue of the lung and enters the blood stream behaving as an anesthetic and limiting the amount of xenon that can be administered to a patient during experiments. This challenge may lead to the greatest opportunity for ^{129}Xe in pulmonary imaging because ^{129}Xe possesses a large chemical shift range arising from strong interactions with the environment that can be exploited to distinguish between gas phase xenon, xenon dissolved in tissue, and xenon dissolved in blood [49]. Chemical shift selective techniques enable the measurement of gas perfusion through the parenchyma [50] and allows ^{129}Xe to probe lung function in diseases such as fibrosis where gas uptake is affected due to thickening of the alveolar walls [51].

1.2.2 Hyperpolarized ^{83}Kr MRI

A possible alternative to ^3He and ^{129}Xe to observe functional information of the lung may exist in using hyperpolarized noble gases that

have a nuclear electric quadrupole moment (i.e. ^{21}Ne , ^{83}Kr , ^{131}Xe). The nuclear electric quadrupole moment serves as a probe for electric field gradients (EFGs) that are generated during brief collision and adsorption events between the noble gas atoms and the surrounding surfaces. These interactions result in longitudinal relaxation that can be detected in the gas phase. By probing the properties of the lung surface it may be possible to investigate the lung in a manner inaccessible to ^3He and ^{129}Xe (this will be discussed in greater detail in *section 2.2.5* of Chapter 2). However, the nuclear electric quadrupole moment limits the hyperpolarization of these isotopes making high-resolution ventilation images unlikely.

Previous studies have shown that the longitudinal relaxation of ^{83}Kr demonstrates MRI contrast specific to the surface treatment in a porous model system [52] as shown in Figure 1.2. This particular study shows the dependence of the longitudinal relaxation on the surface coating of glass beads. A siliconizing agent that creates a hydrophobic surface on the beads results in a shortened longitudinal relaxation time ($T_1 = 9$ seconds) when compared to untreated glass beads ($T_1 = 35$ seconds). The difference in the relaxation times enables the MRI contrast shown in Figure 1.2B and C.

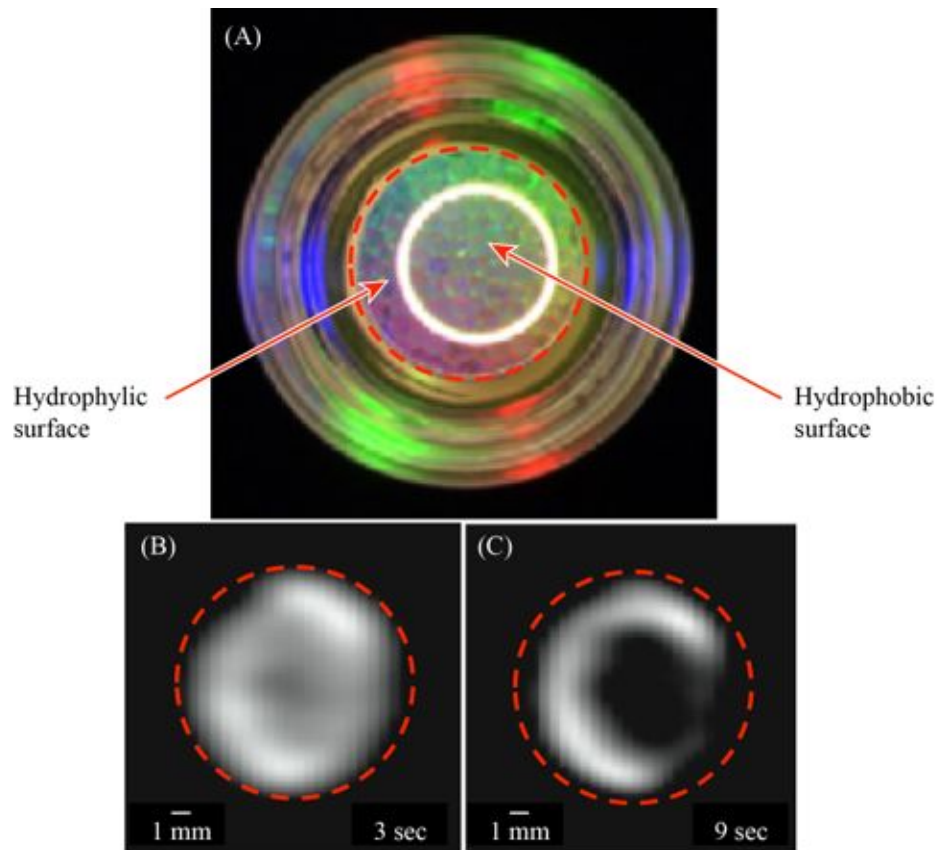


Figure 1.2. Demonstration of surface sensitive T_1 contrast using hyperpolarized ^{83}Kr . (A) Photograph of the sample cell containing hydrophilic and hydrophobic coated beads. The solid white line shows the barrier between types of beads. The dotted red line indicates the outer edge of the sample container for MR experiments. MR images taken (B) 3 seconds and (C) 9 seconds after delivery of hyperpolarized ^{83}Kr gas mixture revealing surface sensitive contrast. Surface sensitive contrast arises from the differences in longitudinal relaxation. Figure adapted from ref. [52].

MRI distinguishes the difference between hydrophilic and hydrophobic surfaces because of the longitudinal relaxation in each environment allowing T_1 weighting of the image to highlight the difference in the surface. Additional studies by Meersmann and co-workers demonstrate that ^{83}Kr longitudinal relaxation is altered by the surface to

volume ratio (S/V), surface composition, surface temperature, and surface adsorption of molecules [52-54].

A recent study using hyperpolarized ^{83}Kr found that the longitudinal relaxation of ^{83}Kr is sensitive to the different regions in *ex vivo* rat lungs as a consequence of the S/V ratio in those areas [55]. This study uses a series of constant small flip angle pulses for 1D NMR spectroscopy with results shown in Figure 1.3. Data acquisition starts prior to hyperpolarized gas inhalation, therefore the inhalation process is observed by the increase of the signal. After completion of inhalation, shown by the maximum signal, the T_1 relaxation is determined from the decay of the signal amplitude. Various inhalation schemes directed the hyperpolarized ^{83}Kr to the desired region of the lung. For example, the gas is directed to the airways, accomplished by inhaling only a small amount of hyperpolarized gas (6 mL) on top of already partially inflated lungs (6 ml pre-existing in lung before hyperpolarized ^{83}Kr inhalation), results in a T_1 of 1.57 ± 0.07 s. Inhaling a 6 ml portion of hyperpolarized ^{83}Kr followed by 6 ml of air directs the hyperpolarized gas into the alveolar regions and results in a T_1 of 1.07 ± 0.08 s. The difference in the T_1 between inhalation schemes suggests that ^{83}Kr can determine surface to volume ratios in the lung. Therefore ^{83}Kr relaxation measurements may be able to provide information complementary to ^3He and ^{129}Xe ADC measurements.

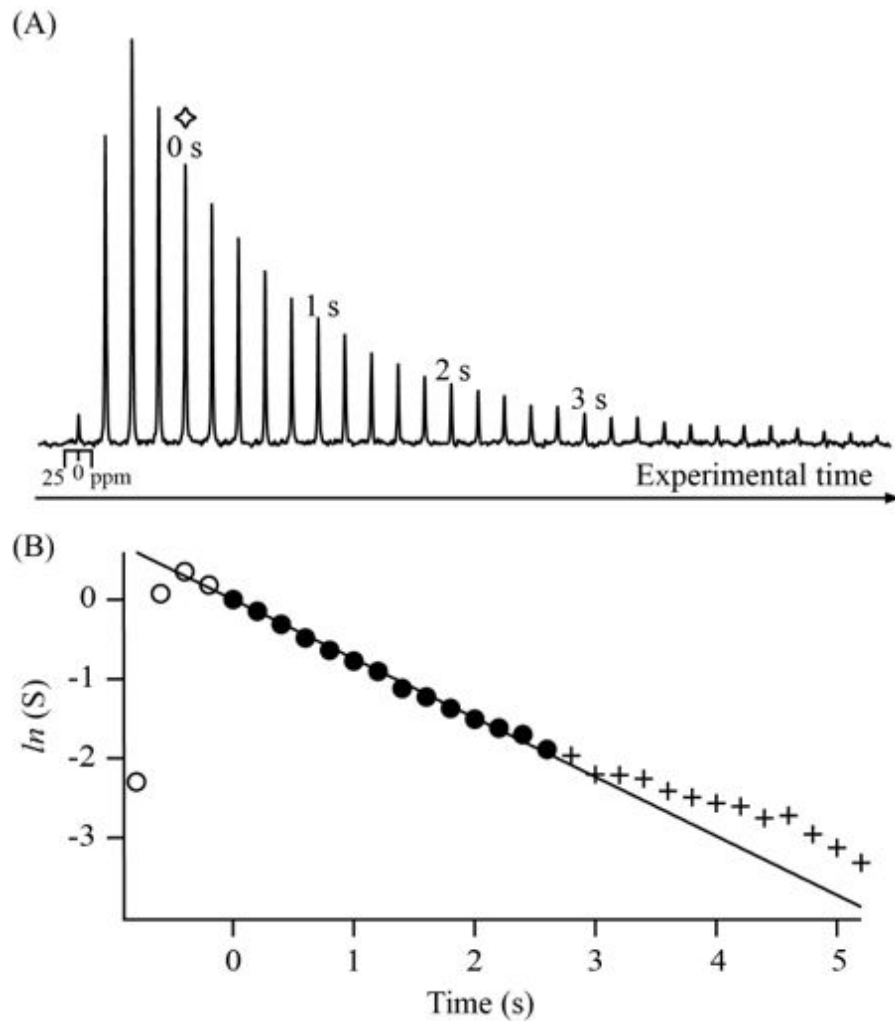


Figure 1.3. T_1 determination of ^{83}Kr in *ex vivo* rat lungs. **(A)** Signal intensity observed during inhalation and the decay due to longitudinal relaxation. **(B)** T_1 is determined from a fitting of the linear portion of the semi-logarithmic plot of data in A. Figure provided courtesy of ref. [55].

Unfortunately, quadrupolar relaxation also limits the hyperpolarized ^{83}Kr signal intensity and applications of hyperpolarized ^{83}Kr pulmonary MRI are limited to low resolution images [52, 56] with little chance to provide data about internal structure or function of the lung as demonstrated in Figure 1.4. Separate batches of hyperpolarized ^{83}Kr gas that acquire the 16 phase encoding increments individually are combined for image reconstruction. Resolution of the non-slice selective image is $2.3 \times 2.3 \text{ mm}^2$.

Multiple batches of hyperpolarized gas are time consuming and also may cause artefacts in the image from slightly different inhalation quantities and signal intensities between experiments. The low resolution image shown in Figure 1.4 illustrates that improved hyperpolarization strategies are necessary for pulmonary ^{83}Kr MRI. It is important to note that hyperpolarized ^{83}Kr MRI will unlikely result in the current resolution of ^3He and ^{129}Xe ventilation images. However, the surface dependent quadrupolar relaxation may give complementary information of lung function or possibly provide information that cannot be acquired using an isotope without a nuclear electric quadrupole moment.

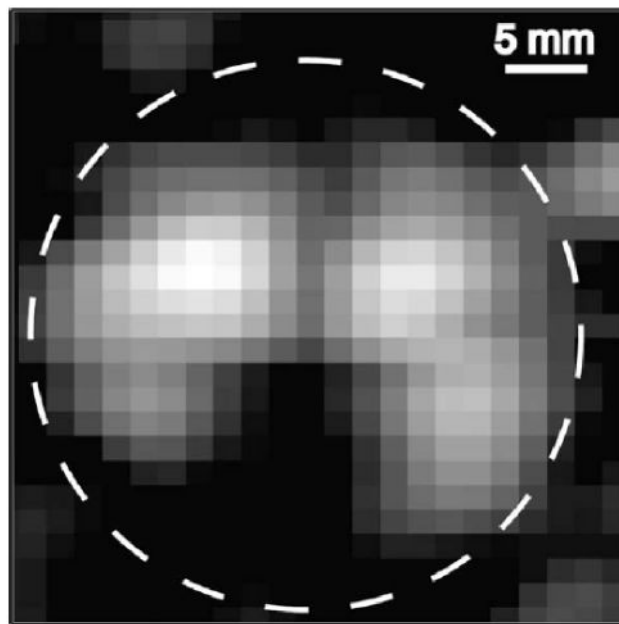


Figure 1.4. Previously published hyperpolarized ^{83}Kr transverse image of an *ex vivo* rat lung. Courtesy of ref. [56].

1.3 Aims of this work

Research presented in this document strives to improve the hyperpolarization of ^{83}Kr to enable pulmonary ^{83}Kr MRI. Appropriate theoretical background into the topic of magnetic resonance and hyperpolarized noble gases is provided in Chapter 2. A new hyperpolarization methodology is thoroughly investigated in Chapter 3 then extended and applied to pulmonary imaging in Chapter 4. Together Chapters 3 and 4 make the bulk of this thesis and the research for the purpose of this degree: developing *new MRI contrast agents through spin exchange optical pumping of noble gases with a nuclear electric quadrupole moment*. It is important to note that the hyperpolarization techniques proposed for ^{83}Kr are also useful for the production of hyperpolarized ^{129}Xe and have been used in published and on-going studies.

In Chapter 5 the transverse relaxation of ^{129}Xe and ^{83}Kr is studied. Transverse relaxation is caused, in part, from diffusion of an atom in a magnetic field gradient. A firm understanding of transverse relaxation may eventually improve information of diffusion processes in the lung and provide a source of contrast in future pulmonary studies. Chapter 6 develops a technique to produce hyperpolarized ^{129}Xe for use as a probe into combustion processes. The new SEOP method enables the first *in situ* MRI of combustion and permits characterization combustion process. The combustion experiments focuses on ^{129}Xe as a proof of principle, but concepts from the combustion study will be expanded to isotopes with a nuclear electric quadrupole moment in the near future.

1.4 References

- [1] A.D. Lopez, C.D. Mathers, M. Ezzati, D.T. Jamison, C.J.L. Murray, Global and regional burden of disease and risk factors, 2001: systematic analysis of population health data, *The Lancet*, 367 (2006) 1747-1757.
- [2] J.B. Soriano, W.C. Maier, P. Egger, G. Visick, B. Thakrar, J. Sykes, N.B. Pride, Recent trends in physician diagnosed COPD in women and men in the UK, *Thorax*, 55 (2000) 789-794.
- [3] P.M.A. Calverley, P. Walker, Chronic obstructive pulmonary disease, *The Lancet*, 362 (2003) 1053-1061.
- [4] C.J.L. Murray, A.D. Lopez, Alternative projections of mortality and disability by cause 1990-2020: Global Burden of Disease Study, *The Lancet*, 349 (1997) 1498-1504.
- [5] E.R. Weibel, What makes a good lung? The morphometric basis of lung function, *Swiss Medical Weekly*, 139 (2009) 375-386.
- [6] D.M. Mannino, A.S. Buist, Global burden of COPD: risk factors, prevalence, and future trends, *The Lancet*, 370 (2007) 765-773.
- [7] R. Peto, Smoking and death: the past 40 years and the next 40, *BMJ: British Medical Journal*, 309 (1994) 937.
- [8] C.J.L. Murray, A.D. Lopez, Mortality by cause for eight regions of the world: Global Burden of Disease Study, *The Lancet*, 349 (1997) 1269-1276.
- [9] C.J.L. Murray, A.D. Lopez, Regional patterns of disability-free life expectancy and disability-adjusted life expectancy: Global Burden of Disease Study, *The Lancet*, 349 (1997) 1347-1352.
- [10] C.J.L. Murray, A.D. Lopez, Global mortality, disability, and the contribution of risk factors: Global Burden of Disease Study, *The Lancet*, 349 (1997) 1436-1442.
- [11] H. Hatabu, D.C. Alsop, J. Listerud, M. Bonnet, W.B. Geftter, T2* and proton density measurement of normal human lung parenchyma using submillisecond echo time gradient echo magnetic resonance imaging, *European Journal of Radiology*, 29 (1999) 245-252.
- [12] C.J. Bergin, J.M. Pauly, A. Macovski, Lung Parenchyma - Projection Reconstruction MR-Imaging, *Radiology*, 179 (1991) 777-781.
- [13] C.J. Bergin, G.H. Glover, J.M. Pauly, Lung parenchyma: magnetic susceptibility in MR imaging, *Radiology*, 180 (1991) 845-848.
- [14] C.J. Bergin, D.C. Noll, J.M. Pauly, G.H. Glover, A. Macovski, MR imaging of lung parenchyma: a solution to susceptibility, *Radiology*, 183 (1992) 673-676.
- [15] H. Hatabu, Q. Chen, K.W. Stock, W.B. Geftter, H. Itoh, Fast magnetic resonance imaging of the lung, *European Journal of Radiology*, 29 (1999) 114-132.
- [16] K.W. Stock, Q. Chen, H. Hatabu, R.R. Edelman, Magnetic resonance T2* measurements of the normal human lung in vivo with ultra-short echo times, *Magnetic Resonance Imaging*, 17 (1999) 997-1000.
- [17] J.P. Mugler, T.A. Altes, Hyperpolarized ¹²⁹Xe MRI of the human lung, *Journal of Magnetic Resonance Imaging*, 37 (2013) 313-331.
- [18] H. Middleton, R.D. Black, B. Saam, G.D. Cates, G.P. Cofer, R. Guenther, W. Happer, L.W. Hedlund, G.A. Johnson, K. Juvan, J. Swartz, MR-Imaging with Hyperpolarized He-3 Gas, *Magn. Reson. Med.*, 33 (1995) 271-275.

- [19] M.S. Albert, G.D. Cates, B. Driehuys, W. Happer, B. Saam, C.S. Springer, A. Wishnia, Biological Magnetic-Resonance-Imaging Using Laser Polarized Xe-129, *Nature*, 370 (1994) 199-201.
- [20] S.B. Fain, F.R. Korosec, J.H. Holmes, R. O'Halloran, R.L. Sorkness, T.M. Grist, Functional lung imaging using hyperpolarized gas MRI, *Journal of Magnetic Resonance Imaging*, 25 (2007) 910-923.
- [21] H.U. Kauczor, D. Hofmann, K.F. Kreitner, H. Nilgens, R. Surkau, W. Heil, A. Potthast, M.V. Knopp, E.W. Otten, M. Thelen, Normal and abnormal pulmonary ventilation: Visualization at hyperpolarized He-3 MR imaging, *Radiology*, 201 (1996) 564-568.
- [22] H.U. Kauczor, M. Ebert, K.-F. Kreitner, H. Nilgens, R. Surkau, W. Heil, D. Hofmann, E.W. Otten, M. Thelen, Imaging of the lungs using 3He MRI: Preliminary clinical experience in 18 patients with and without lung disease, *Journal of Magnetic Resonance Imaging*, 7 (1997) 538-543.
- [23] E.E. de Lange, J.P. Mugler, J.R. Brookeman, J. Knight-Scott, J.D. Truwit, C.D. Teates, T.M. Daniel, P.L. Bogorad, G.D. Cates, Lung air spaces: MR imaging evaluation with hyperpolarized He-3 gas, *Radiology*, 210 (1999) 851-857.
- [24] B.T. Saam, D.A. Yablonskiy, V.D. Kodibagkar, J.C. Leawoods, D.S. Gierada, J.D. Cooper, S.S. Lefrak, M.S. Conradi, MR imaging of diffusion of He-3 gas in healthy and diseased lungs, *Magn. Reson. Med.*, 44 (2000) 174-179.
- [25] M. Salerno, E.E. de Lange, T.A. Altes, J.D. Truwit, J.R. Brookeman, J.P. Mugler, Emphysema: Hyperpolarized Helium 3 Diffusion MR Imaging of the Lungs Compared with Spirometric Indexes, *Initial Experience*, *Radiology*, 222 (2002) 252-260.
- [26] A.L. Sukstanskii, M.S. Conradi, D.A. Yablonskiy, He-3 lung morphometry technique: Accuracy analysis and pulse sequence optimization, *Journal of Magnetic Resonance*, 207 (2010) 234-241.
- [27] J. Parra-Robles, S. Ajraoui, M.H. Deppe, S.R. Parnell, J.M. Wild, Experimental investigation and numerical simulation of (3)He gas diffusion in simple geometries: Implications for analytical models of (3)He MR lung morphometry, *Journal of Magnetic Resonance*, 204 (2010) 228-238.
- [28] X.J. Chen, L.W. Hedlund, H.E. Moller, M.S. Chawla, R.R. Maronpot, G.A. Johnson, Detection of emphysema in rat lungs by using magnetic resonance measurements of 3He diffusion, *Proceedings of the National Academy of Sciences*, 97 (2000) 11478-11481.
- [29] A.J. Swift, J.M. Wild, S. Fischele, N. Woodhouse, S. Fleming, J. Waterhouse, R.A. Lawson, M.N.J. Paley, E.J.R. Van Beek, Emphysematous changes and normal variation in smokers and COPD patients using diffusion He-3 MRI, *European Journal of Radiology*, 54 (2005) 352-358.
- [30] D.A. Yablonskiy, A.L. Sukstanskii, J.C. Leawoods, D.S. Gierada, G.L. Bretthorst, S.S. Lefrak, J.D. Cooper, M.S. Conradi, Quantitative in vivo assessment of lung microstructure at the alveolar level with hyperpolarized He-3 diffusion MRI, *Proceedings of the National Academy of Sciences of the United States of America*, 99 (2002) 3111-3116.
- [31] J.R. Owers-Bradley, S. Fischele, A. Bennattayalah, C.J.S. McGloin, R.W. Bowtell, P.S. Morgan, A.R. Moody, MR tagging of human lungs using hyperpolarized He-3 gas, *Journal of Magnetic Resonance Imaging*, 17 (2003) 142-146.

- [32] B. Eberle, N. Weiler, K. Markstaller, H.-U. Kauczor, A. Deninger, M. Ebert, T. Grossmann, W. Heil, L. Lauer, T. Roberts, Analysis of intrapulmonary O₂ concentration by MR imaging of inhaled hyperpolarized helium-3, *Journal of Applied Physiology*, 87 (1999) 2043-2052.
- [33] M.C. Fischer, Z.Z. Spector, M. Ishii, J. Yu, K. Emami, M. Itkin, R. Rizi, Single-acquisition sequence for the measurement of oxygen partial pressure by hyperpolarized gas MRI, *Magn. Reson. Med.*, 52 (2004) 766-773.
- [34] G.E. Santyr, W.W. Lam, J.M. Parra-Robles, T.M. Taves, A.V. Ouriadov, Hyperpolarized noble gas magnetic resonance imaging of the animal lung: Approaches and applications, *Journal of Applied Physics*, 105 (2009) 102004-102013.
- [35] B. Saam, W. Happer, H. Middleton, Nuclear-Relaxation of He-3 in the Presence of O-2, *Physical Review A*, 52 (1995) 862-865.
- [36] A.J. Deninger, B. Eberle, M. Ebert, T. Grossmann, W. Heil, H.U. Kauczor, L. Lauer, K. Markstaller, E. Otten, J. Schmiedeskamp, W. Schreiber, R. Surkau, M. Thelen, N. Weiler, Quantification of Regional Intrapulmonary Oxygen Partial Pressure Evolution during Apnea by 3He MRI, *Journal of Magnetic Resonance*, 141 (1999) 207-216.
- [37] H. Marshall, J. Parra-Robles, M.H. Deppe, D.A. Lipson, R. Lawson, J.M. Wild, 3He pO₂ mapping is limited by delayed-ventilation and diffusion in chronic obstructive pulmonary disease, *Magn. Reson. Med.*, (2013).
- [38] D.M.L. Lilburn, G.E. Pavlovskaya, T. Meersmann, Perspectives of hyperpolarized noble gas MRI beyond 3He, *Journal of Magnetic Resonance*, 229 (2013) 173-186.
- [39] J.C. Woods, Congressional Hearing: "Caught by Surprise: Causes and Consequences of the Helium-3 Supply Crisis", Testimony before the House Committee on Science and Technology, Subcommittee on Investigations and Oversight, (2010).
- [40] F.W. Hersman, I.C. Ruset, S. Ketel, I. Muradian, S.D. Covrig, J. Distelbrink, W. Porter, D. Watt, J. Ketel, J. Brackett, A. Hope, S. Patz, Large production system for hyperpolarized Xe-129 for human lung imaging studies, *Academic Radiology*, 15 (2008) 683-692.
- [41] X.J. Chen, H.E. Moller, M.S. Chawla, G.P. Cofer, B. Driehuys, L.W. Hedlund, G.A. Johnson, Spatially resolved measurements of hyperpolarized gas properties in the lung in vivo. Part I: Diffusion coefficient, *Magn. Reson. Med.*, 42 (1999) 721-728.
- [42] J.C. Woods, D.A. Yablonskiy, C.K. Choong, K. Chino, J.A. Pierce, J.C. Hogg, J. Bentley, J.D. Cooper, M.S. Conradi, P.T. Macklem, Long-range diffusion of hyperpolarized He-3 in explanted normal and emphysematous human lungs via magnetization tagging, *J. Appl. Physiol.*, 99 (2005) 1992-1997.
- [43] J.F. Mata, T.A. Altes, J. Cai, K. Ruppert, W. Mitzner, K.D. Hagspiel, B. Patel, M. Salerno, J.R. Brookeman, E.E. de Lange, W.A. Tobias, H.T. Wang, G.D. Cates, J.P. Mugler, 3rd, Evaluation of emphysema severity and progression in a rabbit model: comparison of hyperpolarized 3He and 129Xe diffusion MRI with lung morphometry, *J Appl Physiol*, 102 (2007) 1273-1280.

- [44] M. Boudreau, X.J. Xu, G.E. Santyr, Measurement of ^{129}Xe gas apparent diffusion coefficient anisotropy in an elastase-instilled rat model of emphysema, *Magn. Reson. Med.*, 69 (2013) 211-220.
- [45] B. Driehuys, S.S. Kaushik, Z.I. Cleveland, G.P. Cofer, G. Metz, D. Beaver, J. Nouls, M. Kraft, W. Auffermann, J. Wolber, H.P. McAdams, Diffusion-Weighted Hyperpolarized (^{129}Xe) MRI in Healthy Volunteers and Subjects With Chronic Obstructive Pulmonary Disease, *Magn. Reson. Med.*, 65 (2011) 1155-1165.
- [46] M. Kirby, S. Svenningsen, A. Owrangi, A. Wheatley, A. Farag, A.V. Ouriadov, G.E. Santyr, R. Etemad-Rezai, H.O. Coxson, D.G. McCormack, G. Parraga, Hyperpolarized ^3He and ^{129}Xe MR Imaging in Healthy Volunteers and Patients with Chronic Obstructive Pulmonary Disease, *Radiology* (2012) 280-289.
- [47] M. Kirby, M. Heydarian, A. Wheatley, D.G. McCormack, G. Parraga, Evaluating bronchodilator effects in chronic obstructive pulmonary disease using diffusion-weighted hyperpolarized helium-3 magnetic resonance imaging, *Journal of Applied Physiology*, 112 (2012) 651-657.
- [48] J.C. Woods, Mine the moon for ^3He MRI? Not yet, *J Appl Physiol* (1985), 114 (2013) 705-706.
- [49] K. Ruppert, J.R. Brookeman, K.D. Hagspiel, J.P. Mugler, Probing lung physiology with xenon polarization transfer contrast (XTC), *Magn. Reson. Med.*, 44 (2000) 349-357.
- [50] B. Driehuys, H.E. Moller, Z.I. Cleveland, J. Pollaro, L.W. Hedlund, Pulmonary Perfusion and Xenon Gas Exchange in Rats: MR Imaging with Intravenous Injection of Hyperpolarized Xe-^{129} , *Radiology*, 252 (2009) 386-393.
- [51] B. Driehuys, G.P. Cofer, J. Pollaro, J.B. Mackel, L.W. Hedlund, G.A. Johnson, Imaging alveolar-capillary gas transfer using hyperpolarized Xe-^{129} MRI, *Proceedings of the National Academy of Sciences of the United States of America*, 103 (2006) 18278-18283.
- [52] G.E. Pavlovskaya, Z.I. Cleveland, K.F. Stupic, T. Meersmann, Hyperpolarized Krypton-83 as a New Contrast Agent for Magnetic Resonance Imaging, *Proceedings of the National Academy of Sciences of the United States of America*, 102 (2005) 18275-18279.
- [53] K.F. Stupic, Z.I. Cleveland, G.E. Pavlovskaya, T. Meersmann, Quadrupolar Relaxation of Hyperpolarized Krypton-83 as a Probe for Surfaces, *Solid State Nuclear Magnetic Resonance*, 29 (2006) 79-84.
- [54] Z.I. Cleveland, K.F. Stupic, G.E. Pavlovskaya, J.E. Repine, J.B. Wooten, T. Meersmann, Hyperpolarized ^{83}Kr and ^{129}Xe NMR Relaxation Measurements of Hydrated Surfaces: Implications for Materials Science and Pulmonary Diagnostics, *Journal of the American Chemical Society*, 129 (2007) 1784-1792.
- [55] K.F. Stupic, N.D. Elkins, G.E. Pavlovskaya, J.E. Repine, T. Meersmann, Effects of pulmonary inhalation on hyperpolarized krypton-83 magnetic resonance T-1 relaxation, *Physics in Medicine and Biology*, 56 (2011) 3731-3748.
- [56] Z.I. Cleveland, G.E. Pavlovskaya, N.D. Elkins, K.F. Stupic, J.E. Repine, T. Meersmann, Hyperpolarized Kr-^{83} MRI of lungs, *Journal of Magnetic Resonance*, 195 (2008) 232-237.

Chapter 2 Background and theory

2.1 Purpose of chapter

This chapter will provide basic concepts of nuclear magnetic resonance (NMR) to enable an understanding of the original research presented later in this work. NMR is a well-developed field that has several quality sources introducing the topic thoroughly; four particularly useful references were consulted extensively for the theoretical framework of magnetic resonance presented in this chapter [1-4]. The primary focus is to provide a limited background of magnetic resonance to understand the significance and the methods utilized for hyperpolarization of spin active nuclei, predominantly the concept spin-exchange optical pumping (SEOP) of noble gas nuclei. The relaxation behavior of quadrupolar nuclei with relevance to this work will also be discussed. Basic magnetic resonance imaging (MRI) techniques that are relevant to the research in this work will be presented. Detailed theoretical background for each individual experiment will be provided in the following chapters when necessary.

2.2 Introduction to Nuclear Magnetic Resonance

2.2.1 Nuclear spin in a magnetic field

Nuclei that have an odd atomic number or odd atomic mass possess angular momentum and are identified as magnetic resonance active, meaning they can be observed and manipulated using electromagnetic radiation for nuclear magnetic resonance (NMR) spectroscopy or magnetic resonance imaging (MRI). The angular momentum, an intrinsic property termed spin, arises from the fermions that make up the neutrons and protons in the nucleus of the atom. The most commonly used isotope for NMR and MRI is ^1H (a single proton), which has spin $I = 1/2$. The large natural occurrence of the isotope and the abundance of the atom, demonstrated by its presence in water and often found in organic molecules, make it very useful for both magnetic resonance spectroscopy and imaging. The original research in this work will focus on the alternative spin active noble gas isotopes shown in Table 2.1.

A nucleus may have spin $I > 1/2$ giving the nucleus a nuclear electric quadrupole moment (Q) and additional energy states are available. The inclusion of the nuclear electric quadrupole moment makes the system challenging but also rewarding in a number of cases as briefly mentioned in the introduction chapter and discussed in greater detail in *section 2.2.5*. The following discussion on nuclear magnetic resonance will concentrate on spin $I = 1/2$ systems for the sake of simplicity.

Table 2.1. Properties of nuclear isotopes relevant to this work. Note that ^1H is provided for comparison, the isotope is not used in the studies of this work. Values taken from reference [5].

Isotope	Spin	Natural abundance $x/\%$	Gyromagnetic ratio $\gamma/10^7 \text{ rad s}^{-1}\text{T}^{-1}$	Quadrupolar moment Q/fm^2	Frequency ratio $X/\%$
^1H	1/2	99.9885	26.7522128	-	100.000000 ^A
^3He	1/2	0.000137	-20.3801587	-	76.179437
^{21}Ne	3/2	0.27	-2.11308	10.155	7.894296
^{83}Kr	9/2	11.49	-1.03310	25.9	3.847600
^{129}Xe	1/2	26.44	-7.452103	-	27.810186
^{131}Xe	3/2	21.18	2.209076	-11.5	8.243921

Table values taken from reference [5]

^ABy definition

A nucleus that possesses angular momentum will have a magnetic moment, $\boldsymbol{\mu}$, that is described by:

$$\boldsymbol{\mu} = \gamma \hbar \mathbf{I} \quad (2.1)$$

where γ is the gyromagnetic ratio specific to each nucleus, \hbar is Plank's constant h ($6.626075 \times 10^{-34} \text{ J s}$) divided by 2π , \mathbf{I} is the angular momentum operator of the nucleus. The orientation of the angular momentum vector, and therefore the magnetic field is often called the *spin polarization axis* [3] and will be referred to as such throughout this discussion.

In the presence of a magnetic field the total energy operator (the Hamiltonian) of the nucleus is $\mathbf{H} = -\boldsymbol{\mu} \cdot \mathbf{B}$. By defining the field to be along the z -axis and substituting in Eq. 2.1 the Hamiltonian becomes $\mathbf{H} = -\gamma \hbar B_0 \mathbf{I}_z$. The Hamiltonian can then be inserted into the time independent Schrödinger equation ($E\Psi = \mathbf{H}\Psi$) to determine the energy of the system:

$$E = -\gamma m \hbar B_0 \quad (2.2)$$

where m are values ranging from $I, I-1, \dots, -I$. For example ^{129}Xe , which has spin $I=1/2$, two energy states are available: $m=1/2$ and $m=-1/2$ as depicted in Figure 2.1.

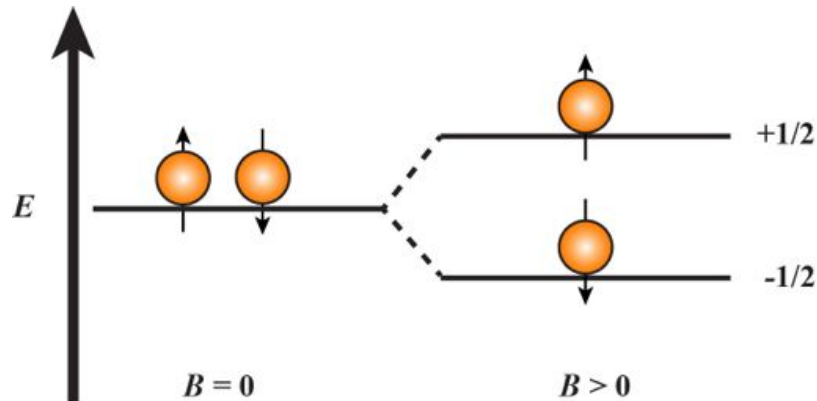


Figure 2.1. Energy diagram for two ^{129}Xe nuclei with and without the presence of an external magnetic field. The arrow in the nucleus represents the direction spin polarization axis.

The spin polarization axis precesses around axis of the external magnetic field as illustrated in Figure 2.2. The frequency of the precession, namely the Larmor frequency, is dependent on the gyromagnetic and magnetic field strength by the relationship: $\omega_0 = -\gamma B_0$ where ω_0 is the Larmor frequency in radians per second. The direction of precession depends on the sign of the gyromagnetic ratio.

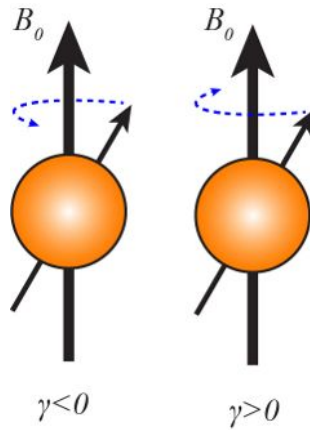


Figure 2.2. Precession of the magnetic moment vector around an external magnetic field. The angle between spin polarization axis and B_0 is exaggerated for this illustration adapted from ref. [3].

When considering an ensemble of spins the net magnetic field produced by the angular momentum behave similarly to the spin polarization axis of individual spins that was previously discussed. Without an external magnetic field the random orientation of the nuclei results in no net magnetic field as illustrated in Figure 2.3A. However, when placed in an external magnetic field the spins orient themselves to the magnetic field creating a net magnetic field what is often referred to as the bulk magnetic field vector as illustrated in Figure 2.3B.

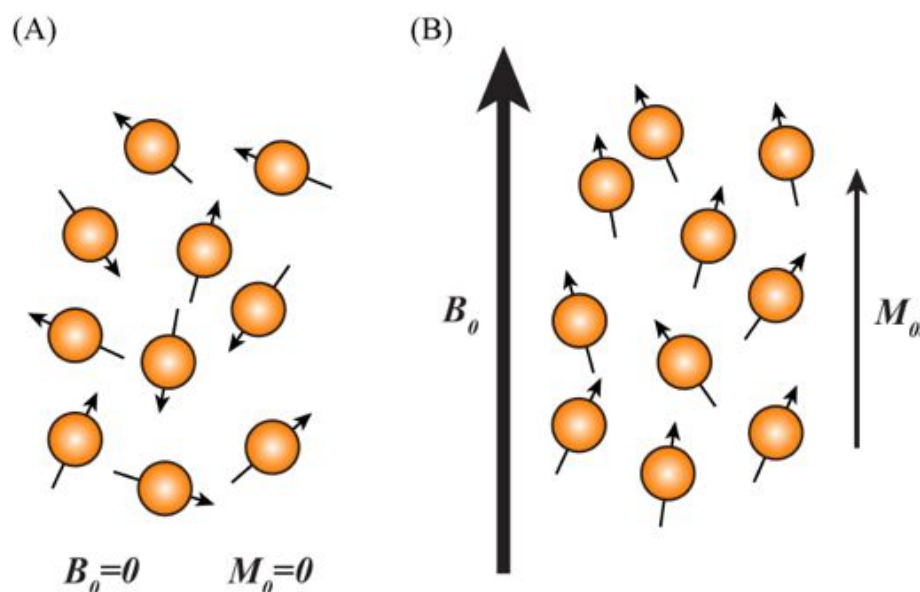


Figure 2.3. The behavior of the net magnetic field of an ensemble of spin (A) without and (B) with the presence of an external magnetic field. M_0 is the magnetization of the nuclear spins.

Applying a radio frequency pulse resonant to the Larmor frequency rotates the orientation of the bulk magnetic field vector from alignment with the external magnet field towards the transverse (x-y) plane as shown in Figure 2.4. This interaction forces the spins to be in a non-equilibrium state and over time the spins will return to equilibrium with its environment as discussed further in *section 2.2.4*. The amount of magnetization that is rotated or ‘tipped’ into the transverse plane can be controlled by the power and length of the radio frequency pulse. The maximum signal arises when all available magnetization tipped to the transverse plane by a rotation 90° from alignment with the external magnetic field. The angle of rotation is called the flip angle, using diverse flip angles is important in a number of magnetic resonance applications and is commonly employed in magnetic resonance of hyperpolarized systems.

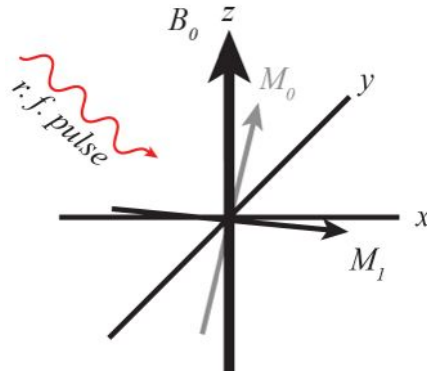


Figure 2.4. Application of a 90° ($\pi/2$) radio frequency pulse rotates the bulk magnetization vector from alignment with the external magnetic field (M_0) into the transverse plane (M_1).

2.2.2 Signal and population distribution at thermal equilibrium

The strength of the signal is determined, in part, by the polarization (P) of the sample. In the spin $I = 1/2$ case, this is the difference in population between the two spin states as defined by:

$$P = \frac{N_{\uparrow} - N_{\downarrow}}{N_{\uparrow} + N_{\downarrow}} \quad (2.3)$$

where, N_{\uparrow} and N_{\downarrow} are the total number of nuclear spins in the $m = 1/2$ and $m = -1/2$ spin states. At thermal equilibrium the fraction of nuclei in each spin state can be defined by the Boltzmann equation:

$$N_i = \frac{e^{-E_i/kT}}{z} \quad (2.4)$$

where, N_i is the population in the spin state i , E_i is the energy of spin state i , k is the Boltzmann constant (1.38066×10^{-23} J/K), T is temperature, and z is the partition function (state sum, sum of all energy levels) with value

$\sum_j e^{-E_j/kT}$. The energy from Eq. 2.2 can be substituted into Eq. 2.4 with the

partition function to become:

$$N_i = \frac{e^{\gamma m_i \hbar B_0 / kT}}{\sum_j e^{\gamma m_j \hbar B_0 / kT}} \quad (2.5)$$

Eq. 2.5 can then be substituted back into the polarization Eq. 2.3 for the spin

$I = 1/2$ case to become:

$$P = \frac{e^{\gamma m \hbar B_0 / 2kT} - e^{-\gamma m \hbar B_0 / 2kT}}{e^{\gamma m \hbar B_0 / 2kT} + e^{-\gamma m \hbar B_0 / 2kT}} \quad (2.6)$$

Eq. 2.6 can be simplified using the high temperature approximation where

$\gamma \hbar B_0 / 2kT \ll 1$:

$$P \approx \frac{|\gamma| \hbar B_0}{2kT} \quad (2.7)$$

The approximation in Eq. 2.7 reveals the dependence of the polarization on the gyromagnetic ratio (γ) and magnetic field strength (B_0).

Eq. 2.7 indicates that, all else being equivalent, a nucleus with a small gyromagnetic ratio will result in less available magnetization than a nucleus with a large gyromagnetic ratio. This limitation in signal is one of a number of obstacles to overcome in ^{83}Kr magnetic resonance. It is also important to mention that Eq. 2.7 also describes a direct dependence of the polarization on magnetic field. This indicates that magnetic resonance signal acquired in a 9.4 T magnet (common laboratory field strength) will have over three times the thermal polarization level than at 3.0 T (common medical MRI scanner field strength).

For a moment return to the origin of Eq. 2.7. If we consider Eq. 2.3 it can be seen that the polarization, and therefore signal intensity, arise from

the difference of population between spin energy states and that the population is determined from the difference in energy. The difference in energy between nuclear spin states is very small compared to vibrational modes and electronic transitions, plaguing magnetic resonance with weak signal intensities when compared with either infrared or visible spectroscopy. However, the versatility of magnetic resonance makes accepting and overcoming the limited signal intensity worthwhile.

Furthermore, the polarization is not the only important parameter leading to signal intensity but also the amount, or density of spins therefore the total magnetization must be explored. The magnetization can be expressed by:

$$M_0 = \frac{N\gamma\hbar P}{2}, \quad (2.8)$$

where, N is the amount of nuclear spins. The polarization Eq. 2.7 can be substituted into Eq. 2.8 to have:

$$M_0 = \frac{N\gamma^2\hbar^2 B_0}{4k_b T}, \quad (2.9)$$

which describes the magnetization of a sample at thermal equilibrium. The importance of looking at the magnetization opposed to the polarization is highlighted in conventional NMR spectroscopy of organic molecules dissolved in liquids where ^1H signal is very strong, but ^{13}C signal is very weak and many scans are required. The difference in signal goes beyond the polarization calculated in Eq. 2.7 due to the reduced gyromagnetic ratio but also the amount of each nucleus must be considered. The ^{13}C isotope of carbon has a natural abundance of only 1.07% whereas ^1H has a natural

abundance of 99.9885% [5], making signal from a naturally abundant sample of hydrogen much greater than that of carbon.

Much of the work that will be presented in later chapters of this thesis will investigate magnetic resonance properties of gases. The density of atoms is much less for gases than for the molecules dissolved in liquids which means limitations of NMR signal intensities are exacerbated. To overcome the low signal intensity from the gas many signal averages are required. Alternatively, creating polarization beyond thermal equilibrium (i.e. hyperpolarization) is a method of overcoming signal limitations inherent to magnetic resonance.

2.2.3 Hyperpolarization through spin exchange optical pumping

To overcome limited signal arising from the small population difference between energy levels a number of techniques have been developed that enhance the population difference and in turn the signal intensity as demonstrated in Figure 2.5. When looking at Eq. 2.7 the most straightforward method to increase the population difference is to increase the external magnetic field strength, however, instruments peak at approximately 23.5 T with substantial monetary investment needed. Additionally, there are health and safety concerns when using high magnetic fields with humans for MRI.

On the other hand, the temperature of a sample may be reduced to increase the population difference. However, even at liquid helium temperature (4 K) the nuclear spin polarization of hydrogen is approximately 0.3% versus only 0.005% at room temperature (calculated using Eq. 2.7 in a 9.4 T magnetic field). Therefore, going to high magnetic

field strengths or cooling the sample may be impractical in many applications with limited reward.

As an alternative to reducing the actual temperature of a sample, methods to reduce the spin temperature (i.e. changing the polarization by altering *effective* temperature of the spin system calculated using the Boltzmann equation) have been developed. The process of reducing spin temperature to increase spin polarization from what is dictated by the Boltzmann distribution at thermal equilibrium is called hyperpolarization. (for an example refer to Figure 2.5).

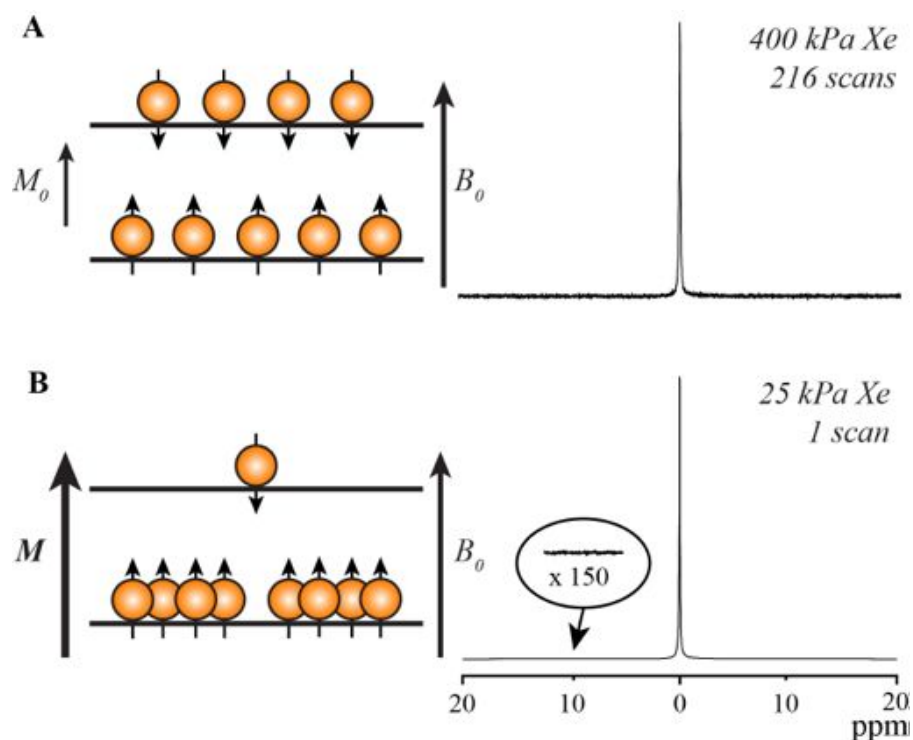


Figure 2.5. Thermally polarized sample compared to hyperpolarized sample of ^{129}Xe with diagram to demonstrate the signal enhancement achieved by hyperpolarization. **(A)** Diagram representing the small difference of populations between energy levels of nuclear spins at thermal equilibrium ($\sim 295\text{ K}$) with ^{129}Xe signal from a 400 kPa sample of xenon at thermal equilibrium (216 scans added, $\text{SNR} \approx 100$). **(B)** Diagram representing the large difference of nuclear spin populations between energy levels of a hyperpolarized sample adjacent to hyperpolarized ^{129}Xe signal from a 25 kPa sample of xenon (1 scan, $\text{SNR} \approx 300$). Notice the SNR in (B) is significantly greater than in (A) even though the thermal sample contains a much larger quantity of xenon and utilized signal averaging. Note that the resonance frequency is strongly dependent on the gas pressure and the radio frequency pulses were on resonance for both (A) and (B). Example spectra were collected for the purpose of this document.

Dynamic nuclear polarization (DNP) is a technique that capitalizes on the much greater spin polarization of an electron ($\gamma_e/\gamma_n > 657$) by transferring the spin polarization from the electron to the nucleus using microwave radiation [6]. This technique uses the improved spin polarization of an electron, which approaches 25% near liquid helium temperature (~ 4 K). Although originally proposed by Overhauser in 1953 [7], DNP has recently become of main stream interest because it has been recently demonstrated to hyperpolarize a sample for liquid state NMR [8] followed by usage for *in vivo* MRI applications [9, 10]. Alternatively to DNP, the studies presented in this work utilize a different hyperpolarization technique called spin exchange optical pumping (SEOP) for hyperpolarization.

SEOP is a two-step process: (1) optical pumping of an alkali metal vapor to achieve high electronic spin polarization which is then (2) transferred to the nucleus of the isotope of interest via spin exchange. The transfer of polarization from optically pumped alkali metal to a noble gas nucleus was demonstrated by Bouchiat et al. [11]. High electronic spin polarization of the alkali metal vapor is achieved by optical pumping, that is irradiation of a glass cell containing the alkali metal vapor with circularly polarized (σ^+) laser light resonant to the D_1 transition. Originally rubidium metal ($D_1 = 794.7$ nm) was utilised for this process [12] and is typically used for most studies today [13-15]. Additionally, work has been completed using cesium metal [16-18] and also mixtures of potassium - rubidium that capitalizes on availability of high power lasers tuned to the D_1 transition of rubidium and reduced spin destruction rates of potassium during SEOP [19, 20]. Only SEOP using rubidium will be discussed in this report.

When an external magnetic field is present along the SEOP cell parallel to the propagation of the laser beam angular momentum is transferred from the circularly polarized laser light to the rubidium electron. The transfer of angular momentum excites the valence electron from the $m_s = -1/2$ sublevel of the $^2S_{1/2}$ state to the $m_j = 1/2$ sublevel of the $5^2P_{1/2}$ state following the $\Delta m = 1$ selection rule as depicted in Figure 2.6. Populations in the $m_j = 1/2$ and $m_j = -1/2$ sublevels of the $^2P_{1/2}$ state are equalized through collisional mixing.

The electron can then return to either sublevel of the ground state through spontaneous emission of a photon with its polarization dependent on the relaxation path or through non-radiative quenching (i.e. no emission of a photon) caused by a collision with a molecule such as nitrogen that transfers the energy into the vibrational mode. Non-radiative quenching is preferred because spontaneous emission of a randomly polarized photon is destructive to the optical pumping process since it is non-selective at pumping any further electron it excites [21]. Therefore a quenching gas, typically nitrogen, is included in SEOP gas mixtures.

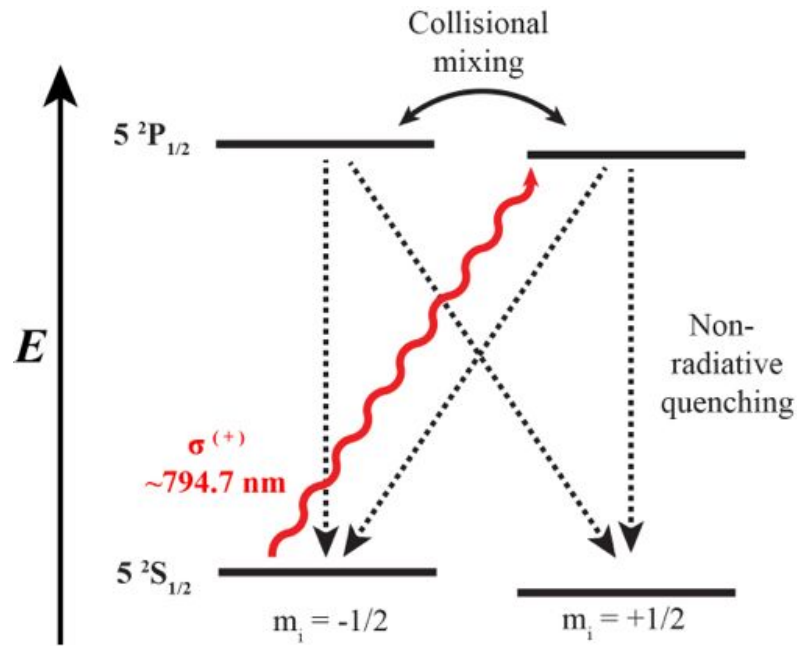


Figure 2.6. Optical Pumping of the valence electron of rubidium metal vapor using $\sigma^{(+)}$ circularly polarized laser light tuned to the D₁ transition. It is through the continuous depletion of the $m_s = -1/2$ sublevel of many rubidium atoms in the ensemble that results in a large electronic polarization.

The electronic polarization then transfers to the noble gas nuclei through spin exchange. Spin exchange is accomplished through two mechanisms: binary collisions (Figure 2.7A) and the formation of van der Waals complexes (Figure 2.7B). Binary collisions are the principal spin exchange mechanism for relatively small atoms such as ^3He or ^{83}Kr where the electron cloud has limited polarizability (i.e. ability of an electron cloud to become distorted). For larger atoms such as ^{129}Xe or ^{131}Xe spin exchange via a van der Waals complex increases because the greater polarizability in the electron cloud allows for the formation of the complex.

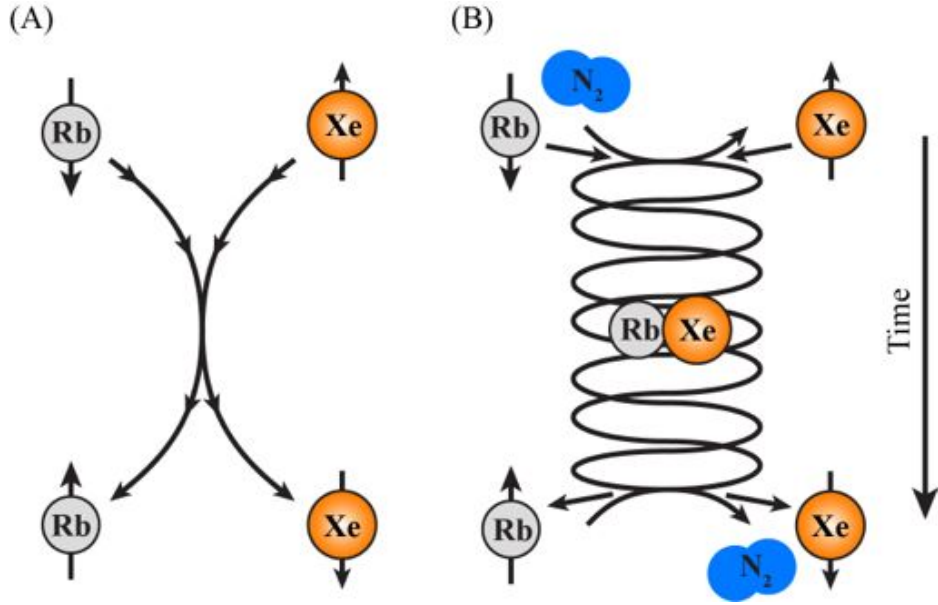


Figure 2.7. Spin exchange of spin polarization via (A) binary collisions and (B) van der Waals complexes.

The theoretical framework underlying SEOP was investigated thoroughly by William Happer and colleagues [13, 21, 22], only a brief overview will be provided here. A simplified spin Hamiltonian to describe the spin exchange process is [22]:

$$H = A\mathbf{I} \cdot \mathbf{S} + \alpha\mathbf{K} \cdot \mathbf{S} + \gamma\mathbf{N} \cdot \mathbf{S} + g_s\mu_B\mathbf{B} \cdot \mathbf{I} + g_K\mu_B\mathbf{B} \cdot \mathbf{K} + \dots \quad (2.8)$$

In equation (2.8), $A\mathbf{I} \cdot \mathbf{S}$ is the interaction between the nuclear spin, \mathbf{I} , and the electron spin, \mathbf{S} , of the rubidium atom, $\alpha\mathbf{K} \cdot \mathbf{S}$ is the interaction between the nuclear spin of the noble gas \mathbf{K} with \mathbf{S} , $\gamma\mathbf{N} \cdot \mathbf{S}$ is the interaction between the rotational angular momentum of the molecule \mathbf{N} with \mathbf{S} , while the remaining terms describe the coupling of \mathbf{I} , \mathbf{S} and \mathbf{N} with the magnetic field. The terms $\alpha\mathbf{K} \cdot \mathbf{S}$ and $\gamma\mathbf{N} \cdot \mathbf{S}$ are of particular importance because they describe the spin exchange from rubidium to the noble gas.

The $\alpha\mathbf{K}\cdot\mathbf{S}$ term in equation (2.8) describes the transfer of spin between the rubidium electron and the noble gas nucleus through binary collisions. The magnetic dipole coupling constant, α , describes the probability of finding the rubidium electron and the noble gas atom in positions where spin transfer could occur. The $\alpha\mathbf{K}\cdot\mathbf{S}$ term can be expanded to show the transfer of spin polarization [23]:

$$\alpha\mathbf{K}\cdot\mathbf{S} = \frac{\alpha}{2} [S^+I^- + S^-I^+] + \alpha S_z I_z \quad (2.9)$$

Equation (2.9), commonly called the flip-flop interaction, shows that spin polarization is only transferred between an electron and nucleus with opposite spin.

The experiments presented in the work do not investigate the quantum mechanics behind SEOP but attempt to optimize SEOP efficiency to produce high polarization and then proceed to use the hyperpolarized noble gas as a contrast agent in magnetic resonance studies. These processes will be discussed in later chapters when relevant.

2.2.4 Relaxation mechanisms

The hyperpolarized spin state does not exist indefinitely; the spins are driven by relaxation mechanisms toward thermal equilibrium over time. Furthermore, in conventional magnetic resonance where spins start at thermal equilibrium and leave equilibrium after a radio frequency pulse are also driven back to equilibrium by the same mechanisms. The two relaxation mechanisms that drive a sample to thermal equilibrium are longitudinal relaxation and transverse relaxation as described by Bloch [24].

2.2.4.1 Longitudinal Relaxation

Longitudinal relaxation, also known as spin-lattice relaxation, is represented by the time constant T_1 . T_1 is related to the rate of the spin system progressing towards thermal equilibrium with the surrounding spins known as the lattice. The relaxation arises from the interaction of the microscopic magnetic field of the nucleus of interest with the microscopic magnetic fields of nuclei in the lattice that cause small magnetic field fluctuations building a net magnetization aligned with applied magnetic field as discussed in *section 2.2.1*. Although small field variations and precession are always present for individual spins, after time an equilibrium is reached where the net magnetic field no longer changes as defined by [24]:

$$dM_z/dt = -(M_z - M_{eq})/T_1. \quad (2.10)$$

In Eq. 2.10, M_z is the existing magnetization and M_{eq} is the magnetization at thermal equilibrium indicating that when M_z is equal to M_{eq} their rate of change of M_z is zero and equilibrium has been researched.

The T_1 inversion recovery experiment, commonly used in conventional (i.e. thermally polarized) systems, is a common method for determining the longitudinal relaxation constant T_1 . First the spin polarization of the system is inverted by applying a 180°_x (π_x) pulse that rotates the bulk magnetization around the x-axis. The magnetization is then sampled at different values of t , showing the return of the bulk magnetization vector to thermal equilibrium. T_1 can be extrapolated from the resulting signal intensities using $M(t) = M_{t=\infty} (1 - 2e^{-t/T_1})$. To run

consecutive experiments it is required to wait at least $5 T_1$ for the magnetization to return almost completely to thermal equilibrium.

For hyperpolarized systems the T_1 inversion recovery experiment is not suitable because the hyperpolarized system trends toward thermal equilibrium and the increased magnetization generated through SEOP or other means is lost, therefore, there is no ‘recovery’ to be exploited. Instead a small flip angle may be used to measure a portion of the magnetization as demonstrated by Gao et al. [25]. The experiment uses a series of small flip angle (θ) excitation pulses, e.g. 12° , that each will rotate the bulk magnetization vector θ° around the x-axis tipping a small component of the magnetic field to the transverse plane to be measured by the receive coil. The series of θ° flip angle experiments will result in an exponential decay following the form $M(t) = \cos(\theta)^{t/\tau} \exp(-t/T_1)$ [25-27], where the $\cos(\theta)$ term accounts for the magnetization consumed by each radio frequency pulse and τ is the time between pulses.

2.2.4.2 Transverse Relaxation

When at thermal equilibrium the bulk nuclear magnetization is parallel to the external magnetic field denoted B_0 , defined as the z-axis. When the bulk magnetization is rotated to the transverse plane by a 90° ($\pi/2$) pulse the entire macroscopic nuclear magnetization precesses at the nuclear Larmor frequency as described previously in *section 2.2.1*. Slight variations in the precession of each nucleus are caused by small differences in magnetic field from the influence of surrounding spins causing

irreversible decay of the transverse magnetization, this decay is described by the time constant T_2 as:

$$dM_{x,y}(t)/dt = -M_{x,y}(t)/T_2 \quad (2.11)$$

Which can be solved for each component as [3]:

$$\begin{aligned} M_y^{nuclear} &= -M_{eq}^{nuclear} \cos(\omega^0 t) \exp(-t/T_2) \\ M_x^{nuclear} &= -M_{eq}^{nuclear} \sin(\omega^0 t) \exp(-t/T_2) \end{aligned} \quad (2.12)$$

Field inhomogeneities across the detection region will also contribute to the apparent T_2 (called T_2^*) because the spins will precess at different frequencies due to the difference in magnetic field strength they experience. The total transverse relaxation constant is described by $1/T_2^* = 1/T_2 + 1/T_2^\dagger$ where T_2^\dagger is the transverse relaxation caused by field inhomogeneities. T_2^* can be determined by from the linewidth (full width at half maximum) of a simple one-dimensional spectrum by $\Delta\nu = 1/\pi T_2^*$.

Inhomogeneous transverse relaxation is a reversible process that can be removed from an experiment using a simple spin echo experiment [28]. A spin echo experiment is designed to investigate the homogeneous transverse relaxation by *cancelling* out field inhomogeneities. An example of a spin echo experiment is shown Figure 2.8. The experiment starts with a 90°_x radio frequency pulse that tips the magnetization onto the x-y plane. Once in the x-y plane the bulk magnetization precesses around the z-axis (B_0). The magnetic field fluctuations cause the spins to precess at slightly different frequency producing a dephasing of the signal as seen in Figure 2.8. Some of the field fluctuations are caused by spin-spin interactions others by field inhomogeneities. After time duration τ a 180°_y pulse rotates

the magnetization around the y-axis and enables the transverse magnetization to refocus into an echo. In the experiment the spin dephasing caused by field inhomogeneities refocuses while spin-spin dephasing is irreversible, allowing for the determination of the T_2 and T_2^\dagger .

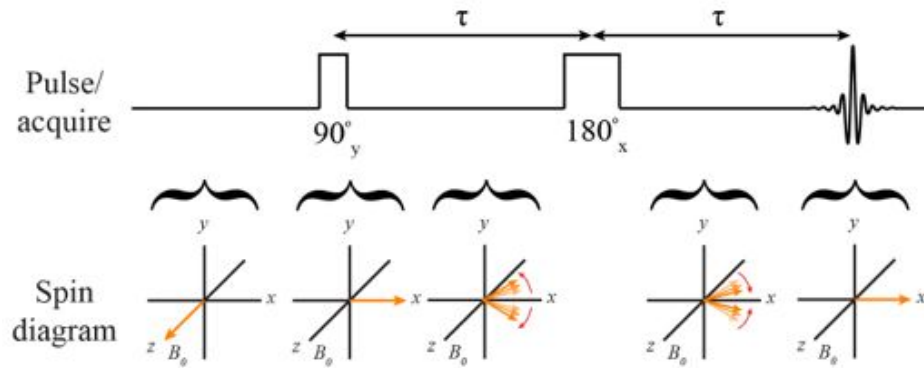


Figure 2.8. Schematic of the spin echo experiment. The bulk magnetization (orange arrow) starts aligned with the external magnetic field (B_0), which is defined as the z-axis. The 90_y pulse rotates the bulk magnetization around the y-axis into the transverse plane. Once in the transverse plane the spins dephase due to field inhomogeneities and natural transverse (spin-spin) relaxation. The 180_x pulse rotates the spins around the x-axis where they will refocus, resulting in the bulk magnetization being refocused along the x-axis as observed as a spin echo. Transverse relaxation due to field inhomogeneities is refocused but the natural spin-spin relaxation is irreversible. The echo from many experiments are acquired varying the time between the 90_y and 180_x pulses resulting in an exponential decay behavior of the spin echo.

A second method to separate T_2 from T_2^* was proposed by Carr and Purcell [29] and modified by Meiboom and Gill [30] to make what is now called a CPMG sequence. The CPMG sequence builds off the spin echo concept, replacing the single echo experiment with a train of echoes made by subsequent 180° pulses that continually refocus the transverse dephasing.

This method can greatly increase the speed of the experiment since the train of echoes can be acquired in a single experiment if conditions are ideal (i.e. adequate signal intensity).

With fluids, such as liquids or gases, diffusion will also be present. When diffusion in a magnetic field gradient exists during a CPMG sequence results in the echo amplitude decay following [29, 31]:

$$S(t) = S_0 \exp\left[(-t/T_2) + \left(-\frac{1}{3}D\gamma^2 G^2 \tau^2 t\right)\right], \quad (2.13)$$

indicating that the apparent transverse relaxation time, T_2 , is [31]:

$$1/T_2^{CPMG} = 1/T_2 + \frac{1}{3}D\gamma^2 G^2 \tau^2. \quad (2.14)$$

In Eq. 2.14 D is diffusion, γ is the gyromagnetic ratio, G is the magnetic field gradient, τ is the time between 90 degree and 180 degree pulse (1/2 the time between 180 pulses on the echo train). Therefore CPMG can be used to probe diffusion in fluids from observing transverse relaxation. This process will be described in greater detail in Chapter 5.

2.2.5 Systems with spin $> 1/2$

As mentioned previously spin $I > 1/2$ denotes that the nucleus has a nuclear electric quadrupole moment (Q) that results from a non-spherical distribution of charge in the nucleus. NMR of quadrupolar nuclei is more challenging than spin $I = 1/2$ nuclei since there are both electric and magnetic influences on the reorientation of the nucleus in a magnetic field [3]. The nuclear electric quadrupole moment enables the nucleus to be sensitive to interactions with electric field gradients (EFGs).

Many quadrupolar isotopes have been investigated as part of solids where rapid transverse relaxation results in very broad signal. In the gaseous

phase the linewidths are much more narrow due to reduced transverse relaxation rate. As gas or vapor EFGs are experienced at the nucleus from distortions of the electron cloud of the atom during collisions and adsorption events [32, 33] as illustrated in Figure 2.9. During the collision, alterations to the shape of the electron cloud and hence a net electric field is experienced by the nucleus, which will reorient itself accordingly. This reduces the longitudinal relaxation time (T_1) that can be detected in the gas phase through rapid exchange. The dependence of the longitudinal relaxation time on the EFGs enables quadrupolar gases to ‘probe’ their surroundings. Unfortunately, the low density of spins requires either high pressures or many experiment repetitions to overcome small signal intensity, limiting the capabilities of this technique.

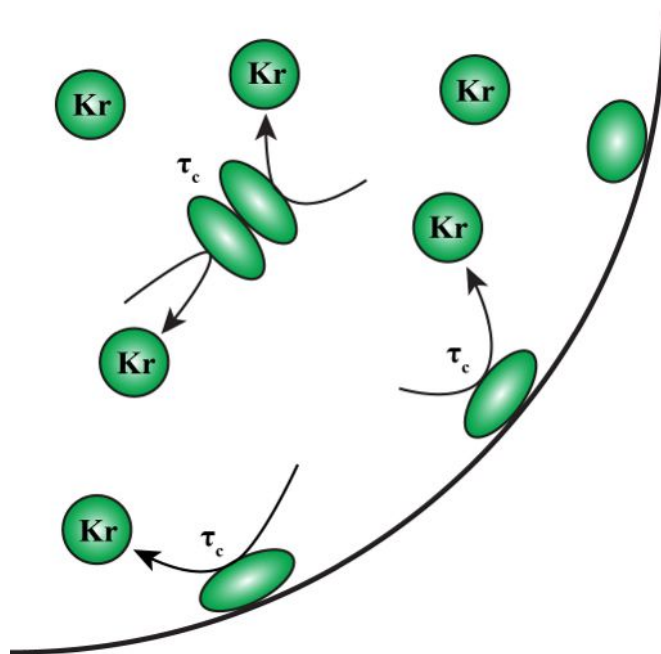


Figure 2.9. Illustration of electric field gradients caused by collisions of ^{83}Kr atoms with time period τ_c .

Hyperpolarization techniques have renewed the interest in gases and vapors of quadrupolar isotopes by overcoming the limited signal. The first investigation showed that the transverse relaxation of hyperpolarized ^{201}Hg ($I = 3/2$) was dependent on the orientation of the NMR cell in the magnetic field [34]. Simpson found that an orientation with an angle of 55° from the magnetic field resulted in the longest T_2 time (i.e. resulted in the greatest signal to noise due to the narrow peak) [34]. The sample orientation found by Simpson corresponds with the “magic angle” proposed by Andrew and colleagues [35] now defined as $\Theta_{magic} = \arctan\sqrt{2} = 54.74^\circ$. Many solid state NMR experiments are designed to rapidly spin a sample at the “magic angle” to average out anisotropic spin interactions (including first order quadrupolar couplings) [3].

The benefits of using the “magic angle” were not observed for either gaseous ^{129}Xe or ^{199}Hg vapor ($I = 1/2$), therefore it was suggested that these angular effects seen in ^{201}Hg and later in ^{83}Kr result from interactions between EFGs and the nuclear quadrupole moment during collisions or adsorption (i.e. momentarily forming a van der Waals interaction) events with the NMR cell wall [32]. Volk and colleagues went on to formulate a theoretical framework for ^{131}Xe to describe relaxation caused by quadrupole moment - EFG interactions [33].

Hyperpolarized noble gas isotopes of ^{21}Ne [36, 37], ^{83}Kr [38-40], and ^{131}Xe [39, 41] have all been used as probes for spectroscopy of materials. As mentioned previously, the EFGs from collision and adsorption events influence the longitudinal relaxation of the nucleus. The longitudinal relaxation rate of ^{83}Kr has shown to be sensitive to the frequency and

duration of the collision and adsorption events that is dependent on by the surface to volume ratio [40], surface chemistry [38-40], and surface temperature [42].

Of the stable quadrupolar noble gas isotopes, only ^{83}Kr has been demonstrated for use in biomedical imaging [39, 43]. ^{131}Xe relaxes more quickly than ^{83}Kr because of the higher polarizability (i.e. capability for electron cloud distortion) of the xenon atom due to the additional electron shell that allows for longer surface adsorption times. Mehring and coworkers used NMR spectroscopy to discover that the activation energy to overcome surface adsorption was 25% greater for ^{131}Xe than for ^{83}Kr as a result the stronger van der Waals interaction [44, 45]. The enhanced EFGs experienced by the nucleus results in shorter T_1 times for ^{131}Xe than ^{83}Kr in porous media [40, 41]. The short T_1 of ^{131}Xe in porous media make it an unlikely candidate for pulmonary studies where surface to volume is exceptionally high.

Conversely ^{21}Ne presumably has slower T_1 relaxation rates than ^{83}Kr due to the smaller, less polarizable electron cloud that will limit surface adsorption. Furthermore, ^{21}Ne has potential to achieve greater signal intensity than krypton based on the gyromagnetic ratio ($\gamma_{\text{Ne}} = -2.11308 \times 10^7 \text{ rad s}^{-1}\text{T}^{-1}$ versus $\gamma_{\text{Kr}} = -1.03310 \times 10^7 \text{ rad s}^{-1}\text{T}^{-1}$ [5]). Unfortunately the natural abundance of ^{21}Ne is very low (0.27%) leading to weak observed signal without isotopically enriching the gas. The usage of isotopically enriched ^{21}Ne for biomedical imaging is promising and warrants future investigation.

2.3 Concepts of Magnetic Resonance Imaging

Magnetic resonance imaging (MRI) is a tool that can non-invasively probe inside objects by observing spin active atoms. The most established use for MRI is to image inside the human body. The concept of magnetic field gradients to spatially resolve nuclear spins was pioneered by Sir Peter Mansfield and Paul Lauterbur who received the Nobel Prize in Medicine in 2003 for their work [46]. The medical community has embraced the utility of MRI making it a common form of medical imaging that is available at many hospitals worldwide.

2.3.1 Spatial encoding

Magnetic resonance imaging is possible because both the frequency and the phase of the nuclear spins can be encoded by magnetic field gradients allowing for the reconstruction of multi-dimensional images. The following description is limited to two-dimensional imaging because only two-dimensional techniques are used later in this work. To explain how an image is collected it is helpful to introduce k-space, which is the spatial-frequency domain or more straightforwardly stated: the Fourier transform of the image space. Frequency encoding is achieved in the direct dimension of k-space by applying a *read* magnetic field gradient across the sample during signal acquisition that makes the magnetic field strength dependant on the location in space. For example, consider a linear magnetic field gradient in B_z along the x-axis of the sample described by $G_x = dB_z/dx$. As a result of the applied gradient, the resonance frequency of the nuclear spins is also dependent on the location in space following the relationship $\omega = -\gamma(B_0 + B_z(x))$, where B_0 is the strength of the static magnetic field

(defined along the z-axis) and $B_z(x)$ is the additional magnetic field from the applied gradient. Each signal acquisition composes a single line in the direct dimension of k-space. In the direct dimension the spatial resolution ($1/\Delta x$) frequency encoding with a linear gradient can be described by [47]:

$$\frac{1}{|\Delta x|} = \left| \frac{\gamma G_x}{2\pi\Delta\nu} \right| \quad (2.10)$$

where, G_x is the magnetic field gradient of B_z along the x-axis, and $\Delta\nu$ is the spread in Larmor frequencies.

Phase encoding of the spins in the second dimension is achieved by applying a magnetic field gradient after the magnetization is rotated into the transverse plane but prior to signal acquisition. The phase encoding gradient causes a linear phase change of the magnetization of the spins depending on their location in space. Incremental steps of the applied gradient strength permit navigating through k-space in individual acquisitions. To generate the complete second dimension, multiple acquisitions are accumulated into a single matrix with each row describing a single line in k-space. The spatial resolution in the phase encoding dimension is determined by the number of phase encoding steps performed.

2.3.2 Gradient-echo imaging

Gradient echo imaging is a versatile technique that utilizes gradients to refocus an echo. This is in contrast to spin echo imaging that uses 180° pulses to refocus echoes. The major benefit of using a gradient echo image over a spin echo image is that a small flip angle may be used for excitation. The small flip angle allows shorter TR in conventional MRI where T_1 relaxation is required to return the signal to maximum as discussed in the

section 2.2.4. Gradient echo imaging is commonly used in hyperpolarized noble gas imaging because spin polarization must be conserved through the entire acquisition.

Gradient echo imaging can be optimized to generate T_1 , T_2 , and T_2^* weighted images based off the selection of TR and TE in conventional imaging. A simple example of a slice selective gradient echo imaging sequence is provided in Figure 2.10. A sinc pulse is used for slice selective excitation of the spins with the slice selection gradients. The length of the sinc pulse determines the excitation bandwidth and subsequently the thickness of the slice. In all images presented later in this work the phase encoding gradient is linearly incremented from negative to positive values to acquire each line of k-space. Alternatively, k-space can be transversed centrically around the 0-gradient line, alternating between positive and negative gradient magnitudes.

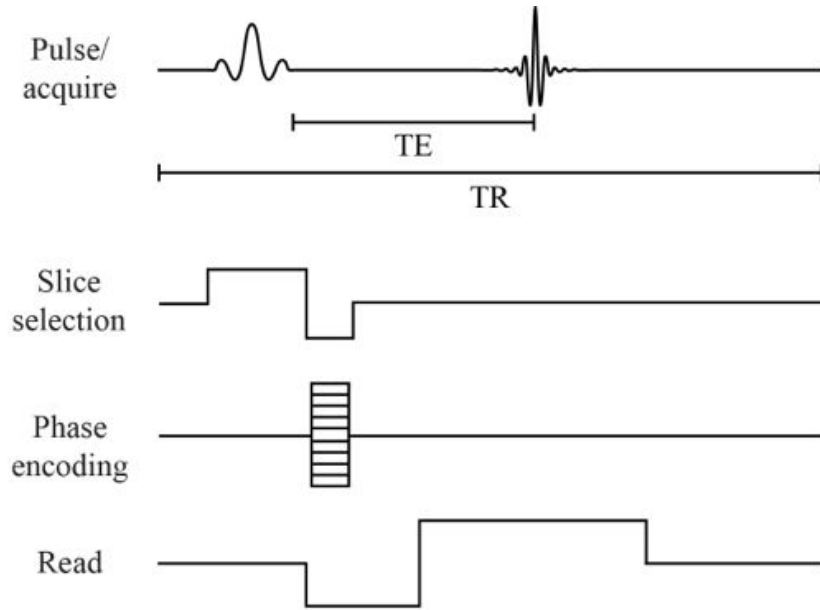


Figure 2.10. Schematic of a slice selective gradient echo imaging sequence. TE is the time between the radio frequency pulse and the center of the gradient echo. TR is the time for each phase-encoded increment. This schematic uses a sinc pulse for slice selection. The strength of the phase encoding gradient is incremented for each line of k-space. The read gradient controls the gradient echo that refocuses the magnetization in the transverse plane for acquisition. Gradient echo diagram is adapted from ref. [47].

2.3.3 Non-equilibrium imaging (variable flip angle)

With growing applications of using hyperpolarized systems, Zhao et al. proposed an imaging method that used a variable flip angle fast low angle shot (VFA FLASH) technique to maintain equal signal intensity throughout image acquisition and completely use all hyperpolarized spin polarization [48]. In the case where acquisition time is much less than T_1 the flip angle θ_n is determined from the current experiment number n of N total experiments by the relation [48]:

$$\theta_n = \arctan\left(\frac{1}{\sqrt{N-n}}\right). \quad (2.11)$$

It is important to note that VFA FLASH is superior in concept to FLASH but can be difficult to implement. VFA FLASH proves effective in small probes that have homogeneous excitation [49]. However, slice selection using VFA FLASH has been shown to create slice profile artefacts [50] and large coils commonly used in MRI tend to have inhomogeneous excitation and that may become problematic without correction [51]. For the small coil sizes of this work these undesirable effects are minimal and VFA FLASH is extensively used.

2.4 References

- [1] A. Abragam, *The Principles of Nuclear Magnetism*, Oxford University Press, Oxford, UK, 1961.
- [2] C.P. Slichter, *Principles of Magnetic Resonance*, 3rd ed., Heidelberg, 1963.
- [3] M.H. Levitt, *Spin Dynamics: Basics of Nuclear Magnetic Resonance*, John Wiley & Sons, LTD, West Sussex, UK, 2001.
- [4] J. Keeler, *Understanding NMR spectroscopy*, Wiley, 2011.
- [5] R. Harris, NMR Nomenclature: Nuclear Spin Properties and Conventions for Chemical Shifts---IUPAC Recommendations, *Journal of Magnetic Resonance*, 156 (2002) 323-326.
- [6] R. Griffin, T. Prisner, High field dynamic nuclear polarization, *the renaissance*, *Phys. Chem. Chem. Phys.*, 12 (2010) 5737-5740.
- [7] A.W. Overhauser, Polarization of Nuclei in Metals, *Phys. Rev.*, 92 (1953) 411-415.
- [8] J.H. Ardenkjaer-Larsen, B. Fridlund, A. Gram, G. Hansson, L. Hansson, M.H. Lerche, R. Servin, M. Thaning, K. Golman, Increase in signal-to-noise ratio of > 10,000 times in liquid-state NMR, *Proceedings of the National Academy of Sciences of the United States of America*, 100 (2003) 10158-10163.
- [9] K. Golman, J.H. Ardenaer-Larsen, J.S. Petersson, S. Mansson, I. Leunbach, Molecular imaging with endogenous substances, *Proceedings of the National Academy of Sciences of the United States of America*, 100 (2003) 10435-10439.
- [10] K. Golman, R. in't Zandt, M. Thaning, Real-time metabolic imaging, *Proceedings of the National Academy of Sciences of the United States of America*, 103 (2006) 11270-11275.
- [11] M.A. Bouchiat, T.R. Carver, C.M. Varnum, Nuclear polarization in He-3 gas induced by optical pumping and dipolar exchange, *Phys. Rev. Lett.*, 5 (1960) 373-375.
- [12] B.C. Grover, Noble-Gas Nmr Detection through Noble-Gas-Rubidium Hyperfine Contact Interaction, *Phys. Rev. Lett.*, 40 (1978) 391-392.
- [13] T.G. Walker, W. Happer, Spin-exchange optical pumping of noble-gas nuclei, *Review of Modern Physics*, 69 (1997) 629-642.
- [14] I.C. Ruset, S. Ketel, F.W. Hersman, Optical pumping system design for large production of hyperpolarized Xe-129, *Phys. Rev. Lett.*, 96 (2006) 053002-053004.
- [15] D.M.L. Lilburn, G.E. Pavlovskaya, T. Meersmann, Perspectives of hyperpolarized noble gas MRI beyond ³He, *Journal of Magnetic Resonance*, 229 (2013) 173-186.
- [16] J. Liran, J. Pietras, J. Camparo, W. Happer, Optical pumping of cesium atoms with second resonance light, *Optics Communications*, 31 (1979) 169-173.
- [17] N. Bhaskar, J. Pietras, J. Camparo, W. Happer, J. Liran, Spin destruction in collisions between cesium atoms, *Phys. Rev. Lett.*, 44 (1980) 930-933.

- [18] N. Whiting, N.A. Eschmann, B.M. Goodson, M.J. Barlow, (129)Xe-Cs (D(1), D(2)) versus (129)Xe-Rb (D(1)) spin-exchange optical pumping at high xenon densities using high-power laser diode arrays, *Physical Review A*, 83 (2011) 053428.
- [19] N.D. Bhaskar, M. Hou, M. Ligare, B. Suleman, W. Happer, Role of Na-Xe molecules in spin relaxation of optically pumped Na in Xe gas, *Physical Review A*, 22 (1980) 2710-2716.
- [20] E. Babcock, I. Nelson, S. Kadlecik, B. Driehuys, L.W. Anderson, F.W. Hersman, T.G. Walker, Hybrid Spin-Exchange Optical Pumping of ^3He , *Phys. Rev. Lett.*, 91 (2003) 123003.
- [21] W. Happer, Optical-Pumping, *Reviews of Modern Physics*, 44 (1972) 169-249.
- [22] W. Happer, E. Miron, S. Schaefer, D. Schreiber, W.A. Vanwijngaarden, X. Zeng, Polarization of the Nuclear Spins of Noble-Gas Atoms by Spin Exchange with Optically Pumped Alkali-Metal Atoms, *Physical Review A*, 29 (1984) 3092-3110.
- [23] E. Brunner, Enhancement of surface and biological magnetic resonance using laser-polarized noble gases, *Concepts in Magnetic Resonance*, 11 (1999) 313-335.
- [24] F. Bloch, Nuclear Induction, *Physical Review*, 70 (1946) 460-474.
- [25] J.H. Gao, L. Lemen, J.H. Xiong, B. Patyal, P.T. Fox, Magnetization and diffusion effects in NMR imaging of hyperpolarized substances, *Magn. Reson. Med.*, 37 (1997) 153-158.
- [26] Z.I. Cleveland, G.E. Pavlovskaya, K.F. Stupic, J.B. Wooten, J.E. Repine, T. Meersmann, Detection of Tobacco Smoke Deposition by Hyperpolarized Krypton-83 MRI, *Magnetic Resonance Imaging*, 26 (2008) 270-278.
- [27] K.F. Stupic, N.D. Elkins, G.E. Pavlovskaya, J.E. Repine, T. Meersmann, Effects of pulmonary inhalation on hyperpolarized krypton-83 magnetic resonance T-1 relaxation, *Physics in Medicine and Biology*, 56 (2011) 3731-3748.
- [28] E.L. Hahn, D.E. Maxwell, Spin Echo Measurements of Nuclear Spin Coupling in Molecules, *Physical Review*, 88 (1952) 1070-1084.
- [29] H.Y. Carr, E.M. Purcell, Effects of Diffusion on Free Precession in Nuclear Magnetic Resonance Experiments, *Phys. Rev.*, 94 (1954) 630-638.
- [30] S. Meiboom, D. Gill, Modified Spin-Echo Method for Measuring Nuclear Relaxation Times, *The Review of Scientific Instruments*, 29 (1958) 688-691.
- [31] H.C. Torrey, Bloch equations with diffusion terms, *Physical Review*, 104 (1956) 563-565.
- [32] C.H. Volk, J.G. Mark, B.C. Grover, Spin Dephasing of Kr-83, *Physical Review A*, 20 (1979) 2381-2388.
- [33] T.M. Kwon, J.G. Mark, C.H. Volk, Quadrupole Nuclear-Spin Relaxation of Xe-131 in the Presence of Rubidium Vapor, *Physical Review A*, 24 (1981) 1894-1903.
- [34] J.H. Simpson, NMR Frequency Splitting of Hg-201 Signals Due to Collisions with a Fused Silica Surface, *Bulletin of the American Physical Society*, 23 (1978) 394-395.

- [35] E.R. Andrew, A. Bradbury, R.G. Eades, Removal of Dipolar Broadening of Nuclear Magnetic Resonance Spectra of Solids by Specimen Rotation, *Nature*, 183 (1959) 1802-1803.
- [36] T.E. Chupp, K.P. Coulter, Polarization of Ne-21 by Spin Exchange with Optically Pumped Rb Vapor, *Phys. Rev. Lett.*, 55 (1985) 1074-1077.
- [37] R.K. Ghosh, Spin exchange optical pumping of neon and its applications, in: *Physics*, Princeton University, Princeton, NJ, USA, 2009.
- [38] Z.I. Cleveland, K.F. Stupic, G.E. Pavlovskaya, J.E. Repine, J.B. Wooten, T. Meersmann, Hyperpolarized ^{83}Kr and ^{129}Xe NMR Relaxation Measurements of Hydrated Surfaces: Implications for Materials Science and Pulmonary Diagnostics, *Journal of the American Chemical Society*, 129 (2007) 1784-1792.
- [39] G.E. Pavlovskaya, Z.I. Cleveland, K.F. Stupic, T. Meersmann, Hyperpolarized Krypton-83 as a New Contrast Agent for Magnetic Resonance Imaging, *Proceedings of the National Academy of Sciences of the United States of America*, 102 (2005) 18275-18279.
- [40] K.F. Stupic, Z.I. Cleveland, G.E. Pavlovskaya, T. Meersmann, Quadrupolar Relaxation of Hyperpolarized Krypton-83 as a Probe for Surfaces, *Solid State Nuclear Magnetic Resonance*, 29 (2006) 79-84.
- [41] K.F. Stupic, Z.I. Cleveland, G.E. Pavlovskaya, T. Meersmann, Hyperpolarized Xe-131 NMR spectroscopy, *Journal of Magnetic Resonance*, 208 (2011) 58-69.
- [42] Z.I. Cleveland, G.E. Pavlovskaya, K.F. Stupic, C.F. LeNoir, T. Meersmann, Exploring hyperpolarized ^{83}Kr by remotely detected NMR relaxometry, *Journal of Chemical Physics*, 124 (2006) 044312.
- [43] Z.I. Cleveland, G.E. Pavlovskaya, N.D. Elkins, K.F. Stupic, J.E. Repine, T. Meersmann, Hyperpolarized Kr-83 MRI of lungs, *Journal of Magnetic Resonance*, 195 (2008) 232-237.
- [44] R. Butscher, G. Wäckerle, M. Mehring, Nuclear quadrupole interaction of highly polarized gas phase ^{131}Xe with a glass surface, *Journal of Chemical Physics*, 100 (1994) 6923-6933.
- [45] R. Butscher, G. Wäckerle, M. Mehring, Nuclear quadrupole surface interaction of gas phase ^{83}Kr : comparison with ^{131}Xe , *Chemical Physics Letters*, 249 (1996) 444-450.
- [46] The Nobel Prize in Physiology or Medicine 2003, http://www.nobelprize.org/nobel_prizes/medicine/laureates/2003/, Nobleprize.org, 11 May 2013.
- [47] B. Blumich, *NMR imaging of materials*, Oxford University Press, 2000.
- [48] L. Zhao, R. Mulkern, C.H. Tseng, D. Williamson, S. Patz, R. Kraft, R.L. Walsworth, F.A. Jolesz, M.S. Albert, Gradient-echo imaging considerations for hyperpolarized Xe-129 MR, *Journal of Magnetic Resonance Series B*, 113 (1996) 179-183.
- [49] G.E. Santyr, W.W. Lam, J.M. Parra-Robles, T.M. Taves, A.V. Ouriadov, Hyperpolarized noble gas magnetic resonance imaging of the animal lung: Approaches and applications, *Journal of Applied Physics*, 105 (2009) 102004-102013.
- [50] M.H. Deppe, K. Teh, J. Parra-Robles, K.J. Lee, J.M. Wild, Slice profile effects in 2D slice-selective MRI of hyperpolarized nuclei, *Journal of Magnetic Resonance*, 202 (2010) 180-189.

[51] G.E. Santyr, W.W. Lam, A. Ouriadov, Rapid and efficient mapping of regional ventilation in the rat lung using hyperpolarized He-3 with Flip Angle Variation for Offset of RF and Relaxation (FAVOR), *Magn. Reson. Med.*, 59 (2008) 1304-1310.

Chapter 3: Pathway to cryogen-free production of hyperpolarized ^{83}Kr and ^{129}Xe

Data presented in this chapter have been published in an article of PLoS One entitled *Pathway to Cryogen Free Production of Hyperpolarized Krypton-83 and Xenon-129* by Joseph S. Six, Theodore Hughes-Riley, Karl F. Stupic, Galina E. Pavlovskaya, and Thomas Meersmann [1]. Mr. Six and Mr. Hughes-Riley performed the low pressure SEOP experiments that are presented in this chapter. Mr. Six and Dr. Pavlovskaya analyzed the data to extrapolate physical parameters. Dr. Stupic and Dr. Pavlovskaya designed and constructed the noble gas hyperpolarizer. Professor Meersmann and Mr. Six wrote the paper.

3.1 Introduction

Spin exchange optical pumping (SEOP) of ^{129}Xe and ^{83}Kr is typically completed in helium - nitrogen mixtures with low concentrations of the noble gas. In the case of ^{129}Xe , the hyperpolarized xenon is separated from the other gasses after the SEOP process by a freeze-thawing cycle using a cold trap at 77 K [2-5]. This process is not viable for hyperpolarized ^{83}Kr because of its rapid quadrupolar relaxation in the frozen state [6, 7]. Although cryogenic separation of hyperpolarized ^{129}Xe is straightforward in a physics or chemistry laboratory with acceptable losses [5, 8], it would be

desirable to eliminate cryogen usage to facilitate hyperpolarized ^{129}Xe MRI applications in typical clinical and pre-clinical settings.

A high noble gas concentration in the SEOP gas mixtures would reduce the need for gas separation and could open up the pathway for cryogen free production of hyperpolarized noble gas MRI. Unfortunately, a high noble gas density, $[\text{NG}]$, adversely affects the obtained noble gas spin polarization, P_{NG} , because it reduces the alkali metal electron spin polarization in the SEOP process. The adverse effect of $[\text{NG}]$ on P_{NG} is further exacerbated by the diminishing effect of $[\text{NG}]$ upon the spin exchange rate, γ_{SE} [2, 9-12]. If cryogenic separation is omitted, a trade off between noble gas concentration and obtained spin polarization exists. For example, a spin polarization of approximately 1% was generated in a previously reported ^{83}Kr SEOP experiments using a mixture of 95% krypton with 5% nitrogen. Reducing the noble gas concentration to 25% krypton led to four fold higher spin polarization but the MR signal did not improve because polarization increase was offset by the noble gas dilution [13].

A potential solution for the conundrum to generate high P_{NG} at high noble gas concentrations is to reduce $[\text{NG}]$ through decreasing the total pressure of the gas mixture containing a high percentage of the respective noble gas. Optical pumping far below ambient pressure had been the method of choice in many of the pioneering SEOP studies [14-18], but low pressure SEOP was largely abandoned with the advent of high power solid state lasers that provide better polarization at elevated gas pressures due to pressure broadening of the rubidium D_1 transition. However, line narrowed high power diode array lasers have become available [10, 17, 19] that make

pressure broadening less beneficial. Even non-narrowed (typically 2 nm linewidth) solid state lasers benefit from ^{129}Xe SEOP being at a gas pressure below ambient, as previously demonstrated by Imai et al. [20]. Unfortunately high spin polarization >12% was obtained (at 15 kPa pressure) only for mixtures with low xenon concentration leaving cryogenic separation as a remaining desirable step. However, the work by Imai et al. also demonstrated that recompression of hyperpolarized ^{129}Xe to ambient pressure after SEOP is feasible without significant losses in spin polarization. Recompression of the hyperpolarized noble gas to ambient pressure would be a crucial step for intended low pressure SEOP usage for *in vivo* MRI applications.

In this work, ‘stopped flow’ (batch mode) SEOP [18] was utilized. In contrast to ‘continuous flow’ SEOP [2-5, 21-24] that is technically more demanding [3, 5, 24], ‘stopped flow’ SEOP is applied to a stagnant gas mixture until the steady state polarization has been reached. The hyperpolarized noble gas is then shuttled through pressure equalization into a pre-evacuated chamber for high field MR detection without re-pressurization. The advantage of ‘stopped flow’ ^{129}Xe SEOP was noted previously [25] and remarkably high ^{129}Xe spin polarization were reported recently [10]. With the noticeable exception of the work by Fujiwara and co-workers [26, 27], pulmonary MRI typically uses hyperpolarized gas in batched volumes. Therefore stopped flow SEOP may be of interest for pulmonary hyperpolarized ^{129}Xe MRI applications, in particular if it provides some advantages beyond current continuous flow methods.

To date, stopped flow SEOP is the only viable technique for hyperpolarizing noble gases with nuclear electric quadrupolar moment such as ^{83}Kr [28, 29]. In this study, stopped-flow SEOP was investigated with mixtures containing 5 - 78% of either krypton or xenon at total gas pressures ranging from 5 kPa to 200 kPa and above. Current theory was applied to attempt a qualitative interpretation of the experimental data.

3.2 Experimental

3.2.1 Stopped flow spin exchange optical pumping

The experimental setup is sketched in Figure 3.1. Mixtures containing various concentrations of ^{129}Xe and ^{83}Kr were hyperpolarized in borosilicate glass SEOP cells (length = 120 mm, inner diameter = 28 mm) containing ~1 g rubidium (99.75%; Alfa Aesar, Heysham, England, UK). The SEOP cell was housed in an aluminum oven with quartz windows and temperature controlled using heated air. The fringe field of a 9.4 T superconducting magnet provided the magnetic field of $B_0 \approx 0.05$ T for the SEOP process. Unless otherwise specified, a line narrowed diode-array laser system (30 W, 0.25 nm linewidth Comet Module, Spectral Physics, Santa Clara, CA, USA) tuned to the D_1 transition of rubidium (794.7 nm) was used to irradiate the SEOP cell with collimated, circularly polarized light of 23.3 W power (incident at SEOP cell).

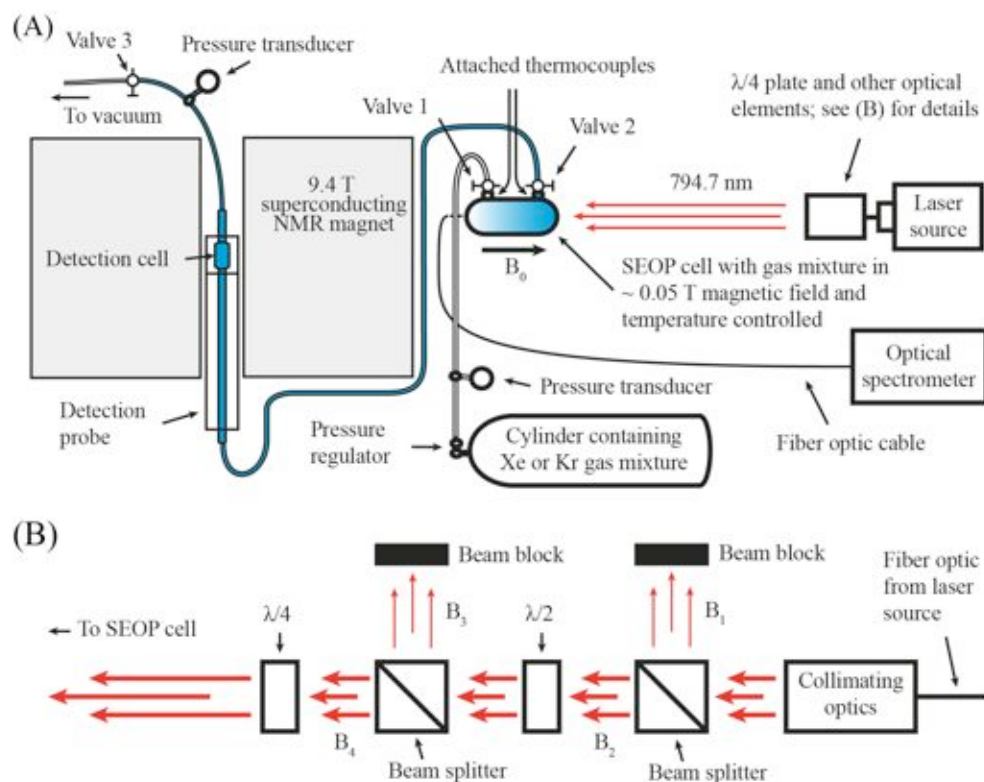


Figure 3.1. The experimental setup used for stopped flow SEOP. **(A)** Transfer of hyperpolarized gas to NMR magnet for high-field detection. The hyperpolarized mixture is transferred to the detection cell by pressure equalization after the noble gas mixtures are hyperpolarized in the SEOP cell for a time period of t_d by the stopped flow SEOP method. **(B)** Outline of the optical elements used in Figure 3.1A. The elements $\lambda/2$ plate and second beam splitter were used to control the laser irradiation (B_4) to the SEOP cell (i.e. adjustment of the B_4/B_3 ratio - for details of power dependent measurements see *section 3.2.2*).

Steady state, nuclear spin polarization was reached after 6 minutes for ^{129}Xe SEOP and after approximately 18 minutes for ^{83}Kr SEOP. However, due to time restraints ^{83}Kr SEOP times of only 8 minutes were used resulting to 80% completion of the built up, as verified by measurements at both high and low SEOP pressure. During SEOP, the gas mixture was contained within the SEOP cell with valve 2 closed (see Figure 3.1A). Valve 1 was kept open initially to allow for pressure monitoring but

was closed approximately 2 minutes before delivery. The borosilicate detection cell and PFA transfer tubing were evacuated (valve 3 open) during the SEOP duration. After SEOP completion, valve 3 was closed and valve 2 opened. Pressure equalization caused rapid hyperpolarized gas transfer via 1.5 mm (inner diameter) PFA tubing into the 15 mm borosilicate detection cell. The detection cell located within a 9.4 T superconducting magnet and a Magritek Kea 2 spectrometer (Wellington, NZ) with custom-built probes tuned to the resonance frequencies of ^{129}Xe (110.5 MHz) and ^{83}Kr (15.4 MHz) were used for detection.

3.2.2 Laser power adjustment and optical measurements

In addition to the line narrowed Comet laser, two broadband 30 W Coherent (Santa Clara, CA, USA) fiber array packaged (FAP) lasers were also used as a non-narrowed laser system (2 nm linewidth) for SEOP efficiency comparison with the line narrowed Comet laser. Due to the experimental setting only 15.6 W of FAP laser power was used to irradiate the SEOP cell. To have a proper comparison between the narrowed and broadband laser systems the laser power of the narrowed laser was reduced to approximately match the power of the broadband system. Figure 3.1B displays the optical elements used to reduce the power of the Comet laser. The first beam splitter in the path of the laser light was present in all experiments in this work and ensured that only a single plane of linearly polarized light would continue toward the SEOP cell. It was found that $B_2 = 19 B_1$ for the highly linear polarized Comet system and $B_2 = B_1$ for the FAP system (i.e. no linear polarization remaining due to passage through the long fibre optic cable of the FAP system). Laser power control was obtained

through a $\lambda/2$ wave plate followed by a second beam splitter. By rotating the $\lambda/2$ wave plate the laser rejection (B_3) was controlled, thus enabling the power control for the laser irradiation (B_4) of the SEOP cell without changes in the irradiation profile (i.e. wavelength and spatial distribution). The incident laser power was measured at the SEOP cell using a Coherent PM150-50C water-cooled power meter. The same power adjustment procedure was also used for the power dependent measurements described in *section 3.4.9*.

The rubidium absorption linewidth in the presence of pure krypton, xenon, nitrogen, and a xenon - nitrogen mixture was measured through absorption experiments similar to those by Driehuys and co-workers [30]. An incandescent light source with a consistent emission over the observed wavelengths irradiated the SEOP cell in place of the laser. A fibre optic cable leading to the optical spectrometer, HR2000+ Ocean Optics (Dunedin, FL, USA) with a spectral resolution of 0.04 nm was placed at the rear of the SEOP cell to measure the D_1 absorption line width at 794.72 – 795.15 nm.

3.2.3 Temperature control

The temperature of the SEOP cell inside the oven was maintained by an inflow of heated air near the back of the cell. Two thermocouples attached to the SEOP cell were used to measure the cell temperature. The first thermocouple was placed at the frontal region of the cell (i.e. in approximately 10 mm distance from the laser illuminated window) where it was carefully shielded from infrared radiation, while the second thermocouple was positioned near the back region of the cell. The data from the two thermocouples were fed into a temperature controller. With this

setup, the temperature controlled incoming air provided sufficiently stable temperature conditions, although the actual temperature inside the cell could not be determined. The temperature was measured on the surface of the SEOP cell at the thermocouple locations during ramping and steady-state processes. Typical temperature difference across the cell was less than 10 K after the steady-state conditions were reached.

3.2.4 Gas mixtures

Research grade xenon (99.995% pure; natural abundance, 26.4% ^{129}Xe ; Airgas, Rednor, PA, USA), krypton (99.995% pure; natural abundance, 11.5% ^{83}Kr ; Airgas, Rednor, PA, USA), and nitrogen (99.999% pure, Air Liquide, Coleshill, UK) were used to prepare the gas mixtures used in this study. The mixtures with varying noble gas contents were prepared prior to the SEOP experiments using a custom built gas mixing system. The ‘standard mixture’ described in *section 3.2.6* required the use of research grade helium (99.999% pure, Air Liquide, Coleshill, UK) in addition to other gases.

3.2.5 Determination of obtained polarization values

For the determination of the actual polarization value, the integrated signal intensities of the hyperpolarized noble gases were compared to the integrated signal intensity of a thermally polarized sample of the respective gas. For the thermal ^{83}Kr NMR measurement, a 15 mm borosilicate sample tube was pressurized to 560 kPa of natural abundance krypton gas leading to $T_1 \approx 65$ s at 298 K [31]. Data were averaged from 360 acquisitions with a 360 s recycle delay time between pulses. Similarly, for the ^{129}Xe thermal measurement, a sample tube was pressurized to 500 kPa containing 4

amagat of natural abundance xenon gas and approximately 1 amagat of O₂ in order to reduce the longitudinal relaxation time to $T_1 < 5$ s ($T_1 \approx 2.6$ s at 4.7 T [32]). Data were averaged from 120 acquisitions with 120 s recycle delay time between pulses. Taking into account the differences in concentration, pressure, and number of scans the integrated intensities from the thermal samples were compared with the integrated intensity of the hyperpolarized samples to obtain the polarization enhancement over the thermal spin polarization.

For nuclei with arbitrary spin I the spin polarization P in a thermal equilibrium is given [29]:

$$P = \frac{|\gamma| \hbar B_0}{3k_B T} (I + 1) \quad (3.1)$$

with γ as the gyromagnetic ratio, k_B as the Boltzmann constant, and $\hbar = h/2\pi$ as the Planck constant. Eq. 3.1 assumes Boltzmann population distribution at high temperatures where $T \gg |\gamma| \hbar B_0 / k_B$, a condition that is fulfilled for the thermally polarized samples described above. Note that the thermal samples and the ‘standard mixture’ (described in *section 3.2.6*) were rerecorded with a second NMR system (Bruker, Avance III at 9.4 T) in order to confirm the obtained hyperpolarization values with the Kea 2 spectrometer.

3.2.6 Accuracy of polarization measurements

The SEOP generated polarization can be measured with high precision through high field NMR spectroscopy. However, the polarization values will scatter due to fluctuations in the SEOP cell. For example, the cell

surface will ‘cure’ after reloading with rubidium metal, probably due to redistribution of surface condensed rubidium, and the obtained hyperpolarization will increase initially for up to a few hours for cells newly loaded with rubidium. Further, contamination with oxygen, carbon dioxide, or water will lead to a slow decrease in the obtainable hyperpolarization. Some of the cells that appear to be nearly identical lead to slightly different hyperpolarization values. Because of the many factors that may influence these measurements data sampling was randomized during parts of the experiment. To characterize experimental variation in cell performance over time a polarization value was obtained for a standard mixture (5% xenon, 5% nitrogen, 90% helium at 230 ± 20 kPa and 373 K). This polarization value, averaged over a few experiments, was measured to be $44.0 \pm 5.4\%$ and was further used for the ‘quality control’ test of a given SEOP cell. Three different SEOP cells that consistently achieved polarization values in this range were used during the course of the experiments. If the achievable polarization of a cell fell outside this range, it was cleaned and refilled with rubidium. Errors reported for the polarization measurements are based on the $\pm 5.4\%$ error of the standard mixture and scaled accordingly.

3.2.7 Data analysis

Data analysis was performed using Igor Pro Version 6.2 from Wavemetrics (Lake Oswego, OR, USA). Fitting parameters for spin-exchange optical pumping were extracted using built-in non-linear least squares fitting algorithms.

3.3 Background to the ^{83}Kr and ^{129}Xe SEOP experiments

The unit ‘amagat’ for the number density $[M_i]$ of gas phase atoms or molecules is often used for convenience. In this work an amagat is defined as the density of an ideal gas at standard pressure and temperature of 101.325 kPa and 273.15 K and therefore $1 \text{ amagat} = 2.6868 \times 10^{25} \text{ m}^{-3}$. Note that the amagat was historically defined as the density of the specific gas at standard pressure and temperature resulting to the slightly different value for instance for xenon with $2.7048 \times 10^{25} \text{ m}^{-3}$ [33]. The small difference of less than 1% between the two definitions indicates almost ideal gas behavior for xenon at this condition.

3.3.1 Expected pressure dependence

The increase of the noble gas spin polarization as a function of the total pressure decrease is expected from [2, 34]:

$$P_{NG} = \frac{\gamma_{SE}}{\gamma_{SE} + \Gamma} \cdot \frac{\gamma_{op}}{\gamma_{op} + \gamma_{trap} + \gamma_{vdW} + \sum_i \kappa_{sd}^i [M_i]} \left(1 - e^{-(\gamma_{SE} + \Gamma)t_p}\right), \quad (3.2)$$

where γ_{op} is the optical pumping rate caused by laser irradiation of the alkali metal atoms (i.e. by irradiation of rubidium (Rb) atoms with circular polarized light at the D_1 transition at 794.7 nm for all experiments described in this work). In principle, the rate $\gamma_{op}(z)$ is a function of position within the pump cell due to the weakening of the laser in the optically thick medium [23, 35], however for the purpose of this work an averaged value γ_{op} is assumed for simplicity, noting also the presence of significant gas convection in the SEOP cell [36]. The rate constant γ_{SE} describes the spin exchange rate and Γ is the longitudinal relaxation rate of the noble gas

atoms. The polarization, P_{NG} , increases with increasing SEOP time, t_p , until the contribution from the exponential term in Eq. 3.2 becomes negligible and the steady state value of polarization P_{NG} has been reached. The rubidium electron spin polarization

$$P_{\text{Rb}} = \gamma_{op} \cdot \left(\gamma_{op} + \gamma_{trap} + \gamma_{vdW} + \sum_i \kappa_{sd}^i [M_i] \right)^{-1}$$

is limited by spin depolarizing collisions with inert gas atoms described by the gas (M_i) specific rate constants κ_{sd}^i multiplied by the number density of the corresponding gas,

$[M_i]$. A further limitation is through radiation trapping described by the

rate constant γ_{trap} [12] that is further discussed below (see *section 3.3.3*)

and by the rate constant γ_{vdW} that is caused by spin rotation interactions (i.e.

interaction of the rubidium 5s electron spin with rubidium- M_i molecular rotation - see *section 3.3.4*). A major contribution to the rubidium

depolarization in the gas phase at SEOP pressures $p_{tot} > 20 - 50$ kPa is

caused by binary atomic collision. The rate constants caused by these interactions are directly dependent on the density of the respective atoms

[15]. The rate constant of xenon is $\kappa_{sd}^{Xe} = 5.2 \times 10^{-21} \text{ m}^3\text{s}^{-1}$ and is about 500

times larger than that of molecular nitrogen and more than 3 order of magnitude larger than that of helium (see Table 3.1). Similarly, the rate

constant of krypton, $\kappa_{sd}^{Kr} = 1.1 \times 10^{-21} \text{ m}^3\text{s}^{-1}$, is a factor of 100 higher than

that of molecular nitrogen. Therefore, even in the 95% nitrogen and 5%

krypton gas mixture the contribution of molecular nitrogen to the overall

rubidium electron spin relaxation is only about 14% of the total gas phase

relaxation caused by binary collisions. Moreover, in all other mixtures used

in this work the nitrogen contribution to rubidium 5s electron spin depolarization through binary collisions is assumed to be below 4%.

Table 3.1. ^{83}Kr and ^{129}Xe literature rate constants used in Eq. 3.2.

Collision pair	Rubidium spin depolarization rate constants $\kappa_{sd} / \text{m}^3 \text{s}^{-1}$	Spin exchange rate of van der Waals complexes ^C $\gamma_{RbNG} / \text{s}^{-1}$	Binary spin exchange: $\langle \sigma v \rangle / \text{m}^3 \text{s}^{-1}$	Characteristic pressure $b = p_0 (NG) / p_0 (N_2)$
Rb-Xe	5.2×10^{-21} ^A	$\approx 9.7 \times 10^3$ ^D $\approx 2.8 \times 10^3$ ^E	1.0×10^{-21} ^D 2.2×10^{-22} ^G 3.7×10^{-22} ^E	
Rb-Kr	$\approx 1.1 \times 10^{-21}$ ^A	≈ 6.0 ^F	2.1×10^{-24} ^F	
Rb-N ₂	$\approx 9.4 \times 10^{-24}$ ^B			
Rb-He	$\approx 2.3 \times 10^{-24}$ ^B			
Rb-Rb	$\approx 8.1 \times 10^{-19}$ ^A			
Xe-N ₂				0.275 ^E
Kr-N ₂				1.90 ^F

^AFrom ref. [15] measured at 300 K

^BFrom ref. [35]

^CUsing $\gamma_{RbNG} = (\gamma_M \zeta)_{RbNG}$, where $\zeta = 0.095$ (assuming P_{Rb} close to 100%)

^DFrom ref. [37]

^EFrom ref. [9], values from this reference were used in calculations where multiple values have been reported

^FAt 363 K from ref. [38]

^GFrom ref. [39] for $T = 373$ K and $B_0 = 0$ T

3.3.2 Contribution of rubidium-rubidium collisions

Unlike typical experiments at high SEOP pressure, depolarization of the rubidium electron spin due to rubidium-rubidium atom collisions may contribute significantly to rubidium depolarization in the gas phase at low SEOP gas densities. The fairly large corresponding rate constant $\kappa_{sd}^{Rb-Rb} \approx 8.1 \times 10^{-19} \text{ m}^3 \text{ s}^{-1}$ indicates that electron magnetic dipole – dipole interactions are responsible for the relaxation mechanism [35]. Depolarization due to rubidium-rubidium collisions depends on the rubidium number density [Rb] and is therefore a function of the SEOP cell temperature. An empirical equation (replacing an older, similar equation by

Killian [40]) for [Rb] in m^{-3} as a function of temperature T in Kelvin is [41, 42]:

$$[\text{Rb}]^T = \frac{10^{32.18 - \frac{4040}{T}}}{T}. \quad (3.3)$$

Using Eq. 3.3 one obtains that $[\text{Rb}]^{373\text{K}} = 6.0 \times 10^{18} \text{ m}^{-3}$ at 373 K. However Eq. 3.3 should be used with caution for rubidium concentration calculations as uncertainties arise from the difficulty of proper temperature monitoring inside the SEOP cell during on-resonance irradiation with a high-powered laser as explained further in the text (see *section 3.4.3* for discussion of the correction factor, c^{Rb} , to [Rb]).

The potential uncertainty in temperature is quite inconsequential for the rubidium depolarization in ^{129}Xe SEOP since the rubidium density at a temperature of 373 K leads to a relaxation rate of $[\text{Rb}]^{373\text{K}} \cdot \kappa_{sd}^{\text{Rb-Rb}} = 4.8 \text{ s}^{-1}$ that contributes less than 2% to the rubidium gas phase relaxation at the lowest pressure (5 kPa) and the lowest xenon concentration (5.0%) used. The significance of rubidium-rubidium collisions to the rubidium depolarization decreases further as the total gas pressure and the xenon concentration increase. However, the situation is quite different in ^{83}Kr SEOP. Firstly, the rate constant κ_{sd}^{Kr} is about 5 times smaller than κ_{sd}^{Xe} , thus increasing the relative importance of $\kappa_{sd}^{\text{Rb-Rb}}$ for the rubidium depolarization. Secondly, ^{83}Kr SEOP produces the highest nuclear spin polarization at 433 K and, according to Eq. 3.3, $[\text{Rb}]^{433\text{K}} = 1.6 \times 10^{20} \text{ m}^{-3}$. This translates into 27 fold increase in rubidium concentration as compared to $[\text{Rb}]^{373\text{K}}$ and rubidium-rubidium collisions contribute therefore significantly to the

rubidium depolarization, in particular at low SEOP pressures. For example, at 30 kPa total gas pressure the contribution of $[Rb]^{433K} \cdot \kappa_{sd}^{Rb-Rb}$ to the rubidium gas phase depolarization ranges from approximately 2% (for the 74% krypton mixture) to 5% (for the 25% krypton mixture) to about 20% for the leanest (5%) krypton mixture. Therefore uncertainties in SEOP temperature (and therefore [Rb]) can affect the second term in Eq. 3.2 for ^{83}Kr SEOP.

3.3.3 Radiation trapping

Molecular nitrogen is an important component of an SEOP gas mixture because it can, unlike mono-atomic noble gasses, dissipate energy from excited rubidium electronic states into vibrational modes [14, 43]. This non-radiative relaxation pathway reduces rubidium fluorescence, depending on the nitrogen number density [12]. In SEOP mixtures with high rubidium density [Rb], fluorescence may be detrimental to the rubidium spin polarization because it can lead to radiation trapping where a single incident circularly polarized photon gives rise to multiple scattered photons that are arbitrarily polarized. Wagshul and Chupp [43] have reported a formula based on earlier experimental work [44] that quantifies the extent of quenching through molecular nitrogen. A slight modification of this formula, i.e. multiplication with the $\gamma_{trap}^{[N_2]=0}$ term from SEOP in the absence of nitrogen, leads to an expression similar to the one reported by Brunner and co-workers [36]:

$$\gamma_{trap} = \gamma_{trap}^{[N_2]=0} \cdot \frac{1}{1 + 1.0 \times 10^{-23} \text{ m}^3 \cdot [N_2]} \quad (3.4)$$

where $\gamma_{trap}^{[N_2]=0} = 3.3 \times 10^4 \text{ s}^{-1}$ was obtained in an earlier ^{129}Xe SEOP measurement [12]. Unfortunately, the effect of laser power, cell temperature, [Rb], and cell geometry on $\gamma_{trap}^{[N_2]=0}$ are little explored to date. For this work $\gamma_{trap}^{[N_2]=0} = 3.3 \times 10^4 \text{ s}^{-1}$ is assumed to provide a good approximation for ^{129}Xe SEOP at 373 K but $\gamma_{trap}^{[N_2]=0}$ is expected to be significantly higher for ^{83}Kr SEOP at 433 K due to the strongly increased rubidium density. Radiation trapping can be important at low pressure SEOP and is therefore included in Eq. 3.2.

3.3.4 Rubidium depolarization caused by spin-rotation interactions

At lower pressures with correspondingly longer lifetimes of the rubidium-xenon van der Waals complexes, a significant rubidium polarization loss is induced by spin rotation interaction [45]. In Eq. 3.2 this effect is represented by the rate γ_{vdW} . The functional dependence of γ_{vdW} on SEOP gas pressure and composition is difficult to quantify. For an SEOP gas mixture with fixed concentration in the long-lifetime pressure regime (i.e. at very low pressures), the relaxation rate γ_{vdW} will increase with the pressure increase due to the intensified complex formation. At sufficiently high pressure the short molecular lifetime regime is reached and the further increase of complex formation with increasing pressure will be offset by higher breakup rates, thus resulting in pressure independent γ_{vdW} . In this regime, the rubidium nuclear-electron hyperfine interaction limits the influence of spin-rotation relaxation. At further pressure increase however, the very short lifetime regime is reached with a diminished hyperfine

interaction and therefore, γ_{vdW} starts to increase again with increasing pressure until the hyperfine interaction has become completely negligible. For a 1% xenon, 1% nitrogen, and 98% helium SEOP mixture, a rate of $\gamma_{vdW} \approx 2 \times 10^3 \text{ s}^{-1}$ at 423 K (and an approximately 60% higher value at 353 K) has been reported for the short lifetime limit [45]. This value is comparable to that of $\kappa_{sd}^{Xe} [Xe] \approx 2 \times 10^3 \text{ s}^{-1}$ caused by binary collisions in ^{129}Xe SEOP at 40 kPa and 373 K in the 5% xenon - 95% nitrogen mixture. The relaxation rate γ_{vdW} is however mixture dependent. For instance completely replacing helium by nitrogen should considerably reduce γ_{vdW} [46] as nitrogen facilitates the break-up of the rubidium-noble gas van der Waals dimer better than helium. Unfortunately literature data of γ_{vdW} for the mixtures used in this work are not available. SEOP conditions in the current work are likely to create short to very short lived rubidium-noble gas van der Waals complexes. Therefore, to a first approximation and within the scope of this work, γ_{vdW} will be considered as pressure independent because of its general pressure independence in the short lifetime limit and because of its relatively small pressure dependence compared to binary relaxation, $\kappa_{sd}^{NG} [NG]$ in the very short lifetime limit. In the lower pressure regime, where γ_{vdW} actually dominates rubidium depolarization rate this crude approximation is destined to fail, therefore experimental data fitting with Eq. 3.2 (or modifications thereof) was not attempted in this pressure limit.

3.3.5 Spin exchange rate

The spin exchange rate γ_{SE} results from the added contributions of (1) spin exchange in rubidium - noble gas van der Waals complexes that is characterized by the rate constant, γ_{RbNG} and (2) from spin exchange caused by binary collisions quantified by the velocity averaged binary spin-exchange cross section $\langle\sigma v\rangle$. Literature values of γ_{RbNG} and $\langle\sigma v\rangle$ for ^{83}Kr and ^{129}Xe are listed in Table 3.1 [9, 37-39], while Eq. 3.5 shows the contribution of both rates to γ_{SE} [9]:

$$\gamma_{SE} = [Rb] \left(\frac{\gamma_{RbNG}}{[NG]} \left(\frac{1}{1+br} \right) + \langle\sigma v\rangle \right). \quad (3.5)$$

The rates $\gamma_{RbNG} \cdot [Kr]^{-1}$ and $\gamma_{RbNG} \cdot [Xe]^{-1}$ are comparable to their corresponding $\langle\sigma v\rangle$ rates at a densities of 0.25 amagat and 0.4 amagat respectively (in the absence of nitrogen). In this density range, van der Waals dimers (mediated through three-body collisions) and binary collisions contribute about equally to the spin exchange. However, binary collisions will eventually dominate in the spin exchange process as the contributions from van der Waals complexes is expected to decline with the increase of the noble gas concentration and therefore its density [NG].

The nitrogen molecules in the SEOP mixture also contribute to the rubidium-noble gas dimer break up. This contribution is quantified by the characteristic pressure ratio $b = p_0(NG)/p_0(N_2)$ listed in Table 3.1 with the specific values for xenon and krypton [9, 38, 47]. The parameter r in Eq. 3.5 is the partial pressure ratio $p(N_2)/p(NG)$ (or $[N_2]/[NG]$ density

ratio) in a mixture. The ratio b shows that a dilution of xenon in nitrogen can be beneficial to γ_{SE} . However, a dilution of krypton in nitrogen can be detrimental to γ_{SE} because the break up of van der Waals complexes is facilitated by nitrogen more than by krypton. Note however, that nitrogen is still beneficial for ^{83}Kr SEOP because of its radiation quenching effect (section 3.3.3) and because $\kappa_{sd}^{Kr} \approx 100 \cdot \kappa_{sd}^{N_2}$ (section 3.3.1).

3.4 Results and discussion

3.4.1 Noble gas polarization as a function of SEOP gas pressure

Steady state, or near steady state spin polarization was obtained for the ^{129}Xe mixtures after about 6 min of SEOP at 373 K and a near steady state (approximately 80%) was reached after 8 min of SEOP for ^{83}Kr mixtures at 433 K. The steady state polarization P is shown as a function of the total SEOP pressure p_{tot} in Figures 3.2 and 3.3 for hyperpolarized ^{83}Kr and hyperpolarized ^{129}Xe respectively. The noble gas polarization P of both isotopes in all mixtures increased as the total gas pressure was decreased from 350 kPa to below ambient in all studied mixtures. The maximum steady state polarization P^{\max} for hyperpolarized ^{83}Kr was obtained at a total gas pressure p_{tot} , in the range of 35 - 50 kPa, depending on the krypton concentration used. Similarly, a polarization maximum was observed for hyperpolarized ^{129}Xe , however at a lower total pressure range of $p_{tot} = 20 - 30$ kPa. Reducing the pressure below these values resulted to a rapid drop in the steady state polarization of the noble gases. In order to facilitate the following discussions, the SEOP pressure that resulted to the

highest observed steady state polarization P^{\max} , will be labelled as $p^{P^{\max}}$.

Table 3.2 lists P^{\max} for various mixtures, the corresponding total SEOP pressure $p_{tot}^{P^{\max}}$, and the corresponding SEOP partial pressure $p_{NG}^{P^{\max}}$.

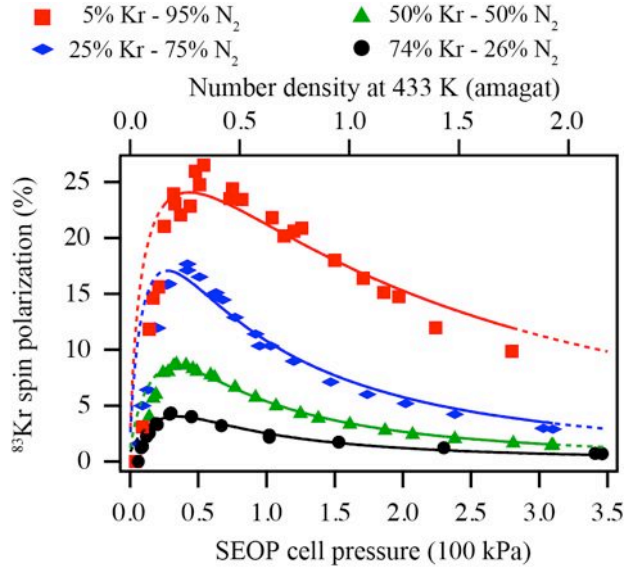


Figure 3.2. ^{83}Kr spin polarization, P , as a function of SEOP pressure. ^{83}Kr spin polarization as a function of SEOP cell pressure and combined number density ($[\text{Kr}] + [\text{N}_2]$) at 433 K for four different gas mixtures. See the legend in the figure for symbol explanation. Polarization data are detailed in Table 3.2. Data analysis using Eq. 3.13 with γ_{op} and $\gamma_{trap}^{[\text{N}_2]=0}$ as fitting parameters is shown in solid lines and resulting values are reported in Table 3.3. Fitting of the data was also not attempted for values much lower than $p_{tot} < p_{tot}^{P^{\max}}$; the dotted lines are extrapolations to pressure ranges outside the fitting region.

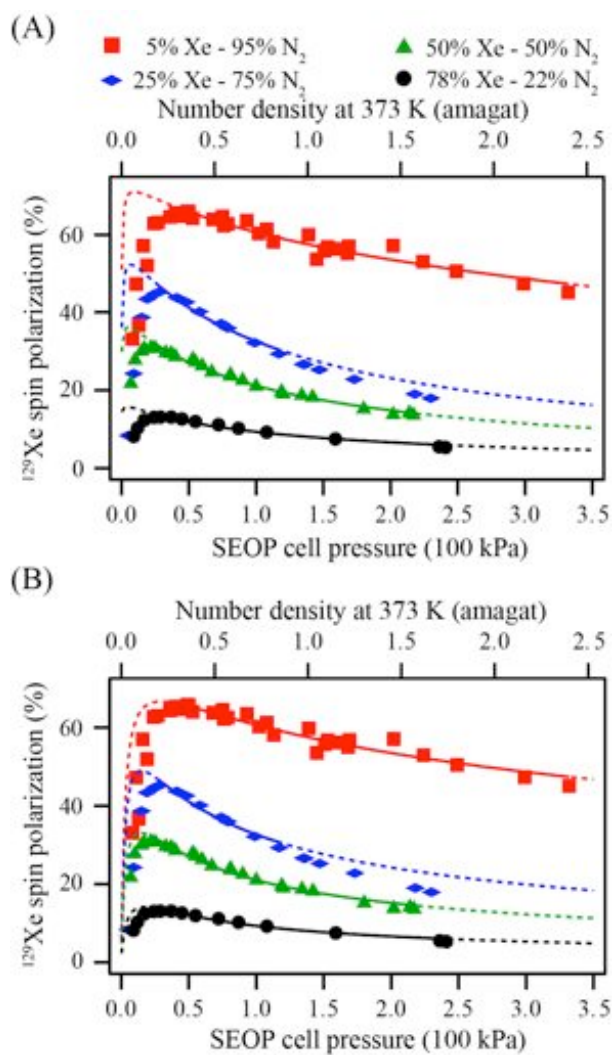


Figure 3.3. ^{129}Xe spin polarization, P , as a function of SEOP pressure. ^{129}Xe spin polarization as a function of the SEOP cell pressure and combined number density ($[\text{Xe}] + [\text{N}_2]$) at 373 K for four different gas mixtures. Please refer to the legend in the figure for symbol explanation. Polarization data are detailed in Table 3.2. **(A)** Solid lines represent data analysis with Eq. 5.13. Extrapolation of these theoretical curves to pressure ranges outside the fitted region are shown by dotted lines. **(B)** Same experimental data as in (A) but the solid lines represent now the data analysis using Eq. 5.13 with the pressure dependence of the rubidium D_1 absorption taken into account through Eq. 5.14. Extrapolation to pressure ranges outside the fitted region are shown by dotted lines. Fitting parameters for (A) and (B) are reported in Table 3.4A and 3.4B, respectively.

Table 3.2. Maximum noble gas polarization P^{\max} , maximum apparent noble gas polarization P_{app}^{\max} , and corresponding gas pressures extracted from data of Figures 3.2 and 3.3.

Mixture composition	Maximum polarization $P^{\max}/\%$	Apparent maximum polarization ^A $P_{app}^{\max}/\%$	SEOP cell pressure and total gas density at maximum polarization $P_{tot}^{P^{\max}}/100$ kPa (density/amagat)	Noble gas partial pressure and noble gas density, [NG], at maximum polarization $P_{NG}^{P^{\max}}/100$ kPa ([NG]/amagat)	SEOP time and temperature
5.0 Kr; 95.0 N ₂	26.5 ± 3.3	1.3 ± 0.2	0.54 (0.34)	0.03 (0.02)	8 minutes 433 K
25.0 Kr; 75.0 N ₂	17.7 ± 2.2	4.4 ± 0.5	0.42 (0.26)	0.11 (0.07)	
49.5 Kr; 50.5 N ₂	8.6 ± 1.1	4.3 ± 0.5	0.41 (0.26)	0.20 (0.13)	
74.1 Kr; 25.9 N ₂	4.3 ± 0.5	3.2 ± 0.4	0.30 (0.19)	0.22 (0.14)	
5.0 Xe; 95.0 N ₂	64.7 ± 8.0	3.2 ± 0.4	0.46 (0.33)	0.02 (0.01)	6 minutes 373 K
24.5 Xe; 75.5 N ₂	45.2 ± 5.6	11.1 ± 1.4	0.28 (0.20)	0.07 (0.05)	
40.3 Xe; 59.7 N ₂	32.6 ± 4.0	13.1 ± 1.6	0.22 (0.16)	0.09 (0.07)	
50.0 Xe; 50.0 N ₂	30.9 ± 3.8	15.5 ± 1.9	0.22 (0.16)	0.11 (0.08)	
78.2 Xe; 21.8 N ₂	13.1 ± 1.6	10.2 ± 1.3	0.37 (0.27)	0.29 (0.21)	

$$^A P_{app}^{\max} = P^{\max} \cdot \frac{P_{NG}}{P_{tot}}$$

Table 3.3. Values for γ_{op} and γ_{trap} from fitting experimental data of ^{83}Kr spin polarization as a function of SEOP cell pressure in Figure 3.2 using Eq. 3.13.^A

Mixture	$\frac{\gamma_{op}}{10^3 \text{ s}^{-1}}$	$\frac{\gamma_{trap}^{[N_2]=0}}{10^3 \text{ s}^{-1}}$
5.0% Kr; 95.0% N ₂	4.3 ± 0.4	125 ± 20
25.0% Kr; 75.0% N ₂	3.1 ± 0.1	100 ± 13
49.5% Kr; 50.5% N ₂	2.37 ± 0.04	164 ± 6
74.1% Kr; 25.9% N ₂	1.49 ± 0.09	139 ± 15

^AA rubidium correction factor of $c^{Rb} = 4$ was used for the fittings of data in Figure 3.2 with Eq. 3.13. The rate constant γ_{vdW} typically resulted to values close to zero but with large error values. Within its error margins γ_{vdW} had little influence on the other fitting parameters and was set to $\gamma_{vdW} = 0$ for the fittings reported in this table.

Table 3.4. Values for γ_{op} , γ_{op}^* , and γ_{vdW} rates obtained from the fitting of experimental data of ^{129}Xe spin polarization as a function of SEOP cell pressure (Figure 3.3) using Eq. 3.13.^A

Mixture	A. Data fitting using Eq. 3.13 (Figure 3.3A)		B. Data fitting using Eqs. 3.13 and 3.14 (Figure 3.3B)	
	$\gamma_{op}/10^3 \text{ s}^{-1}$	$\gamma_{vdW}/10^3 \text{ s}^{-1}$	$\gamma_{op}^*/10^3 \text{ s}^{-1}$	$\gamma_{vdW}/10^3 \text{ s}^{-1}$
5.0% Xe; 95.0% N ₂	44 ± 4	15 ± 2	19.1 ± 1.0	3.2 ± 0.4
24.5% Xe; 75.5% N ₂	27 ± 2	19 ± 3	17.9 ± 1.0	3.9 ± 1.0
50.0% Xe; 50.0% N ₂	34 ± 1	50 ± 3	20.6 ± 0.5	10.6 ± 1.1
78.2% Xe; 21.8% N ₂	25 ± 2	10 ± 20	13.0 ± 0.6	22 ± 3

^AFittings of data in Figure 3.3 using Eq. 3.13 used the following parameters: $f = 1$,

$$\gamma_{trap} = 33000 \text{ s}^{-1}, c^{Rb} = 1.3 \text{ and } \Gamma = 0.0009 \text{ s}^{-1}.$$

As can be seen from Table 3.2, the maximum ^{83}Kr polarization of $P^{\max} = 26.5\%$ was reached for the 5% krypton - 95% nitrogen mixture at an SEOP pressure of 54 kPa. This is a remarkably high spin polarization for a quadrupolar spin system observed at ambient temperature. ^{129}Xe SEOP at a pressure of 46 kPa using a 5% xenon mixture resulted to $P^{\max} \approx 65\%$ spin polarization. Both results were obtained with a 23.3 W laser irradiation that resulted in a power density of 2.6 W/cm^2 at the SEOP cell front window.

Since hyperpolarized noble gasses remain diluted without cryogenic separation process, the obtained polarization does not enable easy comparison with experiments that utilize cryogenic separation. It is therefore useful to define an apparent polarization, P_{app} , scaled to the polarization, P , in the pure hyperpolarized noble gas that would result to the same MRI signal.

$$P_{app} = P \cdot \frac{[NG]}{\sum_i [M_i]} \approx P \cdot \frac{P_{NG}}{P_{tot}} \quad (3.6)$$

The apparent polarization, P_{app} , provides a measure of the ‘usable’ spin polarization in MR experiments if the hyperpolarized noble gas is not separated from the nitrogen after SEOP. Table 3.2 also lists the apparent maximum steady state polarization P_{app}^{\max} . The highest P_{app}^{\max} was obtained for krypton with the 25% and 50% krypton mixtures leading in both cases to $P_{app}^{\max} \approx 4.4\%$. Mixtures with 40% and 50% of xenon lead to the highest values with $P_{app}^{\max} \approx 15.5\%$. In cases where similar P_{app}^{\max} values are obtained

for different SEOP mixtures, economical considerations will prefer the mixture with lower noble gas concentration, in particular when expensive isotopically enriched gases are used.

Note the maximum polarizations listed in Table 3.2 were generated every 6 minutes for hyperpolarized ^{129}Xe and every 8 minutes for hyperpolarized ^{83}Kr (and with slightly increasing values for P_{Kr} at SEOP times up to 18 min). The ideal pumping time for MRI applications however may be shorter than these values if polarization can be compromised in favor for faster experimental repetition.

3.4.2 Spin exchange optical pumping temperature

The three-body spin exchange rate γ_{RbNG} and the binary cross section $\langle\sigma v\rangle$ are both more than two orders of magnitude smaller for the rubidium- ^{83}Kr system than for the rubidium- ^{129}Xe system. The resulting small γ_{SE} rate has two adverse consequences for ^{83}Kr SEOP as predicted by Eq. 3.2. Firstly, a smaller γ_{SE} in the presence of a higher relaxation rate Γ leads to a reduced steady state polarization P for ^{83}Kr compared to that for ^{129}Xe under otherwise identical SEOP conditions. Secondly, smaller γ_{SE} values further result in slower ^{83}Kr SEOP polarization build up as compared to ^{129}Xe SEOP, thus increasing the batch dispense interval in MRI applications. In order to, at least partially, offset this effect $[\text{Rb}]$ needs to be raised through elevated ^{83}Kr SEOP temperatures. In addition to the increased $[\text{Rb}]$, a further advantage of elevated ^{83}Kr SEOP temperatures comes from reduced quadrupolar relaxation of ^{83}Kr on the cell surface (discussed further in *section 3.4.3*). It was found that up to a temperature of

433 K the benefit from the increased spin exchange rate γ_{SE} for ^{83}Kr SEOP outweighs other detrimental effects arising from elevated temperatures. In contrast, a temperature of 373 K was found to produce the highest ^{129}Xe spin polarization in this work. Examples of adverse effects at higher temperatures are increased rubidium-rubidium collision rates, as discussed in *section 3.3.2*, and increased laser absorption in the rising optical density of the rubidium vapor phase.

3.4.3 Results from inversion recovery ^{83}Kr SEOP experiments

The noble gas self-relaxation rate Γ is difficult to obtain from published data as it is specific to some SEOP conditions, for example SEOP cell dimensions and its surface temperature. However, the combined rate constants $B = \gamma_{SE} + \Gamma$ can be extracted from the time dependence of the polarization obtained in SEOP experiments. In principle, build up curves can be measured directly inside the SEOP cell [10, 37, 48]. However, in this work the SEOP time dependence is determined through remotely detected NMR experiments (i.e. after hyperpolarized gas transfer into the high field magnet) as no further experimental modification was required for the existing instrumentation. The drawback of this procedure was that the measurement of the build up curves required time-consuming point-by-point experiments.

The time dependence of the polarization, P_{NG} , was measured in point by point experiments using batch mode SEOP for an incremented time period, t_p , followed by shuttling of the polarized gas mixture into the superconducting magnet for the high field detection. However, the rubidium concentration [Rb] has to be regenerated after each shuttling event and the

time dependence of this regenerative process needs to be eliminated from the data. Since pressure equalization is used for the shuttling of the hyperpolarized gas, a further source of systematic error arises from incomplete gas transfer that leaves hyperpolarized gas in the SEOP cell and thus influences the outcome of the following experiment. The unwanted contributions of these two time dependent processes were previously avoided by maintaining SEOP like conditions for temperature, pressure, and illumination either in the absence of a magnetic field or by switching from circular polarized to linear polarized laser light during a 5 – 10 minutes recovery period. SEOP for the incremented t_p duration is then started by either returning the magnetic field or by reinstating the circular polarization of the irradiation [29]. This type of experiment is reminiscent of ‘*saturation recovery*’ type of NMR relaxation measurements. An increased precision may be obtained in an ‘*inversion recovery*’ type of experiment where either the magnetic field is inverted or the circular polarization is reversed during a constant, precisely timed recovery period. In this work, circular polarized light was switched through rotation of the $\lambda/4$ plate instead of a faster magnetic field switch as SEOP was performed in the fringe field of the superconducting magnet that could not be altered straightforwardly. After returning the original circular polarization for the incremented time t_p , the built up of P_{NG} was fitted to:

$$P_{NG}(t_p) = C + A(1 - 2e^{-Bt_p}) \quad (3.7)$$

with fitting parameter $B = \gamma_{SE} + \Gamma$ as the combined rate constant. The fitting parameters C normalizes the polarization $P_{NG}(t_p = \infty) \equiv 1$. In the

interest of time, the recovery (or ‘inversion’) period was kept to 12 min for ^{83}Kr and 8 min for ^{129}Xe , therefore the fitting parameter A was needed to account for incomplete inversion but also to correct for imperfections in the relative orientation of the $\lambda/4$ plate. Rotation of the $\lambda/4$ plate was accomplished manually, a process that took approximately 4-5 s. The switching time was acceptable for the slow build up rates in the experiments and automation of this process was not pursued. The data from inversion recovery ^{83}Kr SEOP experiments are shown in Figure 3.4A and the rate constants, $B = \gamma_{SE} + \Gamma$, obtained from fitting with Eq. 3.7 are listed in Table 3.3.

The spin exchange rates γ_{SE}^{calc} listed in Table 3.3 were calculated using Eq. 3.5 with the relevant literature values reported in Table 3.1. However, the experimental value $B \approx 3.7 \times 10^{-3} \text{ s}^{-1}$ obtained from the inversion recovery experiments for ^{83}Kr SEOP below 200 kPa presents a problem when combined with the calculated spin exchange rate values γ_{SE}^{calc} in order to determine the first fraction in Eq. 3.2, $\gamma_{SE}/(\gamma_{SE} + \Gamma)$. Using γ_{SE}^{calc}/B , Eq. 3.2 predicts an upper limit for the ^{83}Kr polarization of $P^{\max} \approx 11-14\%$. In reality, any experimentally measured value for P_{Kr} would be further reduced because of $P_{Rb} < 1$ and due to incomplete (approximately 80%) polarization at $t_p = 8$ min in SEOP. In remarkable disagreement, the experimental data show polarization values of up to $P^{\max} = 26.5\%$ and $P^{\max} = 17.7\%$ for the 5% krypton and 25% krypton mixtures, respectively (see Figure 3.2 and Table 3.2).

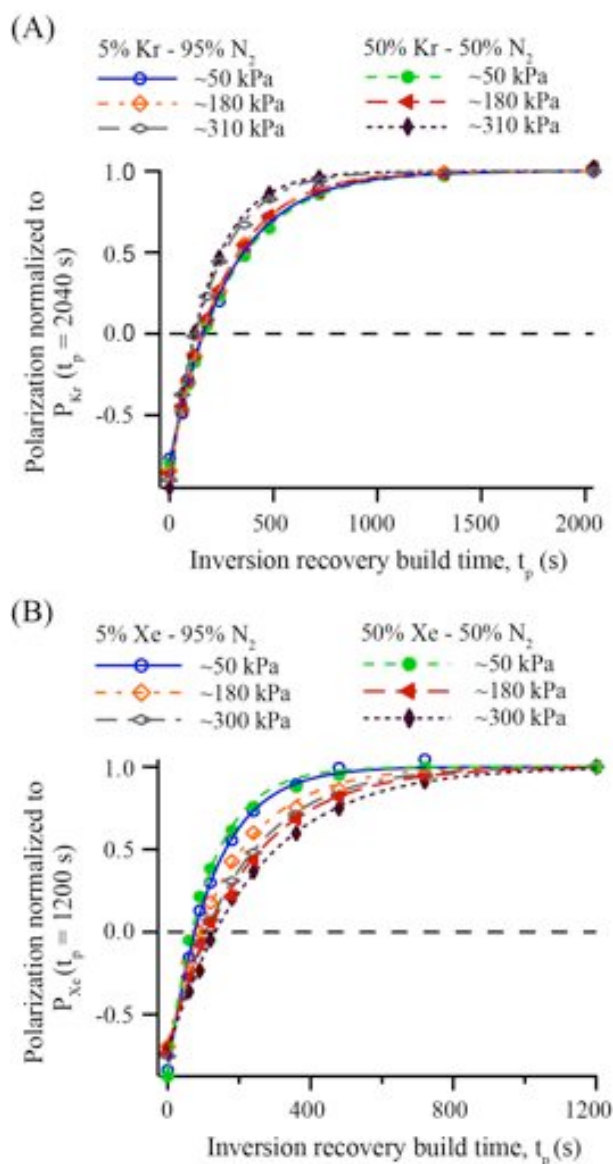


Figure 3.4. Inversion recovery ^{83}Kr and ^{129}Xe SEOP. **(A)** Inversion recovery of ^{83}Kr polarization after SEOP time, t_p , for two krypton-nitrogen gas mixtures at different SEOP pressures. Please refer to the legend in the figure for symbol explanation. **(B)** Inversion recovery of ^{129}Xe polarization after SEOP time, t_p , for two xenon-nitrogen gas mixtures at different SEOP pressures. The inversion recovery data from both (A) and (B) were analyzed using Eq. 3.7. Polarization data were normalized to their values at $t_p = 2040 \text{ s}$ for ^{83}Kr and $t_p = 1200 \text{ s}$ for ^{129}Xe to compare the rate differences of the mixtures and pressures. The obtained rate constants from fitting of both (A) and (B) are reported in Table 3.5.

Table 3.5. ^{83}Kr and ^{129}Xe values for $B = \gamma_{SE} + \Gamma$ obtained from fitting of inversion recovery build up data (see Figure 3.4) with Eq. 3.7.^A

Mixture	SEOP cell pressure (kPa)	B 10^{-3} s^{-1}	γ_{SE}^{calc} 10^{-3} s^{-1}	Γ ^B 10^{-3} s^{-1}
5.0% Kr; 95.0% N ₂	50	3.5 ± 0.1	0.41	1.8 ± 0.1
	180	3.9 ± 0.1	0.36	2.5 ± 0.1
	310	5.0 ± 0.1	0.36	3.6 ± 0.1
50.4% Kr; 49.6% N ₂	50	3.5 ± 0.1	0.43	1.8 ± 0.1
	180	4.0 ± 0.1	0.37	2.5 ± 0.1
	310	5.5 ± 0.1	0.36	4.1 ± 0.1
5.0% Xe; 95.0% N ₂	50	7.8 ± 0.2	7.8	~0
	180	6.0 ± 0.2	3.7	1.2 ± 0.2
	300	5.2 ± 0.1	3.2	1.0 ± 0.1
49.7% Xe; 50.3% N ₂	50	9.4 ± 0.3	5.0	2.9 ± 0.3
	180	4.7 ± 0.2	3.0	0.8 ± 0.2
	300	4.0 ± 0.1	2.7	0.5 ± 0.1

^AThe value of γ_{SE}^{calc} was calculated from Eq. 3.5 using literature values reported in Table 3.1. In the case of multiple literature values, ref. [9] values were used.

^BRubidium correction factors $c^{Rb} = 4$ for ^{83}Kr and $c^{Rb} = 1.3$ for ^{129}Xe were used in the calculation of $\Gamma = B - c^{Rb} \cdot \gamma_{SE}^{calc}$.

The discrepancy between predicted maximum possible polarization and observed polarization may be due to incorrect literature data in Table 3.1 used for determining γ_{SE}^{calc} . Note that the literature data was obtained at temperature conditions different from the ones used in this work. Another potential culprit is a wrong value of [Rb] obtained from Eq. 3.3 based on temperature measurements outside the cell. The temperature inside the cell under high power laser irradiation in the presence of the liquid rubidium metal is unknown. Wagshul and Chupp [35] noted a discrepancy of a factor of two or more in [Rb] under ^{129}Xe SEOP conditions from the prediction by the equilibrium vapor equation. Further doubt about [Rb] determination through external temperature measurements arises from Raman spectroscopical experiments by Happer and co-workers that provide access to the *in situ* temperature distribution within the SEOP cell by measuring the

rotational - vibrational nitrogen temperature [49]. The internal temperatures were found to substantially exceed those measured externally at the cell outside surface. Finally, a numerical simulation study [36] also draws a very complex picture about a non-uniform temperature distribution within a static SEOP cell with significantly elevated internal temperatures. The same, perhaps amplified problem may occur for ^{83}Kr SEOP experiments that are run at the cell outside temperature of 433 K. A correction factor c^{Rb} for the rubidium concentration from Eq. 3.3 is therefore introduced for this work. It follows from the discrepancy between observed and calculated P^{max} described above, that $c^{\text{Rb}} > 2$. An upper limit for the correction factor $c^{\text{Rb}} < 8$ is obtained from the fact that Γ can not be negative. Further, the upper limit can be reduced to $c^{\text{Rb}} < 6$ if one assumes that relaxation rate Γ of ^{83}Kr is not significantly lower than typical rates found for ^{129}Xe under SEOP conditions. Further determination of c^{Rb} for ^{83}Kr SEOP was not possible from the data in this work, however the qualitative outcome of the fittings in Figure 3.2 is not strongly affected within the range $2 < c^{\text{Rb}} < 6$. The correction factor was set to $c^{\text{Rb}} = 4$ for further data analysis in Figure 3.2.

The similarity in the $\gamma_{SE}^{\text{calc}}$ values in Table 3.3 for ^{83}Kr SEOP is caused by the $[\text{Kr}]$ independent rate constant $\langle \sigma v \rangle$ that dominates over the $\gamma_{\text{RbNG}} \cdot [\text{Kr}]^{-1}$ term even at the low pressures of $p_{\text{tot}}^{\text{Pmax}}$ for all krypton mixtures. As pressure $p_{\text{tot}} > p_{\text{tot}}^{\text{Pmax}}$, the van der Waals contributions will be even further marginalized. As a consequence, the inversion recovery ^{83}Kr SEOP curves in Figure 3.4A all display similar time dependence at SEOP

pressures below 200 kPa. At 310 kPa, the combined rate constant is increased due to the increased relaxation rate constant Γ .

In the case of ^{83}Kr the factors affecting the Γ rates are worth further discussion since the surprisingly slow relaxation of this nuclear electric quadrupole isotope is of crucial importance. Due to the nuclear electric quadrupole moment Γ should possess a pressure dependence that needs to be accounted for in the data analysis and fitting of the build up curve with Eq. 3.7. Figure 3.5 shows the pressure dependence of the ^{83}Kr relaxation rate constant, Γ , listed in Table 3.3 and displays the gas composition independence of Γ . Note that the corresponding longitudinal relaxation times range between $T_1 = 244 - 555$ s in this work.

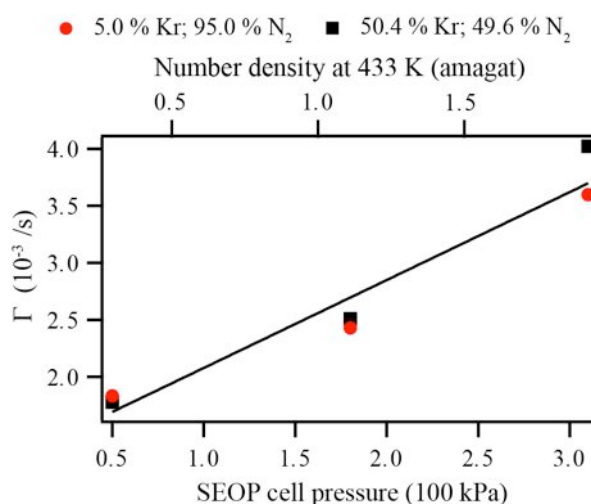


Figure 3.5. ^{83}Kr relaxation rate under SEOP conditions. Dependence of Γ on SEOP cell pressure for two different krypton mixtures as described in the legend. Γ was calculated from the expression $\Gamma = B - c^{Rb} \cdot \gamma_{SE}^{calc}$; where B was determined experimentally fitting Eq. 3.7 with the inversion recovery data of ^{83}Kr in Figure 3.4A. The value for γ_{SE} was calculated from Eq. 3.5 using literature values displayed in Table 3.1, including the rubidium correction factor $c^{Rb} = 4$. The combined data from both mixtures was fitted assuming linear pressure dependence of Γ (solid line) with the result summarized in Eq. 3.10.

Three events may contribute to the quadrupolar driven relaxation rate constant Γ ; (i) binary collisions, (ii) krypton- krypton van der Waals formation, and (iii) surface adsorption:

$$\Gamma = \frac{1}{T_1^{binary}} + \frac{1}{T_1^{vdW}} + \frac{1}{T_1^{surface}} \quad (3.8)$$

(i) The rate constant for relaxation caused by binary krypton-krypton or krypton-nitrogen gas phase collisions is [50]:

$$\frac{1}{T_1^{binary}} = \left[\left(\frac{1}{T_1 \rho_{Kr}} \right)_{Kr} + \left(\frac{1}{T_1 \rho_{N_2}} \right)_{N_2} \cdot r \right] \rho_{Kr} \quad (3.9)$$

with ρ_{Kr} and ρ_{N_2} as the density of the respective gases in amagat and $r = \rho_{Kr}/\rho_{N_2}$. The density independent constants at ambient temperature are

$$\left(1/T_1 \rho_{Kr} \right)_{Kr}^{298K} \approx 1.6 \times 10^{-3} \text{ amagat}^{-1} \text{ s}^{-1} \text{ and } \left(1/T_1 \rho_{N_2} \right)_{N_2}^{298K} \approx 2.3 \times 10^{-3} \text{ amagat}^{-1} \text{ s}^{-1}$$

[50]. Although the corresponding values for 433 K are not known, a linear dependence of $1/T_1^{binary}$ on gas pressure (and therefore on ρ_{Kr}) can be assumed. Due to the similarity of the two rate constants, the resulting rate $1/T_1^{binary}$ is unlikely to be strongly affected by the gas composition. The limited amount of data shown Figure 3.5 does not indicate a significant composition dependence of Γ . Linear fitting of the data leads to:

$$\Gamma^{433K}(\rho_{tot}) = 1.3 \times 10^{-3} \text{ s}^{-1} + 1.2 \cdot 10^{-3} \text{ amagat}^{-1} \text{ s}^{-1} \cdot \rho_{tot}, \quad (3.10)$$

where the total gas density $\rho_{tot} = \rho_{Kr} + \rho_{N_2}$ was used making the simplifying assumption of an equal contribution from the two gases to the

binary collision induced relaxation. The contribution $(1/T_1 \rho_{tot})_{Kr, N_2}^{433K} \approx 1.2 \times 10^{-3} \text{ amagat}^{-1} \text{ s}^{-1}$ in Eq. 3.10 is in reasonable agreement with the literature data [50]. However, the interpolated zero pressure value $\Gamma(\rho_{tot} \rightarrow 0) = 1.3 \cdot 10^{-3} \text{ s}^{-1}$ cannot arise from binary gas phase collision. Two further relaxation mechanisms, described below, may contribute to this rate. Rewriting Eq. 3.10 as a function of the krypton number density and using $r = [N_2]/[Kr]$ leads to:

$$\Gamma([Kr]) = 1.3 \times 10^{-3} \text{ s}^{-1} + 4.6 \times 10^{-29} \text{ s}^{-1} [Kr] \left(1 + \frac{1}{r} \right). \quad (3.11)$$

(ii) The rate constant for relaxation caused by ^{83}Kr - krypton van der Waals dimers in the gas phase becomes independent of the gas density if the extreme narrowing condition is fulfilled [51]. This is the case for all experiments reported in this work. Further [31]:

$$\frac{1}{T_1^{vdW}} \propto \frac{K}{(k_{Kr} + rk_{N_2})} \quad (3.12)$$

where K is the equilibrium constant of the ^{83}Kr - krypton complex formation and k_{Kr} and k_{N_2} are the breakup rate constants due to collisions with krypton atoms and nitrogen molecules respectively. Eq. 3.12 and previous measurements at ambient temperature predict a decreasing relaxation rate $1/T_1^{vdW}$ with increasing nitrogen concentration [31]. Figure 3.5 does not reflect such behavior and suggest therefore that $1/T_1^{vdW}$ does not contribute significantly under SEOP conditions at 433 K. A more thorough experimental study would be required to prove this since the small amount

of data in Figure 3.5 does not allow for a thorough analysis. However, a marginal contribution from van der Waals complexes to the overall relaxation is not completely unexpected due to the temperature dependence of the equilibrium constant K of dimer formation. At high temperature, the equilibrium will be shifted strongly towards the dissociated atoms. Therefore, van der Waals complexes are not the likely cause for the interpolated zero density Γ rate in Eq. 3.10.

(iii) Another possible contribution to Γ is caused by relaxation processes on the surface of the SEOP cell. The corresponding rate, $1/T_1^{surface}$, is independent of the gas composition (assuming no dramatic surface adsorption enthalpies differences between the gas components) and independent of gas pressure (assuming low surface coverage in the Henry isotherm limit). However, $1/T_1^{surface}$ has been demonstrated to depend on the surface to volume ratio [52] and is strongly accelerated by the treatment of model surfaces with silanizing agents [29, 52-54]. In order to keep Γ small, the SEOP cells used in this work have not been treated with silanizing or siliconizing agents. Increasing the temperature clearly helps with reducing the longitudinal ^{83}Kr relaxation. Previously, a temperature dependent decrease of ^{83}Kr longitudinal relaxation rates from $1/T_1 = 1.2 \times 10^{-2} \text{ s}^{-1}$ at 297 K to $1/T_1 = 4.5 \times 10^{-3} \text{ s}^{-1}$ at 433 K was demonstrated for a SEOP cell shaped container, similar to the one used in this work, but without laser irradiation and alkali metal present [28]. The 433 K value was obtained with a gas mixture of 95% krypton and 5% nitrogen at a density of approximately 1 amagat. Using $1.2 \times 10^{-3} \text{ amagat}^{-1} \text{ s}^{-1} \cdot \rho_{tot}$ from Eq. 3.10, one finds a zero

pressure intercept value of $\Gamma(\rho_{tot} \rightarrow 0) = 1/T_1^{surface} = 3.3 \times 10^{-3} \text{ s}^{-1}$ and therefore a 2.5 fold faster surface relaxation than the one found in this work under SEOP conditions (i.e. laser irradiation and in the presence of rubidium metal). The reduced relaxation under SEOP conditions may be caused by a cell temperature that is significantly higher internally than the externally measured value. Alternatively, the presence of rubidium itself may reduce $1/T_1^{surface}$ through competitive co-adsorption [13]. In any case, $1/T_1^{surface}$ can be further reduced through the use of larger SEOP cells with decreased surface to volume ratios, thus leading to improved polarization values for ^{83}Kr SEOP.

3.4.4 ^{83}Kr polarization as a function of SEOP pressure

The pressure dependence of the ^{83}Kr polarization, shown in Figure 3.2, should be described in principle by Eq. 3.2 for SEOP pressures above p_{tot}^{Pmax} . Most of the relevant parameters are listed either in Table 3.1 or described by Eqs. 3.3, 3.4, 3.5, and 3.11. The equation used for fitting of the data in Figure 3.2 is:

$$P = f \cdot \frac{c^{Rb} \cdot \gamma_{SE}^{calc}}{c^{Rb} \cdot \gamma_{SE}^{calc} + \Gamma(p)} \cdot \frac{\gamma_{op}}{\gamma_{op} + \gamma_{trap} + \gamma_{vdW} + \sum_{i \neq Rb} \kappa_{sd}^i [M_i] + \kappa_{sd}^{Rb} \cdot c^{Rb} [Rb]} \quad (3.13)$$

where γ_{op} and $\gamma_{trap}^{[N_2]=0}$ (in Eq. 3.4) were used as fitting parameters. The correction factor $c^{Rb} = 4$ was used for [Rb], as described in *section 3.4.3*. A functional form of $\Gamma(p)$ is given by Eq. 3.11 (also based on $c^{Rb} = 4$). The scaling factor $f = 0.8$ in Eq. 3.13 accounts for the limited SEOP duration of

8 min that caused the polarization build up to be approximately 80% completed. The rubidium electron spin relaxation due to spin-rotation interaction in van der Waals complexes is represented by the rate γ_{vdW} that is assumed to be constant under the SEOP conditions used in this work (see *section 3.3.4*). When used as a third fitting parameter, γ_{vdW} consistently emerged with negative or near zero values with little influence on the other fitting parameters, indicating small to negligible spin-rotation interactions for ^{83}Kr . It was therefore set to zero and the results for γ_{op} and $\gamma_{trap}^{[N_2]=0}$ are listed in Table 3.5.

At a first glance, the fitting result in Figure 3.2 (solid lines) appear to demonstrate that Eq. 3.13 qualitatively describes the dependence of the ^{83}Kr SEOP polarization on $[\text{Kr}]$ at pressures above $p_{tot}^{P_{max}}$. The obtained function describes the experimental observation reasonably well beyond the fitting range (see dashed line). The resulting $\gamma_{trap}^{[N_2]=0}$ rate constants are fairly consistent but are about three fold increased compared to previously reported ^{129}Xe SEOP data [12]. These values are quite high but an increase in $\gamma_{trap}^{[N_2]=0}$ with increasing rubidium density is expected. The γ_{op} rates listed in Table 3.5 are low and indicate low pumping rates as it would be expected for an optically thick medium with high $[\text{Rb}]$. The 2.8 fold decrease of γ_{op} with increasing krypton concentration is further discussed in *section 3.4.8*.

3.4.5 Result from inversion recovery ^{129}Xe SEOP experiments

In contrast to ^{83}Kr SEOP, the time behavior of the ^{129}Xe SEOP polarization shown in Figure 3.4B depends strongly on total pressure and

gas composition (see Table 3.3). This observation is in agreement with previous work [10] and was expected since γ_{RbNG} , i.e. the van der Waals contribution to the spin exchange rate caused by three-body collisions, plays a more dominant role for ^{129}Xe SEOP than for ^{83}Kr SEOP. An increased γ_{RbNG} relative to the rate $\langle\sigma v\rangle$ caused by two body collisions will result in a stronger noble gas density dependency for γ_{SE} in Eq. 3.5. Furthermore, the time scale of the inversion recovery is accelerated at low xenon density compared to that of ^{83}Kr (Figure 3.4A). However, at high $[\text{Xe}]$, γ_{SE} is reduced and the ^{129}Xe SEOP time dependence (i.e. the rate constant $B = \gamma_{SE} + \Gamma$) becomes similar to that of ^{83}Kr SEOP at high $[\text{Kr}]$. The reason for the similar B values at high noble gas densities are of course different for the two isotopes: The dominating term in ^{129}Xe SEOP is γ_{SE} that decreases with $[\text{Xe}]$, whereas Γ is assumed to be pressure independent. The ^{83}Kr SEOP time dependence, on the other hand is controlled through Γ that increases with $[\text{Kr}]$ while γ_{SE} rate of ^{83}Kr is mostly pressure independent.

The combined rate constants $B = \gamma_{SE} + \Gamma$ and the rates γ_{SE}^{calc} for ^{129}Xe , as listed in Table 3.3, imply that the correction factor for $[\text{Rb}]$, if needed at all, must be $c^{Rb} < 1.6$ because of the requirement $\Gamma \geq 0$. Once again, c^{Rb} cannot be further determined and the average $c^{Rb} = 1.3$ of the range is taken. Furthermore, the assumption is made that Γ is caused mainly by interactions with the surface and is therefore pressure and gas composition independent. This seems to be indeed the case with the

exception of the data taken at 50 kPa that scatter widely. However, for ^{129}Xe SEOP at this pressure the values for Γ are relatively small compared to B and a significant error is not unlikely. Excluding 50 kPa data and averaging the 180 kPa and 300 kPa data one obtains $\Gamma = 9 \times 10^{-4} \text{ s}^{-1}$ using $c^{Rb} = 1.3$. Note, for $c^{Rb} = 1$ it follows that $\Gamma = 1.9 \times 10^{-3} \text{ s}^{-1}$ in better agreement with data by Goodson et al. [10] who previously determined $\Gamma = 1.7 \times 10^{-3} \text{ s}^{-1}$ in a coated SEOP cell. However, as will be discussed in the following section, the exact value is not very important for the description of ^{129}Xe SEOP in this work.

3.4.6 ^{129}Xe polarization as a function of SEOP pressure

A qualitative analysis of the data shown in Figure 3.3A was attempted with Eq. 3.13 derived from Eq. 3.2 with the inclusion of the correction factor for the rubidium density, c^{Rb} . During the fitting procedure the rates γ_{op} and γ_{vdW} were used as the fitting parameter with the correction factor set to $c^{Rb} = 1.3$ and the nuclear relaxation term to $\Gamma = 9 \times 10^{-4} \text{ s}^{-1}$. Unlike for ^{83}Kr SEOP that is run at a temperature of 433 K, the radiation trapping term for ^{129}Xe SEOP could be taken from literature data with $\gamma_{trap} = 33000 \text{ s}^{-1}$ [12]. Furthermore, the SEOP duration was long enough to reach the steady state polarization value and therefore one could set $f = 1$. The rest of the constants used in the fitting procedure were taken from Table 3.1, in the case of the multiple choices of the literature data the constants from reference [9] were used. The resulting fits over the pressure range from 45 to 240 kPa are displayed (solid lines) in Figure 3.3A (see also Table 3.5A for the relevant fitting parameters). The theoretical curves were further

extended over the entire pressure range using the values for γ_{op} and γ_{vdW} obtained from fitting (dotted lines). Although, fitting curves using Eq. 3.13 seem to qualitatively describe the experimental behavior in Figure 3.3A, the results listed in Table 3.5A are not within the expected range. The optical pumping rate constants are quite high and, the rate constant γ_{vdW} values are about one order of magnitude higher than a previous literature value for a 1% xenon, 1% nitrogen, and 98% helium SEOP mixture with $\gamma_{vdW} \approx 3.2 \times 10^3 \text{ s}^{-1}$ at 353 K [45] (see *section 3.3.4*). Furthermore, increasing [Xe] and decreasing [N₂] should lead to increasing γ_{vdW} , however the value for the mixture 78.2% xenon drops below γ_{vdW} for all other mixtures and exhibits an unacceptably high error.

Note that the general appearance of the overall shape of the fitting curves is not dramatically affected by c^{Rb} (at least within the range $1 \leq c^{Rb} < 1.6$), nor do the resulting values for the fitting parameters change significantly. Generally, the larger γ_{SE}/Γ ratio makes the first term in Eq. 3.13 less important for ¹²⁹Xe SEOP compared to ⁸³Kr SEOP. However, the unsatisfactory results of the data fitting with Eq. 3.13 will need some further considerations. The rubidium D₁ absorption linewidth may hold important information for the second term in Eq. 3.13 and may provide a better understanding of the experimental data. The effect of the D₁ linewidth is discussed in the following section.

3.4.7 Non-linear pressure broadening of the rubidium D₁ absorption linewidth

Figure 3.6A shows infrared absorption spectra of rubidium within the SEOP cell when illuminated by an incandescent light source. Spectra were acquired at 433 K with pure krypton for three pressures: 9 kPa, 68 kPa and 434 kPa. Only the D₁ transition (i.e. the $^1S_{1/2} \rightarrow ^1P_{1/2}$ transition at 794.7 nm) and its linewidth are relevant for the SEOP studied in the present work. The pressure behavior of the D₁ linewidth is depicted in Figure 3.6B. Further theoretical analysis suggests that a $[\text{Xe}]^{1/3}$, $[\text{Kr}]^{1/3}$, and $[\text{N}_2]^{1/3}$ functional form provides a reasonably good description of the absorption linewidth behavior over the studied pressure range. The non-linear rubidium D₁ line dependence on gas density dependence is in contrast to the linear gas density dependence usually found for alkali metal D₁ or D₂ transitions (see for instance [30, 55]). The cause for this unexpected behavior was not further investigated and the exact functional description would benefit from refinement in future research.

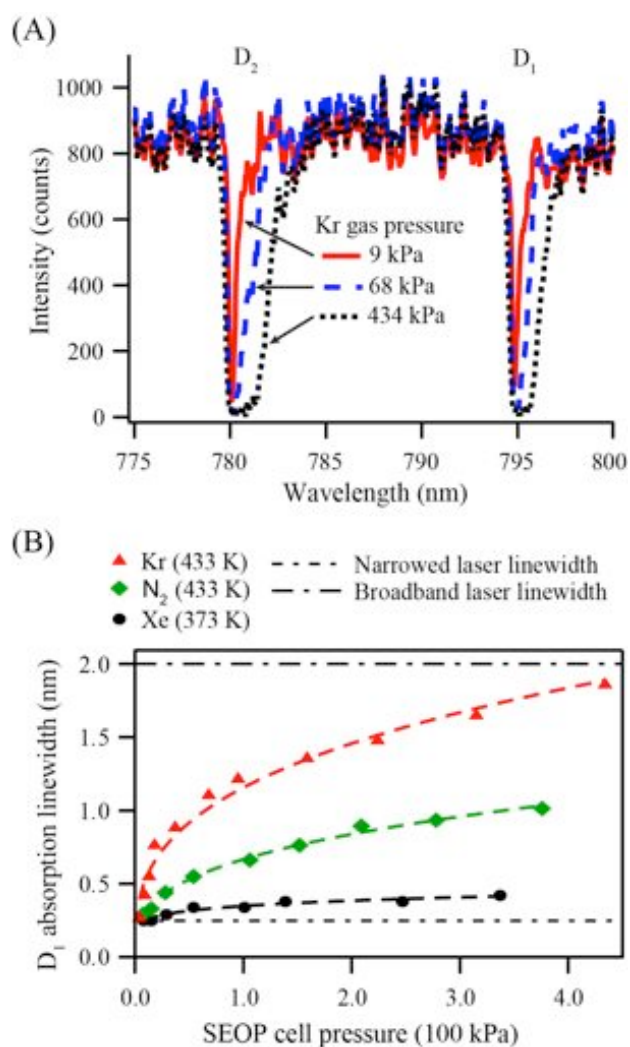


Figure 3.6. Rubidium infrared absorption linewidth as a function of gas pressure. **(A)** Infrared absorption spectrum of rubidium in the SEOP cell containing pure krypton gas at 433 K at three different pressures as detailed in the figure legend. The absorption lines experience a pressure broadening and, to a lesser extent, a shift to higher wavelengths with increasing pressure. **(B)** Rubidium D_1 absorption linewidth as a function of SEOP cell pressure at 433 K for pure krypton (solid red triangles), for pure nitrogen at 433 K (solid green squares), for pure xenon at 373 K (solid black circles). The pressure dependence of the absorption linewidth can be approximately described by $\nu_{1/2} \propto p^{1/3}$ (dashed lines). Eq. 3.14 was concluded from the observed linewidth dependence. The linewidth of the narrowed laser and the broadband laser are 0.25 nm and 2.0 nm respectively, and are indicated in the figure by horizontal dotted lines.

Figure 3.6B shows that the linewidth in the presence of either krypton or nitrogen at 433 K is much broader than that in the presence of xenon at 373 K. The rubidium absorption linewidth with nitrogen at 373 K was too close the resolution limit of the optical spectrometer used (i.e. 0.04 nm). The data demonstrates that all krypton-nitrogen mixtures at 433 K should lead to a D_1 broadening that is much larger than the laser linewidth (0.25 nm – dashed line in Figure 3.6B) at all pressures above p_{tot}^{max} .

However, a different situation occurs for xenon at 373 K, in particular in mixtures with nitrogen. In these cases the laser linewidth may exceed the D_1 linewidth and thus not all of the laser power will be absorbed. The effect of the linewidth is difficult to quantify, in particular since exact on-resonance irradiation can be disadvantageous as explored in detail by Wagshul and Chupp [35] and recently observed for high power irradiation by Wild and co-workers [56] and by Goodson and co-workers [57]. However, for this work the simple assumption is made that laser irradiation with a wider linewidth than the D_1 linewidth will lead to a pressure dependent pumping rate that follows the same dependence as the D_1 linewidth itself:

$$\gamma_{op}(\rho) \approx \gamma_{op}^* \cdot \left(\frac{[Xe]}{2.6868 \times 10^{25} \text{ m}^{-3}} \right)^{1/3} \quad (3.14)$$

with γ_{op}^* as the optical pumping rate at 1 amagat total gas density. The density dependent rate constant $\gamma_{op}(\rho)$ as defined in Eq. 3.14 replaces γ_{op} in Eq. 3.13. Using γ_{op}^* and γ_{vdW} as fitting parameters with all other parameters kept identical to the ones used in *section 3.4.6*, fitting with Eq.

3.13 leads to the solid lines depicted in Figure 3.3B with the values for rate constants listed in Table 3.5B. Once again, the theoretical curves were further extended over the entire pressure range using the values for γ_{op}^* and γ_{vdW} obtained from fitting (dotted lines). The results for γ_{op}^* listed in Table 3.5B are similar to previous literature values [12] obtained under similar conditions and seem to be constant for different gas compositions except for the highest xenon concentration where a clear drop in γ_{op}^* results. The value for $\gamma_{vdW} = 3.2 \times 10^{-3} \text{ s}^{-1}$ at 373 K for the mixture with 5% in Table 3.5 is identical to the literature value $\gamma_{vdW} = 3.2 \times 10^3 \text{ s}^{-1}$ for a 1% xenon, 1% nitrogen, and 98% He SEOP mixture at 353 K [45]. Further, with increasing [Xe] the values for γ_{vdW} show a monotone increase. Overall, the consideration of the pressure dependence of the rubidium D₁ (Eq. 3.14) in Eq. 3.13 appears to result to more realistic values for γ_{op}^* and γ_{vdW} . While there is little effect on the qualitative appearance between the fitted curves in Figures 3.3A and 3.3B, the extended curve (dotted line) in Figure 3.3B provides a better description of the observed data compared to the one in Figure 3.3A.

It should be noted again that Eq. 3.14 should be handled with care since it is based on a number of simplifying assumptions. Firstly, neither the line shape of the pressure broadened rubidium D₁ transition nor the emission line shape of the frequency narrowed diode-array laser are Lorentzian or otherwise straightforwardly defined. Further, at high xenon concentration and pressure, the adsorption linewidth starts to exceed the

laser linewidth causing the validity of the underlying concept in Eq. 3.14 to end. This may be the case in particular at high SEOP pressures for the mixture containing 78.2% xenon. Another factor, not considered here, is the pressure dependent shift of the D₁ transition. For ¹²⁹Xe SEOP at 373 K this shift is small with 0.13 nm over the used pressure range for pure xenon. Although the shift is larger at 433 K with 0.43 nm over the used pressure range for krypton (see Fig 5A) it is still small compared to the D₁ line broadening. Despite the limitation of Eq. 3.14, requiring more refinement in future research, the current work suggests that the effect of pressure broadening needs to be considered for a correct description of variable pressure ¹²⁹Xe SEOP with narrowed lasers.

3.4.8 Non-linear pressure broadening of the rubidium D₁ absorption linewidth

The γ_{op} values for ⁸³Kr SEOP listed in Table 3.5 change by a factor of approximately 2.8 between the gas mixtures used. The γ_{op}^* rates found in ¹²⁹Xe SEOP summarized in Table 3.5B are less affected by [Xe] except for the mixture containing 78.2% xenon where the rate drops significantly. However, nothing in the general theory outlined in *section 3.3* gives rise to the expectation that γ_{op} is affected by the noble gas-nitrogen ratio of the various mixtures. Nevertheless, at the same time it has been noted that the temperature gradient between the front and the back of the SEOP cell changed when SEOP mixture was altered.

The mixture dependent changes in the temperature gradient across the SEOP cell may have been induced by the different thermal conductivity of the used gas mixtures. Under the experimental SEOP conditions, nitrogen

has an approximate 2.5 times larger thermal conductivity than krypton (and 4.5 times larger than xenon) [58]. Therefore, as the krypton or xenon concentration in the SEOP cell is increased, the decreasing thermal conductivity allows for higher temperature difference between the laser-illuminated front of the SEOP cell and its back. The consequences of this temperature gradient are unknown but changes in local rubidium concentration, thermal convection, and laser penetration are likely to lead to different convection patterns within the cell [36, 59]. Note also, that the heat capacity, C_V , of nitrogen is more than 5/3 larger than that of a mono-atomic noble gas. Therefore, the corresponding changes between the gas mixtures may potentially have a profound impact on quantitative SEOP measurements and comparison of data between different noble gas mixtures needs to be handled with great caution. Due to the higher temperature, ^{83}Kr SEOP may be stronger affected than ^{129}Xe SEOP.

Thermal conductivity and heat capacity effects may explain the mixture dependent γ_{op} values but would of course also require mixture dependent c^{Rb} values. Unfortunately, the limited data in this work does not make the use a further fitting parameter reasonable in particular since the differences between the γ_{op} values are not too excessive.

However, a serious concern for the fitting of the experimental data would be SEOP gas pressure on the temperature, γ_{op} , and c^{Rb} . Fortunately, no effect on the pump cell temperature gradient with pressure changes has been noted. Moreover, the well-known equation for the thermal conductance, κ , of an ideal gas is

$$\kappa = \frac{1}{3} \bar{c} \lambda \cdot C_{V,m} \cdot [M] \cdot N_A^{-1} \quad (3.15)$$

where \bar{c} is the mean average velocity of the gas molecules, λ is the mean free path, $C_{V,m}$ is the molar heat capacity at constant volume, $[M]$ the density of the gas, and N_A is Avogadro's number. The thermal conductivity of an ideal gas is pressure independent because the gas density is directly proportional to the pressure, whereas $\lambda \propto p^{-1}$ and \bar{c} is also pressure independent.

3.4.9 Effect of laser power and laser linewidth

The effects of laser power on the polarization curves are shown in Figure 3.7. The power of the laser irradiation was adjusted in the linear polarized part of the laser beam rotating the $\lambda/2$ plate positioned in front of a beam splitter (see *section 3.2.2* or Figure 3.1B). This procedure allowed for the control of the laser irradiation power (incident at the SEOP cell) without changing the linewidth, the line shape, and irradiation pattern (i.e. beam shape). Fitting of the data was performed using Eq. 3.13 in the same fashion as in *section 3.4.7* using $\gamma_{op}(\rho)$ as defined in Eq. 3.14. The parameter $\gamma_{trap}^{[N_2]=0} = 33000 \text{ s}^{-1}$ at 23.3 W power was taken from literature [12] and was scaled linearly with the relative decrease of laser power.

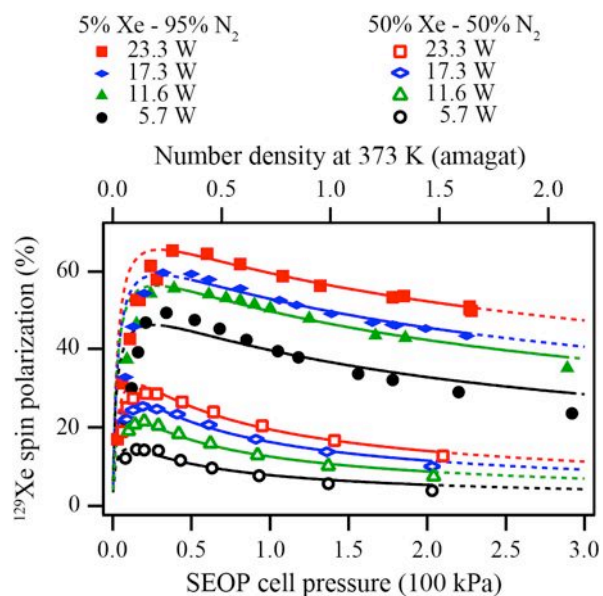


Figure 3.7. ^{129}Xe polarization, P , dependence on laser power. ^{129}Xe spin polarization as a function of SEOP cell pressure for two different gas mixtures at four different SEOP laser power levels. Please refer to the figure legend for symbol explanation. The laser power was measured in the front of the SEOP cell. Data were analyzed using Eq. 3.13 (utilizing Eq. 3.14) within the fitting region (solid lines). Extrapolations to pressure ranges outside the fitted region are shown by dotted lines. The fitting procedure is discussed in *section 3.4.9* and the results of the data analysis are listed in Table 3.6.

Table 3.6. Values of γ_{op}^* rates from fitting of the ^{129}Xe spin polarization data for different laser powers and laser linewidths in Figures 3.7 and 3.8 using Eq. 3.13.^A

Laser source	Mixture	Power (W)	$\gamma_{op}^*/10^3 \text{ s}^{-1}$
Narrowed laser (0.25 nm linewidth)	5.0% Xe; 95.0% N ₂	23.3	17.7 ± 0.2
		17.3	12.8 ± 0.2
		11.6	11.0 ± 0.2
		5.7	6.9 ± 0.3
	50.0% Xe; 50.0% N ₂	23.3	18.6 ± 0.3
		17.3	14.8 ± 0.3
		11.6	10.8 ± 0.3
		5.7	6.3 ± 0.3
Broadband laser (2 nm linewidth)	5.0% Xe; 95.0% N ₂	15.6	2.0 ± 0.1
	50.3% Xe; 49.7% N ₂	15.6	1.6 ± 0.1

^AThe rubidium correction factor was set to $c^{Rb} = 1.3$. The values of $\gamma_{vdW} = 3200 \text{ s}^{-1}$ from Figure 3.3B (Table 3.5B) for the 5% xenon mixture and $\gamma_{vdW} = 10600 \text{ s}^{-1}$ for the ~50% xenon mixture were used. The parameter $\gamma_{trap}^{[N_2]=0} = 33000 \text{ s}^{-1}$ at 23 W power was taken from literature [12] and scaled linearly for all other powers with the relative decrease of laser power.

Measurements at 23.3 W power were performed redundantly under the same pumping conditions as the ones used for 5% and 50% xenon mixtures displayed Figure 3.3. The resulting rates, γ_{op}^* , are listed in Table 3.6 for the two mixtures at various laser power levels.

The increase in γ_{op}^* as the laser power is raised from 5.7 W to 23.3 W is 3.0 fold for the 50% mixture and is 2.6 fold for the 5% xenon mixture. However, the dependence of P_{Xe}^{max} on laser power (see Figure 3.7) is more pronounced for the 50% mixture (approximately 2.0 fold increase in the polarization P_{Xe}^{max} between 5.7 W to 23.3 W) compared to the 5% xenon gas mixture (1.3 fold increase). The increasing importance of laser power for SEOP with higher noble gas concentration is due to the second fraction in Eq. 3.13 that makes the γ_{op}^* (or γ_{op}) values more relevant for the obtained polarization, P_{Xe}^{max} , if the destructive rates $\kappa_{sd}^{NG}[NG]$ are high. Therefore

higher laser power is particularly beneficial for higher noble gas concentration SEOP. This is an important observation for the concept of cryogen-free SEOP.

Figure 3.8 depicts a comparison of SEOP results obtained with a line narrowed (0.25 nm) Comet laser module using reduced laser power (17.3 W) and with a similar power (15.6 W) but using much larger linewidth (Coherent FAP, approximately 2 nm line width). Data were analyzed with Eq. 3.13 in identical fashion as above and the resulting γ_{op}^* for broadband laser ^{129}Xe SEOP are listed in Table 3.6. Clearly, laser line narrowing is beneficial for SEOP as it leads to a 9.3 fold increase of γ_{op} for the 50% xenon mixture and to the 6.4 fold increase for the 5% xenon mixture. Similar to the laser power trend, the resulting improvement of P_{Xe}^{\max} through line narrowing is particularly strong for SEOP with high xenon concentration. A 4.7 fold increase of P_{Xe}^{\max} is observed in Figure 3.8 for the 50% xenon mixture as compared to the 2.7 fold increase for the 5% xenon mixture.

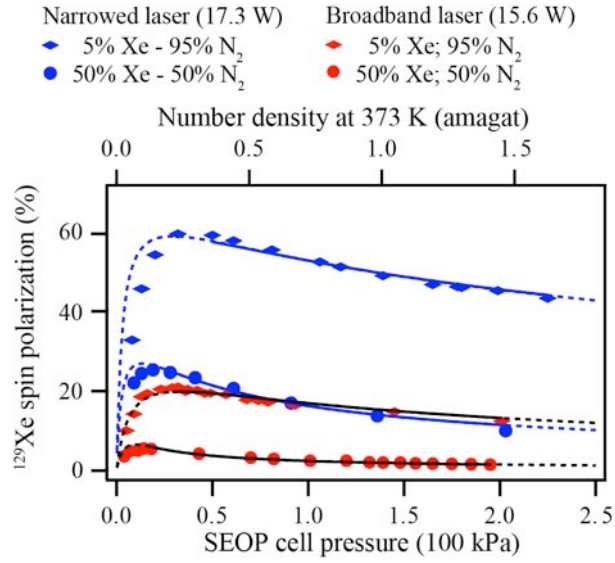


Figure 3.8. ^{129}Xe polarization, P , dependence on laser linewidth. ^{129}Xe spin polarization as a function of SEOP cell pressure with the line narrowed (0.25 nm linewidth, 17.3 W) and FAP laser irradiation (2 nm linewidth, 15.6 W). Data were analyzed using Eqs. 3.13 and 3.14 for fitting region indicated by the solid lines as discussed in *section 3.4.9*. Extrapolation using the obtained values of the fitting coefficients to pressure ranges outside the fitting range are shown by dotted lines. Results of this data analysis are listed in Table 3.6.

3.4.10 Rapid decrease of polarization with decreasing pressure below P^{max}

When the SEOP pressure was reduced below $p_{\text{tot}}^{P^{\text{max}}}$ (i.e. $p_{\text{tot}}^{P^{\text{max}}} = 20 - 35$ kPa for ^{129}Kr SEOP and $p_{\text{tot}}^{P^{\text{max}}} = 30 - 50$ kPa for ^{83}Kr SEOP) a sharp decrease in polarization was observed. Note, that data fitting was limited to pressures above $p_{\text{tot}}^{\text{max}}$, however simple extrapolation of the (high-pressure) fitting curves into the lower pressure region are shown as dotted lines in Figures 3.2 and 3.3. These extensions seem to provide a remarkably good description of the low-pressure behavior. This result should however not be over-interpreted, in particular since the assumption

of a constant γ_{vdW} will fail in the low-pressure regions (see *section 3.3.4*).

The rate γ_{vdW} , caused by spin-rotation interaction, will lead to significant depolarization at lower pressure but its effect is overestimated in this work because its absolute value will decrease with decreasing pressure.

There are further effects that contribute to the rapid polarization drop below p_{tot}^{\max} . Radiation trapping, discussed in *section 3.3.3*, reduces the rubidium electron spin polarization. Radiation trapping will increase with lower p_{tot} values, in particular in mixtures with high noble gas concentration (i.e. low nitrogen concentration) as described by Eq. 3.4.

A contribution to the polarization drop at pressures below p_{tot}^{\max} , that is not accounted for in Eq. 3.13, may be caused by an optically dense boundary layer of rubidium at the cell window that is illuminated by the laser. This layer will reduce the resonant laser light penetrating the SEOP cell at any pressure. As demonstrated by Wagshul and Chupp [35] its effect is particularly detrimental at low pressures when the resonant absorption cross section of the rubidium is very high, leading to an almost complete absorption of the resonant laser light. The situation can be alleviated by detuning the laser to (slight) off-resonant illumination [56] (not attempted in this work) and by the usage of very high laser power densities [35]. This effect was not investigated in this work.

Furthermore, the sudden drop in P_{NG} with decreasing SEOP pressure may be caused by a dramatic increase in rubidium relaxation due to the combination of increased diffusion and wall relaxation [15, 35]. The contribution of diffusion modes on the rubidium relaxation in pure nitrogen

becomes dominant and increases dramatically at pressures below 50 kPa of nitrogen [35], i.e. at a pressure slightly above p_{tot}^{max} in the current work. This effect was also not further investigated in this work.

3.5 Conclusions

Cryogen free production of hyperpolarized ^{83}Kr and hyperpolarized ^{129}Xe for practical MRI applications is possible through stopped flow SEOP with high noble gas concentrations at low total gas pressures. Without cryogenic separation the apparent polarization (as defined in Eq. 3.6) was $P_{app} = 15.5\%$ for hyperpolarized ^{129}Xe at a production rate of $1.8 \text{ cm}^3/\text{min}$ hyperpolarized gas (volume at 298 K). Respectively, an apparent polarization of $P_{app} = 4.4\%$ at a rate of $2 \text{ cm}^3/\text{min}$ was produced for hyperpolarized ^{83}Kr . These results were obtained using 23.3 W of laser power (incident at the SEOP cell) and a laser linewidth of 0.25 nm. Recompression of the hyperpolarized gases after SEOP is a necessary step with this technique and preliminary work resulted to $P_{app} = 12.4\%$ (for ^{129}Xe) and $P_{app} = 2.6\%$ (for ^{83}Kr) after recompression.

Current theory (Eq. 3.2) appears to provide a reasonable qualitative description of the SEOP gas pressure dependence of the polarization although several simplifications were used in this work. Overall, the practical application of current theory would benefit if more studies and published data were available. For instance, little is known about the actual spin-rotation parameter for various gas mixtures. Further, an experimental procedure to measure the temperature distribution within the SEOP cell would be very useful. In this work, a corrected value for the rubidium

density [Rb] was used for ^{83}Kr SEOP analysis (Eq. 3.13) that is 4 times higher than its predicted equilibrium value at the (externally) measured SEOP cell temperatures. A correction factor of 1.3 was used for ^{129}Xe SEOP analysis, although correction proved to be less important compared to ^{83}Kr SEOP. The rubidium density (and the pumping rate γ_{op} due to associated changes in laser penetration) also appeared to be dependent on the SEOP mixture, an effect attributed to different thermal conductivity of the various gas mixtures. Furthermore, the rubidium D_1 absorption linewidth dependence upon the SEOP gas pressure at 373 K was taken into account for the hyperpolarized ^{129}Xe data fitting (Eq. 3.14). The pressure dependence of the rubidium D_1 transition appeared not to be relevant for ^{83}Kr SEOP because the D_1 linewidth at 433 K is much wider than that of the narrowed diode array laser. However, a non-linear pressure broadening of the rubidium D_1 linewidth was observed in all cases and this unexpected behavior warrants further study.

High SEOP temperature is needed for ^{83}Kr in order to increase the spin exchange rate γ_{SE} for ^{83}Kr and to decrease the ^{83}Kr relaxation rate Γ . The results from ^{83}Kr SEOP inversion recovery experiments suggest that surface relaxation is a strong contributor to Γ at SEOP below 200 kPa. Therefore, higher ^{83}Kr spin polarization may be obtained through a reduction in surface to volume ratio using larger SEOP cells that reduce Γ and thus increase the ratio $\gamma_{SE}/(\gamma_{SE} + \Gamma)$ in Eq. 3.2.

The technique would benefit from future development focusing on practical hyperpolarized gas extraction-recompression units, in particular for

hyperpolarized ^{83}Kr , and on larger SEOP cell volumes to produce larger quantities of hyperpolarized noble gas within a given time interval. Larger SEOP cells, that may also improve the polarization in ^{83}Kr SEOP, will require increased laser power. Further increased laser power density at narrow laser line widths may be particularly advantageous for SEOP with high noble gas concentrations, as demonstrated in this work. Laser line narrowing to approximately 0.25 nm provides a crucial increase in ^{129}Xe polarization compared to SEOP with a 2 nm laser and further narrowing would likely be helpful for ^{129}Xe SEOP at low pressures. Finally, the general concepts of cryogen free hyperpolarized noble gas production are by no means restricted to SEOP with rubidium. SEOP with cesium vapor [46, 60, 61] has recently been shown to increase the ^{129}Xe polarization significantly compared to SEOP with rubidium [11]. The benefits of cesium vapor SEOP at low gas pressures, in particular with ^{83}Kr , are still unexplored.

3.6 References

- [1] J.S. Six, T. Hughes-Riley, K.F. Stupic, G.E. Pavlovskaya, T. Meersmann, Pathway to Cryogen Free Production of Hyperpolarized Krypton-83 and Xenon-129, *PLOS ONE*, 7 (2012) e49927.
- [2] B. Driehuys, G.D. Cates, E. Miron, K. Sauer, D.K. Walter, W. Happer, High-volume production of laser-polarized Xe-129, *Applied Physics Letters*, 69 (1996) 1668-1670.
- [3] I.C. Ruset, S. Ketel, F.W. Hersman, Optical pumping system design for large production of hyperpolarized Xe-129, *Phys. Rev. Lett.*, 96 (2006) 053002.
- [4] F.W. Hersman, I.C. Ruset, S. Ketel, I. Muradian, S.D. Covrig, J. Distelbrink, W. Porter, D. Watt, J. Ketel, J. Brackett, A. Hope, S. Patz, Large production system for hyperpolarized Xe-129 for human lung imaging studies, *Academic Radiology*, 15 (2008) 683-692.
- [5] G. Schrank, Z. Ma, A. Schoeck, B. Saam, Characterization of a low-pressure high-capacity ^{129}Xe flow-through polarizer, *Physical Review A*, 80 (2009) 063424.
- [6] D.F. Cowgill, R.E. Norberg, Spin-Lattice Relaxation and Chemical-Shift of Kr-83 in Solid and Liquid Krypton, *Physical Review B*, 8 (1973) 4966-4974.
- [7] D.F. Cowgill, R.E. Norberg, Pulsed Nmr-Studies of Self-Diffusion and Defect Structure in Liquid and Solid Krypton, *Physical Review B*, 13 (1976) 2773-2781.
- [8] N.N. Kuzma, B. Patton, K. Raman, W. Happer, Fast nuclear spin relaxation in hyperpolarized solid Xe-129, *Phys. Rev. Lett.*, 88 (2002) 147602.
- [9] G.D. Cates, R.J. Fitzgerald, A.S. Barton, P. Bogorad, M. Gatzke, N.R. Newbury, B. Saam, Rb Xe-129 Spin-Exchange Rates Due to Binary and 3-Body Collisions at High Xe Pressures, *Physical Review A*, 45 (1992) 4631-4639.
- [10] N. Whiting, P. Nikolaou, N.A. Eschmann, B.M. Goodson, M.J. Barlow, Interdependence of in-cell xenon density and temperature during Rb/ ^{129}Xe spin-exchange optical pumping using VHG-narrowed laser diode arrays, *Journal of Magnetic Resonance*, 208 (2011) 298-304.
- [11] N. Whiting, N.A. Eschmann, B.M. Goodson, M.J. Barlow, (^{129}Xe -Cs (D(1), D(2)) versus (^{129}Xe -Rb (D(1)) spin-exchange optical pumping at high xenon densities using high-power laser diode arrays, *Physical Review A*, 83 (2011) 053428.
- [12] M.G. Mortuza, S. Anala, G.E. Pavlovskaya, T.J. Dieken, T. Meersmann, Spin-exchange optical pumping of high-density xenon-129, *Journal of Chemical Physics*, 118 (2003) 1581-1584.
- [13] Z.I. Cleveland, K.F. Stupic, G.E. Pavlovskaya, J.E. Repine, J.B. Wooten, T. Meersmann, Hyperpolarized ^{83}Kr and ^{129}Xe NMR Relaxation Measurements of Hydrated Surfaces: Implications for Materials Science and Pulmonary Diagnostics, *Journal of the American Chemical Society*, 129 (2007) 1784-1792.

- [14] W. Happer, Optical-Pumping, *Reviews of Modern Physics*, 44 (1972) 169-249.
- [15] M.A. Bouchiat, J. Brossel, L.C. Pottier, Evidence for Rb Rare-Gas Molecules from Relaxation of Polarized Rb-Atoms in a Rare-Gas - Experimental Results, *Journal of Chemical Physics*, 56 (1972) 3703-3714.
- [16] T.G. Walker, W. Happer, Spin-exchange optical pumping of noble-gas nuclei, *Review of Modern Physics*, 69 (1997) 629-642.
- [17] J.N. Zerger, M.J. Lim, K.P. Coulter, T.E. Chupp, Polarization of Xe-129 with high power external-cavity laser diode arrays, *Applied Physics Letters*, 76 (2000) 1798-1800.
- [18] D. Raftery, H. Long, T. Meersmann, P.J. Grandinetti, L. Reven, A. Pines, High-Field NMR of Adsorbed Xenon Polarized by Laser Pumping, *Phys. Rev. Lett.*, 66 (1991) 584-587.
- [19] P. Nikolaou, N. Whiting, N.A. Eschmann, K.E. Chaffee, B.M. Goodson, M.J. Barlow, Generation of laser-polarized xenon using fiber-coupled laser-diode arrays narrowed with integrated volume holographic gratings, *Journal of Magnetic Resonance*, 197 (2009) 249-254.
- [20] H. Imai, J. Fukutomi, A. Kimura, H. Fujiwara, Effect of reduced pressure on the polarization of Xe-129 in the production of hyperpolarized Xe-129 gas: Development of a simple continuous flow mode hyperpolarizing system working at pressures as low as 0.15 atm, *Concepts in Magnetic Resonance Part B-Magnetic Resonance Engineering*, 33B (2008) 192-200.
- [21] D. Raftery, E. MacNamara, G. Fisher, C.V. Rice, J. Smith, Optical pumping and magic angle spinning: Sensitivity and resolution enhancement for surface NMR obtained with laser-polarized xenon, *Journal of the American Chemical Society*, 119 (1997) 8746-8747.
- [22] M. Haake, A. Pines, J.A. Reimer, R. Seydoux, Surface-enhanced NMR using continuous-flow laser-polarized xenon, *Journal of the American Chemical Society*, 119 (1997) 11711-11712.
- [23] N.J. Shah, T. Unlu, H.P. Wegener, H. Halling, K. Zilles, S. Appelt, Measurement of rubidium and xenon absolute polarization at high temperatures as a means of improved production of hyperpolarized Xe-129, *Nmr in Biomedicine*, 13 (2000) 214-219.
- [24] A.L. Zook, B.B. Adhyaru, C.R. Bowers, High capacity production of > 65% spin polarized xenon-129 for NMR spectroscopy and imaging, *Journal of Magnetic Resonance*, 159 (2002) 175-182.
- [25] K. Knagge, J. Prange, D. Raftery, A continuously recirculating optical pumping apparatus for high xenon polarization and surface NMR studies, *Chemical Physics Letters*, 397 (2004) 11-16.
- [26] T. Wakayama, M. Kitamoto, T. Ueyama, H. Imai, M. Narazaki, A. Kimura, H. Fujiwara, Hyperpolarized Xe-129 MRI of the mouse lung at a low xenon concentration using a continuous flow-type hyperpolarizing system, *Journal of Magnetic Resonance Imaging*, 27 (2008) 777-784.
- [27] Y. Hori, A. Kimura, T. Wakayama, M. Kitamoto, F. Imai, H. Imai, H. Fujiwara, 3D Hyperpolarized Xe-129 MRI of Mouse Lung at Low Xenon Concentration using a Continuous Flow-type Hyperpolarizing System: Feasibility for Quantitative Measurement of Regional Ventilation, *Magnetic Resonance in Medical Sciences*, 8 (2009) 73-79.

- [28] Z.I. Cleveland, G.E. Pavlovskaya, K.F. Stupic, C.F. LeNoir, T. Meersmann, Exploring hyperpolarized ^{83}Kr by remotely detected NMR relaxometry, *Journal of Chemical Physics*, 124 (2006) 044312.
- [29] K.F. Stupic, Z.I. Cleveland, G.E. Pavlovskaya, T. Meersmann, Hyperpolarized ^{131}Xe NMR spectroscopy, *Journal of Magnetic Resonance*, 208 (2011) 58-69.
- [30] A.H. Couture, T.B. Clegg, B. Driehuys, Pressure shifts and broadening of the Cs D(1) and D(2) lines by He, N(2), and Xe at densities used for optical pumping and spin exchange polarization, *Journal of Applied Physics*, 104 (2008) 094912.
- [31] Z.I. Cleveland, T. Meersmann, Density-independent contributions to longitudinal relaxation in ^{83}Kr , *Chemphyschem*, 9 (2008) 1375-1379.
- [32] C.J. Jameson, A.K. Jameson, J.K. Hwang, Nuclear-Spin Relaxation by Intermolecular Magnetic Dipole Coupling in the Gas-Phase - ^{129}Xe in Oxygen, *Journal of Chemical Physics*, 89 (1988) 4074-4081.
- [33] A. Michels, T. Wassenaar, G.J. Wolkers, J. Dawson, Thermodynamic Properties of Xenon as a Function of Density up to 520 Amagat and as a Function of Pressure up to 2800 Atmospheres, at Temperatures Between 0-Degrees-C and 150-Degrees-C, *Physica*, 22 (1956) 17-28.
- [34] M.S. Rosen, T.E. Chupp, K.P. Coulter, R.C. Welsh, S.D. Swanson, Polarized ^{129}Xe optical pumping/spin exchange and delivery system for magnetic resonance spectroscopy and imaging studies, *Review of Scientific Instruments*, 70 (1999) 1546-1552.
- [35] M.E. Wagshul, T.E. Chupp, Laser Optical-Pumping of High-Density Rb in Polarized ^3He Targets, *Physical Review A*, 49 (1994) 3854-3869.
- [36] A. Fink, D. Baumer, E. Brunner, Production of hyperpolarized xenon in a static pump cell: Numerical simulations and experiments, *Physical Review A*, 72 (2005) 053411.
- [37] W.J. Shao, G.D. Wang, E.W. Hughes, Measurement of spin-exchange rate constants between ^{129}Xe and alkali metals, *Physical Review A*, 72 (2005) 022713.
- [38] S.R. Schaefer, G.D. Cates, W. Happer, Determination of Spin-Exchange Parameters between Optically Pumped Rubidium and ^{83}Kr , *Physical Review A*, 41 (1990) 6063-6070.
- [39] Y.Y. Jau, N.N. Kuzma, W. Happer, Magnetic decoupling of ^{129}Xe -Rb and ^{129}Xe -Cs binary spin exchange, *Physical Review A*, 67 (2003) 022720.
- [40] T.J. Killian, Thermionic phenomena caused by vapors of rubidium and potassium, *Physical Review*, 27 (1926) 578-587.
- [41] C.B. Alcock, V.P. Itkin, M.K. Horrigan, Vapor-Pressure Equations for the Metallic Elements - 298-2500-K, *Canadian Metallurgical Quarterly*, 23 (1984) 309-313.
- [42] D.A. Steck, Rubidium 87 D Line Data, in: <http://steck.us/alkalidata>, 2010.
- [43] M.E. Wagshul, T.E. Chupp, Optical-Pumping of High-Density Rb with a Broad-Band Dye-Laser and Gaal Lasers - Application to ^3He Polarization, *Physical Review A*, 40 (1989) 4447-4454.
- [44] E.S. Hryciashyn, L. Krause, Inelastic Collisions between Excited Alkali Atoms and Molecules .7. Sensitized Fluorescence and Quenching in

- Mixtures of Rubidium with H₂, HD, N₂, CD₄, C₂H₂, and C₂H₆, *Canadian Journal of Physics*, 48 (1970) 2761-2768.
- [45] I.A. Nelson, T.G. Walker, Rb-Xe spin relaxation in dilute Xe mixtures, *Physical Review A*, 65 (2002) 012712.
- [46] X. Zeng, Z. Wu, T. Call, E. Miron, D. Schreiber, W. Happer, Experimental-Determination of the Rate Constants for Spin Exchange between Optically Pumped K, Rb, and Cs Atoms and Xe-129 Nuclei in Alkali-Metal Noble-Gas Vanderwaals Molecules, *Physical Review A*, 31 (1985) 260-278.
- [47] W. Happer, E. Miron, S. Schaefer, D. Schreiber, W.A. Vanwijngaarden, X. Zeng, Polarization of the Nuclear Spins of Noble-Gas Atoms by Spin Exchange with Optically Pumped Alkali-Metal Atoms, *Physical Review A*, 29 (1984) 3092-3110.
- [48] Y.Y. Jau, N.N. Kuzma, W. Happer, High-field measurement of the Xe-129-Rb spin-exchange rate due to binary collisions, *Physical Review A*, 66 (2002) 052710.
- [49] D.K. Walter, W.M. Griffith, W. Happer, Energy transport in high-density spin-exchange optical pumping cells, *Phys. Rev. Lett.*, 86 (2001) 3264-3267.
- [50] Z.I. Cleveland, T. Meersmann, Binary-collision-induced longitudinal relaxation in gas-phase Kr-83, *Journal of Chemical Physics*, 129 (2008) 244304.
- [51] B.C. Anger, G. Schrank, A. Schoeck, K.A. Butler, M.S. Solum, R.J. Pugmire, B. Saam, Gas-phase spin relaxation of Xe-129, *Physical Review A*, 78 (2008) 043406.
- [52] K.F. Stupic, Z.I. Cleveland, G.E. Pavlovskaya, T. Meersmann, Quadrupolar Relaxation of Hyperpolarized Krypton-83 as a Probe for Surfaces, *Solid State Nuclear Magnetic Resonance*, 29 (2006) 79-84.
- [53] Z. Wu, S. Schaefer, G.D. Cates, W. Happer, Coherent interactions of polarized nuclear spins of gaseous atoms with container walls, *Physical Review A*, 37 (1988) 1161-1175.
- [54] D. Raftery, H.W. Long, D. Shykind, P.J. Grandinetti, A. Pines, Multiple-Pulse Nuclear-Magnetic-Resonance of Optically Pumped Xenon in a Low Magnetic-Field, *Physical Review A*, 50 (1994) 567-574.
- [55] M.V. Romalis, E. Miron, G.D. Cates, Pressure broadening of Rb D-1 and D-2 lines by He-3, He-4, N-2, and Xe: Line cores and near wings, *Physical Review A*, 56 (1997) 4569-4578.
- [56] S.R. Parnell, M.H. Deppe, J. Parra-Robles, J.M. Wild, Enhancement of (129)Xe polarization by off-resonant spin exchange optical pumping, *Journal of Applied Physics*, 108 (2010) 064908.
- [57] N. Whiting, P. Nikolaou, N.A. Eschmann, M.J. Barlow, R. Lammert, J. Ungar, W. Hu, L. Vaissie, B.M. Goodson, Using frequency-narrowed, tunable laser diode arrays with integrated volume holographic gratings for spin-exchange optical pumping at high resonant fluxes and xenon densities, *Applied Physics B-Lasers and Optics*, 106 (2012) 775-788.
- [58] D.R. Lide, *CRC Handbook of Chemistry and Physics*, 82nd ed., CRC Press, New York, 2002.
- [59] A. Fink, E. Brunner, Optimization of continuous flow pump cells used for the production of hyperpolarized Xe-129: A theoretical study, *Applied Physics B-Lasers and Optics*, 89 (2007) 65-71.

- [60] D. Levron, D.K. Walter, S. Appelt, R.J. Fitzgerald, D. Kahn, S.E. Korbly, K.L. Sauer, W. Happer, T.L. Earles, L.J. Mawst, D. Botez, M. Harvey, L. DiMarco, J.C. Connolly, H.E. Moller, X.J. Chen, G.P. Cofer, G.A. Johnson, Magnetic resonance imaging of hyperpolarized Xe-129 produced by spin exchange with diode-laser pumped Cs, *Applied Physics Letters*, 73 (1998) 2666-2668.
- [61] J. Luo, X. Mao, J. Chen, S. Wang, M. Zhao, L. Fu, X. Zeng, Frequency-selective laser optical pumping and spin exchange of cesium with Xe-129 and Xe-131 in a high magnetic field, *Appl. Magn. Reson.*, 17 (1999) 587-595.

Chapter 4: Pulmonary MRI contrast using surface quadrupolar relaxation of hyperpolarized ^{83}Kr

Data presented in this chapter have been published in an article of Magnetic Resonance Imaging entitled *Pulmonary MRI contrast using Surface Quadrupolar Relaxation (SQUARE) of hyperpolarized ^{83}Kr* by Joseph S. Six, Theodore Hughes-Riley, David M.L. Lilburn, Alan C. Dorkes, Karl F. Stupic, Dominick E. Shaw, Peter G. Morris, Ian P. Hall, Galina E. Pavlovskaya, and Thomas Meersmann [1]. Mr. Six, Mr. Hughes-Riley and Dr. Lilburn performed the experiments. Dr. Lilburn handled the animals and completed the lung extraction process. Mr. Hughes-Riley and Mr. Dorkes designed the extraction unit fabricated by Mr. Dorkes. Mr. Six, Mr. Hughes-Riley, Dr. Lilburn and Dr. Pavlovskaya analyzed the data. Dr. Stupic and Dr. Pavlovskaya designed and constructed the noble gas hyperpolarizer. Dr. Shaw, Prof. Morris, and Prof. Hall were greatly consulted on the design of the experiment. Prof. Meersmann conceived the experiment. Mr. Six and Prof. Meersmann wrote the paper.

4.1 Introduction

Pulmonary MRI with hyperpolarized ^{129}Xe [2] and hyperpolarized ^3He [3] are emerging techniques for spatially resolved measurement of lung function that cannot be obtained by alternative non-invasive methods as described in the introduction to this thesis in Chapter 1. Both isotopes have a nuclear spin $I = 1/2$ that can be hyperpolarized through laser-based methods [4, 5] to obtain sufficient MRI signal intensity for high resolution imaging of the lung. Various MRI protocols can be used to generate complementary contrast from the two isotopes. For example, because of its high diffusivity, ^3He is thus far preferred for contrast relating to changes in alveolar lung structure (i.e. ADC contrast) [6-9]. The ^3He spin relaxation is more affected by the presence of paramagnetic O_2 than that of any other noble gas isotope and the ^3He T_1 relaxation can therefore be used for partial pressure measurement of pulmonary oxygen [10-12]. In regards to ^{129}Xe , the large chemical shift range leads to distinguishable MR signals between tissue dissolved and gas phase xenon [13] thus enabling the visualization of gas transport through the parenchyma [14].

Using a third noble gas isotope, namely ^{83}Kr , longitudinal (T_1) relaxation weighted MRI contrast was previously shown to be indicative of the specific surface treatment in a porous model system [15]. Unlike ^3He and ^{129}Xe , the ^{83}Kr nucleus possesses a nuclear spin $I = 9/2$ and thus a non-vanishing electric quadrupole moment that serves as a probe for electric field gradients (EFGs). The EFGs are predominantly generated during brief collision and adsorption events of the noble gas atoms with the surrounding surfaces, resulting in rapid T_1 relaxation that is detected in the gas phase.

The ^{83}Kr surface quadrupolar relaxation (SQUARE) MRI contrast is affected by the surface to volume ratio (S/V), surface composition, surface temperature, and surface adsorption of molecules [15-17].

In 2011 Stupic *et al.* demonstrated the effects of surface quadrupolar relaxation (SQUARE) in *ex vivo* rat lungs using one-dimensional spectroscopy where they attempted to determine relaxation behavior in selected regions of the lung (bronchi, bronchioles, alveoli) through various inhalation schemes [18]. Due to the limitations of the equipment and available signal intensity the determination spatial resolved ^{83}Kr relaxation times using MRI was not attempted. To date, applications of hyperpolarized ^{83}Kr pulmonary MRI are limited to low resolution images [15, 19] that reveal little internal structure or function of the lung. The lack of signal intensity and polarization losses in the ^{83}Kr delivery contributed to the limited signal in earlier studies. This work strives to overcome the limited signal intensity by improved hyperpolarization methodology to acquire spatially resolved SQUARE contrast in an *ex vivo* rat lung.

In Chapter 3 (and ref. [20]), spin exchange optical pumping (SEOP) of a mixture of 5% krypton with 95% nitrogen achieved a ^{83}Kr spin polarization of $P = 26\%$, corresponding to a 59,000 fold signal increase compared to the thermal equilibrium ^{83}Kr signal at 9.4 T field strength. SEOP at low krypton concentration was used because high krypton density $[\text{Kr}]$ adversely affects SEOP but, unfortunately, fast quadrupolar driven ^{83}Kr T_1 relaxation in the condensed state generally prevents the cryogenic separation of hyperpolarized krypton from the gas mixture [21, 22]. Therefore, the high gas dilution caused a 20 fold reduction of the MRI

signal and the ‘apparent polarization’, that takes the dilution into account, was only $P_{\text{app}} = 1.3\%$.

As an alternative to dilution, the density [Kr] can be lowered in concentrated krypton mixtures by reducing the SEOP gas pressure and described in Chapter 3 and ref. [20]. In the current work, this method is modified to extract below ambient pressure hyperpolarized gas mixture from the SEOP cell followed by compression to ambient pressure for pulmonary imaging. Hyperpolarized ^{83}Kr produced with this method is now utilized to study the concept of SQUARE MRI contrast in an excised rat lung.

4.2 Materials and methods

4.2.1 ^{83}Kr spin exchange optical pumping

Spin exchange optical pumping (SEOP) produced hyperpolarized ^{83}Kr via batch mode in a temperature controlled (433 K) cylindrical borosilicate glass cell (inner diameter = 28 mm, volume $\approx 74 \text{ cm}^3$) containing approximately 1 g of rubidium (99.75% purity, Alfa Aesar, Heysham, England, UK). A line narrowed diode-array laser system (0.25 nm output linewidth, Comet Module, Spectral Physics, Santa Clara, CA, USA) tuned to the D_1 transition of rubidium (794.7 nm) passed through telescoping lenses and polarizing optical elements to deliver 30 W of circularly polarized light in a 28 mm diameter beam to the SEOP cell. The SEOP cell was located within a 0.007 T static magnetic field that was oriented parallel with the propagation of the laser beam. Spin polarization measurements used natural abundance krypton gas (99.995% purity; 11.5% ^{83}Kr ; Airgas, Rednor, PA, USA), whereas the magnetic resonance images

presented in this publication utilized enriched ^{83}Kr (99.925% ^{83}Kr , CHEMGAS, Boulogne, France) for improved signal intensity. A 25% krypton - 75% nitrogen (99.999% purity, Air Liquide, Coleshill, UK) mixture was used for SEOP because it was previously proven in Chapter 3 (and ref. [20]) to lead to high hyperpolarized ^{83}Kr signal intensities and allowed for economical usage of the expensive isotopically enriched ^{83}Kr gas.

Spin polarization measurements were acquired using a Magritek Kea 2 spectrometer (Wellington, New Zealand) with a custom-built probe tuned to the resonance frequency of 15.4 MHz for ^{83}Kr at 9.4 T. Spin polarization was determined by comparison of the hyperpolarized gas signal with that from a thermally polarized krypton gas as described in Section 3.2.5 in Chapter 3 and ref. [20]. In baseline polarization measurements the hyperpolarized gas was transferred by gas expansion directly into a pre-evacuated borosilicate glass cell located in the r.f. detection coil without usage of the extraction unit.

Spin polarization measurements were acquired after 8 minutes of SEOP and images were acquired after 12 minutes SEOP corresponding to ~80% and ~92% of the steady state polarization (reached after 18 minutes [20]) respectively. Allowing 18 minutes for SEOP to reach steady state polarization would further improve spin polarization and subsequently the signal intensity of the images, however the reduction in spin polarization was considered acceptable in the interest of time.

4.2.2 Hyperpolarized gas extraction, compression and transfer

To utilize the enhanced ^{83}Kr spin polarization of below ambient pressure SEOP an extraction unit was designed and built that extracted the hyperpolarized gas from the SEOP cell and then delivered the gas for pulmonary imaging in a single expansion–compression cycle. The transfer of hyperpolarized gas from the low pressure SEOP cell was accomplished by expansion into a volume (V_{extract}) of a collapsible container in a purpose-built extraction unit. Volume V_{extract} needed to be substantially larger than the SEOP cell (V_{SEOP}) to allow for a rapid transfer of a large portion of the hyperpolarized gas. Forced reduction in the volume of V_{extract} pressurized the gas mixture to ambient.

The extraction unit underwent a number of iterations before a suitable design and technique was chosen and used in this study. Initially a simple device was designed using a latex balloon as the volume for V_{extract} . Although extremely simple this extraction unit was very effective at the extraction and compression of hyperpolarized ^{129}Xe gas mixtures as demonstrated elsewhere [23, 24]. Unfortunately the large surface to volume ratio of the latex balloon and the fast ^{83}Kr quadrupolar relaxation on the latex surface made the simple extraction unit unsuitable for ^{83}Kr .

An advanced extraction unit that aimed to minimize the surface to volume ratio was designed for ^{83}Kr and used in this study. The body of the extraction unit was made from an acrylic tube with acrylic screw caps that were fitted with an O-ring to seal the device. The volume V_{extract} (790 cm^3) of the extraction unit was evacuated to prepare for hyperpolarized gas

extraction via pressure equalization. The extraction and delivery process is depicted in Figure 4.1.

To reduce spin polarization losses during gas transfer, the delivery time was restricted to a few seconds resulting in approximately 6 kPa of hyperpolarized gas mixture in V_{extract} . The near equalization of pressure transferred approximately 75% of the hyperpolarized gas mixture from the SEOP cell to the extraction unit. After hyperpolarized gas extraction the SEOP cell closed and nitrogen gas pressurizes the back chamber thus driving the piston to compress the hyperpolarized gas to ambient pressure (Figure 4.1B). Additional nitrogen pressure in the back chamber then ‘injected’ the hyperpolarized gas mixture into the storage volume V_B for pulmonary MR imaging as shown in Figure 4.1C. At 90 – 100 kPa SEOP cell pressure this method produced approximately 35 - 40 cm^3 of hyperpolarized gas mixture every 12 minutes for lung imaging. Alternatively, in the spin polarization measurements the hyperpolarized gas was injected into an NMR detection cell to measure the ^{83}Kr spin polarization after the compression process.

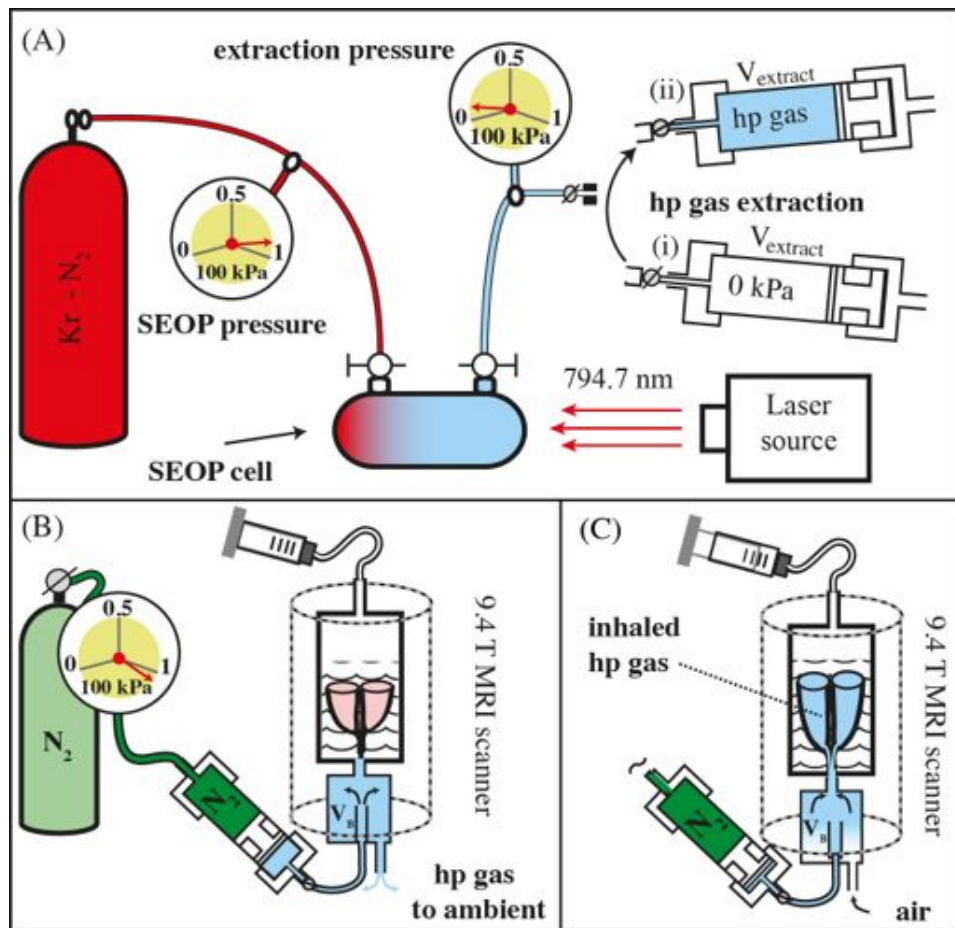


Figure 4.1. Hyperpolarized krypton extraction and transfer from the SEOP cell, operating at 90 – 100 kPa, to the lungs at ambient pressure. **(A)** A pre-evacuated volume $V_{extract} = 790 \text{ cm}^3$ in the extraction unit (i) was filled to approximately 6 kPa during hyperpolarized gas extraction (ii). **(B)** The extraction unit was moved to the MRI scanner and the nitrogen gas operated piston pressurized the hyperpolarized gas mixtures to a pressure slightly above ambient. The hyperpolarized gas was then pushed through connecting tubing into a storage container (V_B). The lung was located upside down in glucose solution within the breathing apparatus with the trachea connected to V_B . **(C)** A slight suction on the breathing apparatus (substituting for the pleural cavity) caused the lung to expand and to inhale the hyperpolarized gas.

4.2.3 Hyperpolarized gas inhalation.

A ventilation chamber was designed to substitute for the pleural cavity for the excised rat lung and allow inhalation of the hyperpolarized gas. The lung suspended in a 5% glucose solution (weight/volume) (Baxter Healthcare Ltd, Thetford, UK) within the ventilation chamber with the trachea pointed downward. The ventilation chamber containing the suspended lungs was placed inside the superconducting magnetic resonance magnet and kept at a constant temperature of 295 K. Active inhalation of the lung was achieved by applying a small negative pressure above the glucose solution from pulling a ventilation syringe to 10 cm³ as shown in Figure 4.1C (see further explanation in ref. [18]). The expansion of the lungs caused them to uptake the hyperpolarized noble gas residing in V_B. The corresponding inhaled volume of 8 cm³ was measured through exhalation causing water displacement in a water bell. This method allowed for measurement of the actual inhaled gas volume while the lungs were confined inside the magnetic resonance magnet.

4.2.4 MRI protocol

MRI experiments were performed using a vertical bore 9.4 T Bruker Avance III microimaging system (Bruker Corporation, Billerica, Massachusetts, USA). Imaging experiments utilized a Bruker 30 mm double saddle probe tuned to 15.4002 MHz corresponding to the resonance frequency of ⁸³Kr gas in the lung. Images were acquired by means of 32 linear phase encoding gradient increments using a variable flip angle (VFA) FLASH protocol (TE = 4.2 ms, TR = 19.2 ms) that neglected T₁ decay; flip angle of the ith increment (θ_i) was calculated by $\theta_i \approx \tan^{-1}\left(1/\sqrt{32-i}\right)$ [25].

The imaging protocol had a total acquisition time 0.615 s limiting the T_1 decay during acquisition.

Coronal images were acquired into 64×32 matrices resulting in a field of view (FOV) of 50.9 mm in the longitudinal (frequency encoding) and 40.7 mm in the transverse (phase encoding) directions, respectively. To acquire a non-slice selective image, 0.3 ms rectangular hard pulses of variable power levels were used for excitation. The slice selective images utilized 2 ms sinc-shaped radio frequency pulses of variable power to selectively excite a 3 mm central coronal slice of the lung, resulting in a nominal resolution of $0.80 \times 1.27 \times 3 \text{ mm}^3$.

To obtain T_1 -weighted images and demonstrate SQUARE pulmonary MRI contrast the acquisition was triggered following a time delay (t_d) of 0.0 s, 0.5 s, 1.0 s or 1.5 s after lung inhalation. Each image was acquired from a single inhalation cycle and subsequent VFA FLASH acquisition (NEX = 1) with no signal averaging. Slice selective images demonstrating SQUARE MRI contrast and the resulting T_1 map were acquired using a single animal.

4.2.5 Image reconstruction and analysis

Images were processed and reconstructed in Prospa (v. 3.06, Magritek, Wellington, New Zealand) by applying a sine-bell squared window function to the raw data before two-dimensional Fourier transformation. The two dimensional image data were exported for further analysis using IGOR Pro (v. 6.01, Wavemetrics, Lake Oswego, OR, USA).

To construct the T_1 map the image data were combined into a three dimensional matrix having two spatial dimensions (the slice selective

images) and one time dimension (the delay before acquisition). Data were then converted into a half logarithmic scale for linear regression analysis of signal intensity as a function of time that resulted in spatially resolved T_1 values. T_1 values calculated outside the lung region were composed solely of background noise and consequently insignificant. Therefore, these data were removed by applying a threshold set to 15.4% of the maximum signal intensity on the lung image for $t_d = 0$ s and then applying the resulting mask to the T_1 map. It is important to note that noise far removed from the lung remaining after the mask were also removed. The final T_1 map was then overlaid onto the lung at delay time $t_d = 0$ s for clarity of presentation.

4.2.6 Animal care and preparation

Male Sprague-Dawley rats (350 - 400 g, Charles River UK Ltd, Margate, UK) were euthanized by overdose of pentobarbital (Sigma-Aldrich Ltd, Gillingham, UK) in accordance with local animal welfare guidelines and A(SP)A 1986 (Animals for Scientific Procedures Act 1986). Immediately after confirmation of death, a catheter was inserted into the caudal vena cava to allow flushing of the pulmonary circulation with 20 – 30 cm³ heparin 100 IU/cm³ (Wockhardt UK Ltd, Wrexham, UK) in 0.9% saline solution (Baxter Healthcare Ltd, Thetford, UK) followed with phosphate buffer solution (PBS, Sigma-Aldrich Ltd, Gillingham, UK) in order to remove residual blood from the pulmonary circulation.

The heart and lungs were removed *en masse*. A polytetrafluorethylene (PTFE) adapter tube was inserted 5 - 10 mm above the carina and sutured into place. The heart and lungs were suspended in 5% glucose solution (weight/volume) with the trachea pointing downwards in a custom-built

acrylic ventilation chamber, as detailed in Figure 4.1. The *ex vivo* lungs were repeatedly inflated with 8 - 10 cm³ of room air to check for leakage either from the suture around the trachea or the lungs themselves. For the presented work the lung harvesting procedure was completed with 100% success of removing the lungs intact. Normally with a skilled operator the *ex vivo* technique results in over 90% of lungs being suitable for imaging. The lungs were chilled to 278 K for transportation to the imaging facility.

4.3 Results and Discussion.

This work required the construction of a device that is able to complete hyperpolarized gas extraction in a single expansion–compression cycle. The transfers of hyperpolarized gas mixture from the low pressure SEOP cell was accomplished by expansion into a pre-evacuated large volume of a collapsible container by pressure equalization. The volume V_{ext} of the respective gas expansion chamber was required to be much larger than that of the SEOP cell (V_{SEOP}) to allow for a rapid transfer of a large portion of the hyperpolarized gas. The extraction container was then collapsed and its contents were pressurized to ambient by the application of external gas pressure. The pure gas phase relaxation time of ⁸³Kr is sufficiently long with T_1 times of several minutes at ambient pressure [17] to permit hyperpolarized gas extraction and transfer. However, as the ⁸³Kr relaxation is accelerated by the presence of surfaces, the contact of the hyperpolarized gas with any material during this process needs to be minimized. Pumps, that are used for extraction and compression of ³He after metastable exchange optical pumping (MEOP) [26], typically require many compression cycles to transfer the entire hyperpolarized gas volume [26-

29]. For the extraction and compression of the quadrupolar ^{83}Kr a pneumatically operated piston within a large volume cylinder was designed that used a single extraction – compression cycle as shown in Figure 4.1. This design is conceptually similar to the gas pressure driven ‘syringe’ using a Teflon piston as applied previously by Rosen et al. [30] for the transfer of hyperpolarized ^{129}Xe following cryogenic gas separation. However, the extraction unit in this work needs to attain vacuum conditions of less than 0.2 kPa prior to hyperpolarized gas extraction from the SEOP cell and, following extraction, is required to compress the hyperpolarized gas to ambient pressure.

Therefore, this unit operates at a high pressure differential and an O-ring seal equipped acrylic piston provides gas tight isolation of the two compartments of the extraction unit. The setup allows for the extraction of about 3/4 of the hyperpolarized gas volume from the SEOP cell in a single expansion - compression cycle. The losses in polarization caused by compression, shown in Figure 4.2, are negligible at SEOP pressures above 75 kPa and are still acceptable down to 50 kPa. Using a 25% krypton - 75% nitrogen mixture at a pressure of 50 kPa for a SEOP duration of 8 minutes, a maximum apparent spin polarization $P_{\text{app}} = 2.9\%$ is found after extraction and transfer of the hyperpolarized gas into a sample cell as seen in Figure 4.2.

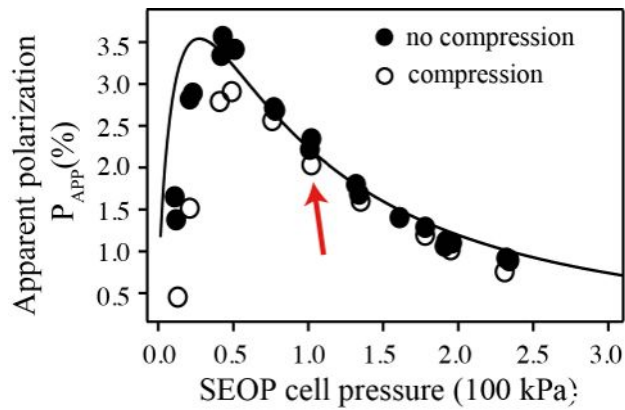


Figure 4.2. The apparent ^{83}Kr spin polarization P_{app} as a function of SEOP cell pressure using the extraction unit for compression (open circles) and baseline data without the extraction unit (filled circles). The arrow indicates the pressure used for imaging experiments. Curve fitting was adapted from ref. [20].

For the MRI, an above optimal SEOP cell pressure of 90 – 100 kPa is used, even though the attained apparent polarization is only about 2/3 the maximum value ($P_{\text{app}} = 2.0\%$). The higher SEOP pressure ensures that the quantity of the produced hyperpolarized gas (i.e. ambient pressure volume of 40 cm^3 instead of 20 cm^3 , determined from SEOP cell pressures of 100 kPa and 50 kPa respectively) is sufficient to match the actual inhaled volume and the dead volume in the gas transfer system. In particular the complete expulsion of non-hyperpolarized gas from the storage volume (V_B) in the delivery system needs to be ensured. Reducing the losses of hyperpolarized gas in the delivery system or increasing SEOP cell size would allow for improved polarization by permitting a decrease in pressure to 50 kPa.

After SEOP with isotopically enriched ^{83}Kr followed by extraction, compression, and delivery of the gas mixture into the (ambient pressure) storage chamber (V_B) located underneath the breathing apparatus, 8 cm^3 of

the hyperpolarized gas are inhaled by the excised lungs using the breathing apparatus shown in Figure 4.1B and 4.1C (see also ref. [18]). The signal intensity is sufficient to provide anatomical details using a variable flip angle (VFA) FLASH MRI protocol [25] without slice selection but also without signal averaging as shown in Figure 4.3.

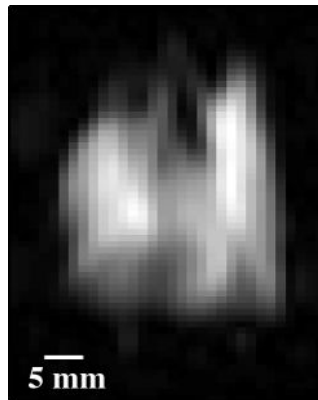


Figure 4.3. Variable flip angle (VFA) FLASH hyperpolarized ^{83}Kr MRI of an excised rat lungs at 9.4 T without signal averaging (NEX =1, no slice selection, SNR = 51) using isotopically enriched ^{83}Kr (99.925%).

The hyperpolarized ^{83}Kr presented in image shown in Figure 4.3 is a substantial improvement in resolution, SNR, and time required for acquisition when compared to previously published ^{83}Kr MRI of the lung [15, 19]. These improvements originate from a number of sources including the use of a higher power laser and utilizing the low pressure SEOP technique explored in Chapter 3 has help increase polarization values. Additionally, extraction unit developed for this work has reduced losses of polarization during delivery of the hyperpolarized gas to V_B for inhalation into the lung. Isotopically enriched ^{83}Kr in place of natural abundance has also substantially improved signal.

After the addition of 3 mm slice selection to the VFA FLASH MRI protocol, the major airways can clearly be recognized in a single acquisition (i.e. NEX = 1) as shown in Figure 4.4A. Furthermore, the obtained signal intensity is sufficient to permit the proof of principle study of surface sensitive contrast in lungs. Figure 4.4B – 4.4D show the same 3 mm slice selective hyperpolarized ^{83}Kr images as Figure 4.4A, but with a delay period t_d between inhalation and start of the image acquisition ranging from 0.5 s – 1.5 s. As a clear trend observed directly in these four images (Figure 4.4A – 4.4D), the signal originating from the major airways is less affected by the delay time than the rest of the lung. The cause for the slower relaxation is the smaller surface to volume (S/V) ratio in the airways as opposed to the alveolar space.

Smaller airways are not resolved but contribute to the contrast observed in the MR images. Figure 4.4E shows a T_1 relaxation time map obtained from the t_d dependent signal decay of each volume element in Figure 4.4A – 4.4D. The longitudinal relaxation time for the trachea is $T_1 = 5.3 \pm 1.9$ s and $T_1 = 3.0 \pm 0.9$ s for the main stem bronchus. The relaxation times measured in lung parenchyma adjacent to the major airways and in the periphery of the lung are $T_1 = 1.1 \pm 0.2$ s and $T_1 = 0.9 \pm 0.1$ s respectively. The observed T_1 data are in reasonable agreement with previous, spatially unresolved bulk measurements of ^{83}Kr T_1 relaxation in excised rat lungs that also demonstrated that the addition of up to 40% of O_2 did not significantly alter the T_1 times [18].

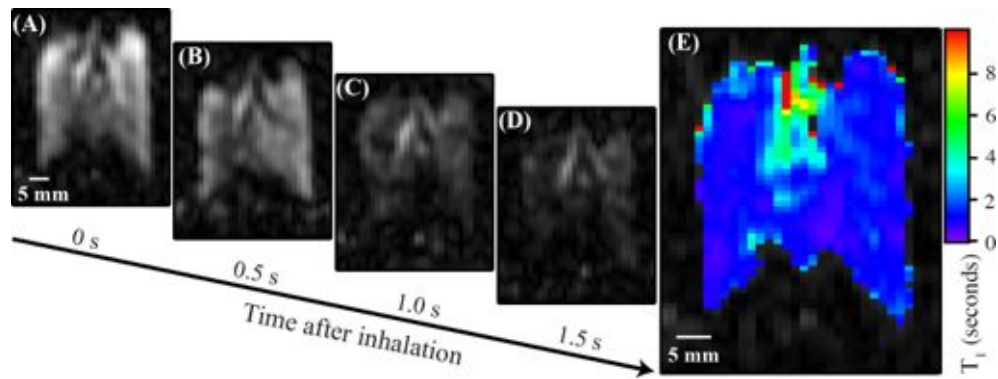


Figure 4.4. Series of hyperpolarized ^{83}Kr MRI demonstrating SQUARE contrast. A new delivery of hyperpolarized ^{83}Kr was provided for each image shown. (A) VFA FLASH MRI as in Figure 4.2B but with 3 mm slice selection. (B – D) MRI as in (A) with a relaxation delay, t_d , between hyperpolarized gas inhalation and acquisition as indicated in the figure. The major airways are visibly less affected than the alveolar space by increasing t_d values. (E) Graphical representation of the T_1 values calculated from the signal decay in (A – D) for each volume element.

As Figures 4.2 - 4.4 demonstrate, the extraction technique from low pressure (90 – 100 kPa) SEOP cells works well, generating reproducibly $P_{\text{app}} = 2.0\%$ with a 30 W line narrowed laser. This result is an approximately 10 fold increase in magnetic resonance signal intensity as compared to the previously published results on hyperpolarized ^{83}Kr MRI in excised rat lungs [19]. An additional factor of 8.7 improvement in signal to noise ratio is achieved by using isotopically enriched to 99.925% ^{83}Kr gas. Not surprisingly for a spin system with $P_{\text{app}} = 2\%$, the obtained resolution falls short compared to ventilation hyperpolarized ^{129}Xe MRI. However, the ^{83}Kr signal intensity is strong enough to allow for surface sensitive contrast in excised lungs while retaining structural resolution. The resolution obtained with hyperpolarized ^{83}Kr MRI is similar to dissolved phase ^{129}Xe pulmonary MRI that uses the small fraction (typically 1 – 2%) of inhaled xenon dissolved in tissue and blood.

Signal averaging will improve the signal intensity of the hyperpolarized ^{83}Kr MRI for *in vivo* applications but will also contribute to artifacts due to inhalation variations during breathing. Furthermore, the applied laser power of 30 W can be increased significantly due to recent advances in solid state laser technology and may thus improve the quantity of the produced hyperpolarized gas and its spin polarization. Larger volume SEOP cells could be used to produce larger quantities of hyperpolarized gas volumes at lower pressures if the power density of the laser irradiation is maintained across the larger cross section. Alternatively, the volume of hyperpolarized gas can also be increased if several SEOP units of the current cell size and laser power operate in parallel. The amount of hyperpolarized gas needed per inhalation cycle may additionally be reduced by optimizing the ambient pressure storage container (V_B), consequently allowing for lower SEOP cell pressures that result in higher spin polarization with the current setup.

A potential drawback of the presented methodology is that the lungs may become contaminated by rubidium vapors during the rapid delivery of hyperpolarized gas from the SEOP cell. Therefore, the extraction unit, that serves for temporal storage of hyperpolarized ^{83}Kr before delivery to the lungs, is tested for rubidium contamination by brushing the inside of the transfer chamber with a cotton swab. After adding a few drops of water no increase in the pH value is found for the swab using a simple (ColorpHast) pH indicator strip. Although more elaborate testing is required than this relatively crude method, the presence of substantial quantities of rubidium in the extraction unit can be ruled out and it appears that most of the

rubidium tends to condense in the tubing located before the extraction unit. The use of simple filter may improve the situation further but was not explored.

4.4 Conclusion

The cryogen free production of hyperpolarized ^{83}Kr discussed in Chapter 3 allowed for the high ^{83}Kr polarization reported here. A purpose built extraction unit transferred the hyperpolarized noble gas from the SEOP to the excise rat lung with small losses in the polarization. Further improvements to the extraction unit may be possible but not attempted in this study. The ^{83}Kr relaxation may be reduced if the extraction unit was fabricated from borosilicate glass, which minimizes longitudinal relaxation, in place of acrylic tubing.

The improved magnetization and consequent signal intensity permitted the demonstration of pulmonary SQUARE MRI contrast. This technique confirmed previously acquired measurements [18] between airways and alveolar regions by spatially resolved relaxation measurements in the lung. Lung pathology related contrast was not attempted as animal models of pulmonary disease were beyond the scope of this proof of concept study. However, the produced signal intensity will be sufficient to attempt disease specific contrast in pathophysiology and to explore whether hyperpolarized ^{83}Kr is of supplemental diagnostic value to hyperpolarized ^3He and hyperpolarized ^{129}Xe MRI.

The potential usage of hyperpolarized ^{83}Kr as a novel contrast agent should be investigated for disorders such as emphysema where the lung surface to volume ratio (S/V) is reduced [31, 32]. Currently there is a study

[33] being conducted by the Translational Imaging Research Group under the supervision of Thomas Meersmann in collaboration with Mark Birrell and Maria Belvisi from Imperial College London investigating the relaxation of ^{83}Kr in lungs affected by the elastase model of emphysema [34] where there is destruction of alveoli architecture. Preliminary results using SQUARE MRI with hyperpolarized ^{83}Kr are shown by a histogram in Figure 4.5.

Initial data suggests that hyperpolarized ^{83}Kr is a potential tool to distinguish healthy and elastase disease model lungs. A larger sample size is required to conclusively determine the utility of the method. The disease model shows a shift to longer T_1 times arising from the decrease in S/V caused by the elastase model of emphysema. There also appears to be a wider distribution of T_1 values for the disease model data; possibly indicating inhomogeneous distribution of the disease.

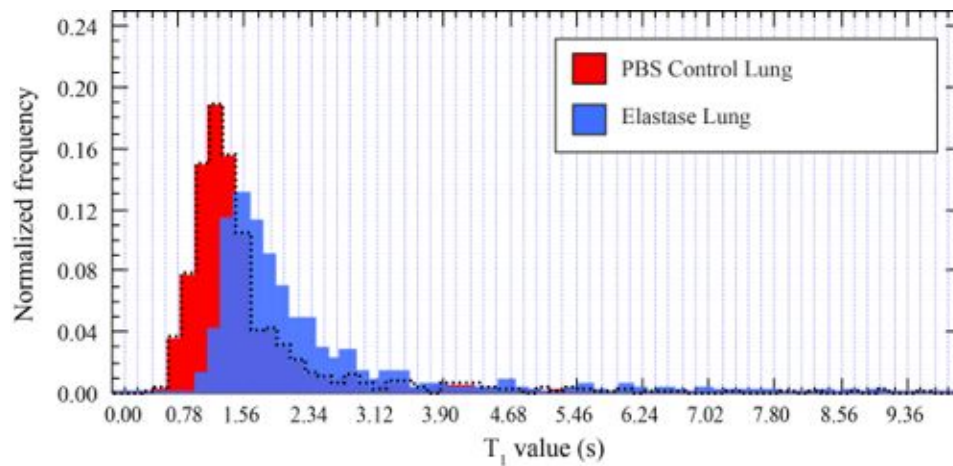


Figure 4.5. Histogram of the T_1 values taken from T_1 relaxation maps (not shown) for control and diseased lungs. See legend for color explanation. The T_1 map was generated using the technique describe in this chapter. The histogram displays the frequency of occurrence for each T_1 value, normalized for the amount of voxels in the lung region. Please note that the data presented in Figure 4.5 is from a pilot study currently underway [33] and the method of evaluating the data is in development.

In addition to disorders effecting S/V, SQUARE ^{83}Kr MRI may also be beneficial for the broad spectrum of diseases which exhibit significant changes in lung surface chemistry, for example acute lung injury (ALI), acute respiratory syndrome (ARDS) [35] and cystic fibrosis (CF) [36]. Two final notes with regard to practicalities of hyperpolarized ^{83}Kr MRI: (1) krypton gas (natural abundance of 12.4% ^{83}Kr) is a renewable resource generated as a by-product of air liquefaction, available at approximately € 1 per liter (at ambient pressure). Unfortunately, isotopically enriched ^{83}Kr is costly (approximately € 4000/L) at the current low demand for production. (2) There are little toxicological concerns for future clinical applications as krypton is chemically inert and does not exhibit anesthetic properties at ambient gas pressure [37, 38].

4.5 References

- [1] J.S. Six, T. Hughes-Riley, D.M.L. Lilburn, A.C. Dorkes, K.F. Stupic, D.E. Shaw, P.G. Morris, I.P. Hall, G.E. Pavlovskaya, T. Meersmann, Pulmonary MRI contrast using Surface Quadrupolar Relaxation (SQUARE) of hyperpolarized ^{83}Kr , *Magnetic Resonance Imaging*, (2013) <http://dx.doi.org/10.1016/j.mri.2013.1008.1007>.
- [2] M.S. Albert, G.D. Cates, B. Driehuys, W. Happer, B. Saam, C.S. Springer, A. Wishnia, Biological Magnetic-Resonance-Imaging Using Laser Polarized Xe-129, *Nature*, 370 (1994) 199-201.
- [3] H. Middleton, R.D. Black, B. Saam, G.D. Cates, G.P. Cofer, R. Guenther, W. Happer, L.W. Hedlund, G.A. Johnson, K. Juvan, J. Swartz, Mr-Imaging with Hyperpolarized He-3 Gas, *Magn. Reson. Med.*, 33 (1995) 271-275.
- [4] D. Raftery, H. Long, T. Meersmann, P.J. Grandinetti, L. Reven, A. Pines, High-Field NMR of Adsorbed Xenon Polarized by Laser Pumping, *Phys. Rev. Lett.*, 66 (1991) 584-587.
- [5] T.G. Walker, W. Happer, Spin-exchange optical pumping of noble-gas nuclei, *Review of Modern Physics*, 69 (1997) 629-642.
- [6] B.T. Saam, D.A. Yablonskiy, V.D. Kodibagkar, J.C. Leawoods, D.S. Gierada, J.D. Cooper, S.S. Lefrak, M.S. Conradi, MR imaging of diffusion of He-3 gas in healthy and diseased lungs, *Magn. Reson. Med.*, 44 (2000) 174-179.
- [7] M. Salerno, E.E. de Lange, T.A. Altes, J.D. Truwit, J.R. Brookeman, J.P. Mugler, Emphysema: Hyperpolarized Helium 3 Diffusion MR Imaging of the Lungs Compared with Spirometric Indexes, *Initial Experience*, *Radiology*, 222 (2002) 252-260.
- [8] A.L. Sukstanskii, M.S. Conradi, D.A. Yablonskiy, He-3 lung morphometry technique: Accuracy analysis and pulse sequence optimization, *Journal of Magnetic Resonance*, 207 (2010) 234-241.
- [9] J. Parra-Robles, S. Ajraoui, M.H. Deppe, S.R. Parnell, J.M. Wild, Experimental investigation and numerical simulation of (^3He) gas diffusion in simple geometries: Implications for analytical models of (^3He) MR lung morphometry, *Journal of Magnetic Resonance*, 204 (2010) 228-238.
- [10] A.J. Deninger, B. Eberle, M. Ebert, T. Grossmann, G. Hanisch, W. Heil, H.U. Kauczor, K. Markstaller, E. Otten, W. Schreiber, R. Surkau, N. Weiler, He-3-MRI-based measurements of intrapulmonary $p(\text{O}_2)$ and its time course during apnea in healthy volunteers: first results, reproducibility, and technical limitations, *NMR Biomed.*, 13 (2000) 194-201.
- [11] M.C. Fischer, Z.Z. Spector, M. Ishii, J. Yu, K. Emami, M. Itkin, R. Rizi, Single-acquisition sequence for the measurement of oxygen partial pressure by hyperpolarized gas MRI, *Magn. Reson. Med.*, 52 (2004) 766-773.
- [12] G.E. Santyr, W.W. Lam, J.M. Parra-Robles, T.M. Taves, A.V. Ouriadov, Hyperpolarized noble gas magnetic resonance imaging of the animal lung: Approaches and applications, *Journal of Applied Physics*, 105 (2009).
- [13] J.P. Mugler, T.A. Altes, I.C. Ruset, I.M. Dregely, J.F. Mata, G.W. Miller, S. Ketel, J. Ketel, F.W. Hersman, K. Ruppert, Simultaneous magnetic resonance imaging of ventilation distribution and gas uptake in the

human lung using hyperpolarized xenon-129, Proceedings of the National Academy of Sciences of the United States of America, 107 (2010) 21707-21712.

[14] B. Driehuys, G.P. Cofer, J. Pollaro, J.B. Mackel, L.W. Hedlund, G.A. Johnson, Imaging alveolar-capillary gas transfer using hyperpolarized Xe-129 MRI, Proceedings of the National Academy of Sciences of the United States of America, 103 (2006) 18278-18283.

[15] G.E. Pavlovskaya, Z.I. Cleveland, K.F. Stupic, T. Meersmann, Hyperpolarized Krypton-83 as a New Contrast Agent for Magnetic Resonance Imaging, Proceedings of the National Academy of Sciences of the United States of America, 102 (2005) 18275-18279.

[16] Z.I. Cleveland, K.F. Stupic, G.E. Pavlovskaya, J.E. Repine, J.B. Wooten, T. Meersmann, Hyperpolarized ^{83}Kr and ^{129}Xe NMR Relaxation Measurements of Hydrated Surfaces: Implications for Materials Science and Pulmonary Diagnostics, Journal of the American Chemical Society, 129 (2007) 1784-1792.

[17] D.M.L. Lilburn, G.E. Pavlovskaya, T. Meersmann, Perspectives of hyperpolarized noble gas MRI beyond ^3He , J. Magn. Reson., (2012).

[18] K.F. Stupic, N.D. Elkins, G.E. Pavlovskaya, J.E. Repine, T. Meersmann, Effects of pulmonary inhalation on hyperpolarized krypton-83 magnetic resonance T-1 relaxation, Physics in Medicine and Biology, 56 (2011) 3731-3748.

[19] Z.I. Cleveland, G.E. Pavlovskaya, N.D. Elkins, K.F. Stupic, J.E. Repine, T. Meersmann, Hyperpolarized Kr-83 MRI of lungs, Journal of Magnetic Resonance, 195 (2008) 232-237.

[20] J.S. Six, T. Hughes-Riley, K.F. Stupic, G.E. Pavlovskaya, T. Meersmann, Pathway to Cryogen Free Production of Hyperpolarized Krypton-83 and Xenon-129, PLOS ONE, 7 (2012) e49927.

[21] D.F. Cowgill, R.E. Norberg, Spin-Lattice Relaxation and Chemical-Shift of Kr-83 in Solid and Liquid Krypton, Physical Review B, 8 (1973) 4966-4974.

[22] D.F. Cowgill, R.E. Norberg, Pulsed Nmr-Studies of Self-Diffusion and Defect Structure in Liquid and Solid Krypton, Phys. Rev. B, 13 (1976) 2773-2781.

[23] D.M.L. Lilburn, T. Hughes-Riley, J.S. Six, D.E. Shaw, G.E. Pavlovskaya, T. Meersmann, Validating excised rodent lung for functional hyperpolarized xenon-129 MRI, (2013).

[24] T. Hughes-Riley, J.S. Six, D.M.L. Lilburn, K.F. Stupic, A.C. Dorkes, D.E. Shaw, G.E. Pavlovskaya, T. Meersmann, Cryogenics free production of hyperpolarized ^{129}Xe and ^{83}Kr for biomedical MRI applications, Journal of Magnetic Resonance, 237 (2013) 23-33.

[25] L. Zhao, R. Mulkern, C.H. Tseng, D. Williamson, S. Patz, R. Kraft, R.L. Walsworth, F.A. Jolesz, M.S. Albert, Gradient-echo imaging considerations for hyperpolarized Xe-129 MR, Journal of Magnetic Resonance Series B, 113 (1996) 179-183.

[26] R.S. Timsit, J.M. Daniels, E.I. Dennig, A.K.C. Kiang, A.D. May, An Experiment to Compress Polarized ^3He Gas, Canadian Journal of Physics, 49 (1971) 508-516.

[27] J. Becker, W. Heil, B. Krug, M. Leduc, M. Meyerhoff, P.J. Nacher, E.W. Otten, T. Prokscha, L.D. Scheerer, R. Surkau, Study of mechanical

- compression of spin-polarized He-3 gas Nuclear Instruments & Methods in Physics Research Section a-Accelerators Spectrometers Detectors and Associated Equipment, 346 (1994) 45-51.
- [28] T.R. Gentile, G.L. Jones, A.K. Thompson, R.R. Rizi, D.A. Roberts, I.E. Dimitrov, R. Reddy, D.A. Lipson, W. Gefter, M.D. Schnall, J.S. Leigh, Demonstration of a compact compressor for application of metastability-exchange optical pumping of He-3 to human lung imaging, *Magn. Reson. Med.*, 43 (2000) 290-294.
- [29] H. Imai, J. Fukutomi, A. Kimura, H. Fujiwara, Effect of reduced pressure on the polarization of Xe-129 in the production of hyperpolarized Xe-129 gas: Development of a simple continuous flow mode hyperpolarizing system working at pressures as low as 0.15 atm, *Concepts in Magnetic Resonance Part B-Magnetic Resonance Engineering*, 33B (2008) 192-200.
- [30] M.S. Rosen, T.E. Chupp, K.P. Coulter, R.C. Welsh, S.D. Swanson, Polarized Xe-129 optical pumping/spin exchange and delivery system for magnetic resonance spectroscopy and imaging studies, *Review of Scientific Instruments*, 70 (1999) 1546-1552.
- [31] W.M. Thurlbeck, Internal Surface Area and Other Measurements in Emphysema, *Thorax*, 22 (1967) 483-496.
- [32] G.D. Massaro, D. Massaro, Retinoic acid treatment abrogates elastase-induced pulmonary emphysema in rats, *Nature Medicine*, 3 (1997) 675-677.
- [33] D.M.L. Lilburn, J.S. Six, C. Lesbats, T. Hughes-Riley, D.E. Shaw, G.E. Pavlovskaya, M.G. Belvisi, M.A. Birrell, T. Meersmann, MRI of hyperpolarized ⁸³Kr surface quadrupolar relaxation in an ex vivo model of emphysema, in, University of Nottingham, Unpublished work, Nottingham, UK, 2013.
- [34] M.A. Birrell, S. Wong, D.J. Hele, K. McCluskie, E. Hardaker, M.G. Belvisi, Steroid-resistant inflammation in a rat model of chronic obstructive pulmonary disease is associated with a lack of nuclear factor-kappa B pathway activation, *American Journal of Respiratory and Critical Care Medicine*, 172 (2005) 74-84.
- [35] A. Gunther, C. Siebert, R. Schmidt, S. Ziegler, F. Grimminger, M. Yabut, B. Temmesfeld, D. Walmrath, H. Morr, W. Seeger, Surfactant alterations in severe pneumonia, acute respiratory distress syndrome, and cardiogenic lung edema, *Am. J. Respir. Crit. Care Med.*, 153 (1996) 176-184.
- [36] J.J. Smith, S.M. Travis, E.P. Greenberg, M.J. Welsh, Cystic fibrosis airway epithelia fail to kill bacteria because of abnormal airway surface fluid, *Cell*, 85 (1996) 229-236.
- [37] S.C. Cullen, E.G. Gross, The Anesthetic Properties of Xenon in Animals and Human Beings, with Additional Observations on Krypton, *Science*, 113 (1951) 580-582.
- [38] A.-L. Hachulla, F.o. Pontana, L. Wemeau-Stervinou, S. Khung, J.-B. Faivre, B. Wallaert, J.-F.o. Cazaubon, A. Duhamel, T. Perez, P. Devos, J. Remy, M. Remy-Jardin, Krypton Ventilation Imaging Using Dual-Energy CT in Chronic Obstructive Pulmonary Disease Patients: Initial Experience, *Radiology*, 263 (2012) 253-259.

Chapter 5: Diffusion of ^{129}Xe and ^{83}Kr through internal magnetic field gradients

5.1 Introduction

Signal attenuation of spin echoes originating from diffusion through magnetic field gradients has been of interest since the early days of NMR when researchers found that the self-diffusion coefficient could be determined from spin echoes [1] or spin echo trains [2]. Torrey then used an analytical approach to theoretically explain the signal attenuation by adding diffusion terms into the Bloch equations [3]; finding an equation that agreed with the prior experimental results. Though the initial experiments were relatively straightforward, diffusion caused transverse relaxation is challenging to generalize [4] and consequently warrants research interest to this date (refer to recent conference proceedings for examples of current studies: [5-8]).

The majority of studies have investigated diffusion of liquids in porous material. Particular attention, motivated by the petroleum industry, has concentrated on restricted diffusion in porous rock [9, 10] to the determine of oil and water content in the pores [11-13]. The relatively slow movement of atoms in the liquid state limits the diffusion length thereby restricting the size of pores that can be investigated. As an alternative, gases can be used in place of liquids in systems with large pores [14, 15] because

the diffusion of a gas is much greater than that of a liquid on the same time scale. Gases require either high gas pressure, a large number of acquisitions, or enhanced signal intensity through hyperpolarization techniques to have satisfactory magnetic resonance signal intensity due to low density of spins.

Most studies involving restricted diffusion use pulsed gradient spin echo (PGSE) experiments [16] that have an externally applied gradient to observe time-dependent diffusion. The principles of PGSE experiments have enabled the spatially resolved measurement of the apparent diffusion coefficient (ADC) for ^3He and ^{129}Xe in lungs [17]. As an alternative internal magnetic field gradients, inherent and unique to a sample, also contain information such as pore size and surface-to-volume ratio [18].

This work investigated the transverse relaxation of gaseous hyperpolarized ^{129}Xe and ^{83}Kr caused by diffusion through internal magnetic field gradients. Systems of both free diffusion and restricted diffusion in porous media were used to understand the behavior of the gas. Information may prove useful in hyperpolarized noble gas pulmonary imaging where a fundamental understanding of the diffusion of the gas will be helpful in data interpretation and may help improve imaging strategies. For example, manipulation of the transverse relaxation to maximize T_2 , to the extent possible under experimental conditions, will help improve signal intensity by reducing relaxation during gradient echo imaging techniques commonly used.

5.2 Background

CPMG sequences are built around the single spin echo concept but acquire a train of spin echoes made by subsequent π (180°) pulses that

continually refocus the transverse magnetization (refer to Figure 2.8 and discussion in Chapter 2 for further explanation of the CPMG sequence). Because the train of echoes is acquired in a single experiment, CPMG is more efficient than an individual spin echo method where each time increment requires a separate experiment with a new ‘batch’ of hyperpolarized gas delivery. It is important to note that the result is dependent on the CPMG parameters and will be denoted as T_2^{CPMG} and CPMG parameters must be considered during data interpretation.

To describe signal attenuation caused by diffusion during a train of spin echoes, Carr and Purcell [2] treated diffusion as a random walk of discrete steps to a new location. At each location the nucleus would precess at the Larmor frequency according to the strength of the external magnetic field. Therefore, the phase shift from the different precession frequencies serves to store information of not only current location but also a memory of past locations. Culminating all the spins, the signal attenuation of the ensemble during a CPMG sequence follows [2, 3]:

$$M(t) = M_0 \exp\left[(-t/T_2) + \left(-\frac{1}{3}D\gamma^2 G^2 \tau^2 t\right)\right], \quad (5.1)$$

which can be expressed as:

$$\ln\left(\frac{M(t)}{M_0}\right) = \left(-1/T_2 + -\frac{1}{3}D\gamma^2 G^2 \tau^2\right)t = \left(-1/T_2^{CPMG}\right)t. \quad (5.2)$$

From Eq. 5.2 it can be concluded that the CPMG transverse relaxation time, T_2^{CPMG} , is calculated as the sum of the intrinsic transverse relaxation and transverse relaxation caused from diffusion [3]:

$$1/T_2^{CPMG} = 1/T_2 + \frac{1}{3}D\gamma^2 G^2 \tau^2. \quad (5.3)$$

In Eqs. 5.1-5.3, D is the diffusion coefficient, γ is the gyromagnetic ratio, G is the magnetic field gradient, and τ is the time between $\pi/2$ and first π pulse (1/2 the time between subsequent π pulses). The magnetic field gradient can be from either an externally applied gradient or the internal gradients of the sample.

In the following experiments the composition of the gas mixture and gas pressure in the sample cell during the CPMG sequence are individually adjusted to investigate the diffusion behavior. The dependence of $1/T_2^{CPMG}$ (described using Eq. 5.3) on the gas pressure during the experiment may be explained by the kinetic gas theory where diffusion is defined as the product of the mean free path (λ) and the mean thermal speed (\bar{c}) divided by the dimension of the considered space, $D = \frac{1}{3}(\lambda \cdot \bar{c})$. The mean free path is the distance travelled by an atom before a collision with a second body. Assuming that the atoms or molecules are hard spheres that have no interactions the mean free path is described by:

$$\lambda = \frac{1}{\sqrt{2}\pi\sigma^2 N_v} \quad (5.4)$$

where: σ is the collisional cross-section and N_v is the number of atoms per unit volume. In the case of an ideal gas where pressure, $P = N_v k_B T$ the mean free path is:

$$\lambda = \frac{k_b T}{\sqrt{2}\pi\sigma^2 P} \quad (5.5)$$

where, σ is the collisional diameter, P is the pressure, k_b is Boltzmann's constant, T is the temperature. The mean thermal speed of atoms with molar

mass m , if assumed to follow Maxwell's distribution of an ideal gas, is determined by:

$$\bar{c} = \left(\frac{8k_b T}{\pi m} \right)^{1/2}. \quad (5.6)$$

Substituting Eqs. 5.5 and 5.6 into the definition of diffusion and assuming the case of self-diffusion of an ideal gas determines the diffusion coefficient as:

$$D = \frac{2}{3\sigma^2 P} \left(\frac{k_b^3 T^3}{\pi^3 m} \right)^{1/2}. \quad (5.7)$$

The simplicity of Eq. 5.7 helped to qualitatively describe diffusion and helped in designing the experiments of this work. However, Eq. 5.7 is inadequate in quantifying the diffusion in the following discussions.

There are two major shortcomings in using Eq. 5.7 for calculations: (1) intermolecular (or interatomic in the case of a noble gas) interactions make the gases behave non-ideally and (2) this work uses gas mixtures containing buffer gases that require inclusion in the calculation. These buffer gases were necessary for efficient hyperpolarization of ^{129}Xe and ^{83}Kr (as discussed previously in Chapter 3). It is important to consider alterations to the diffusion coefficient caused by the mixture of gases.

To account for intermolecular interactions and buffer gases a more rigorous description of diffusion is necessary. Hirschfelder, Curtiss, and Bird describe a method using the work of Chapman and Enskog that estimates intermolecular interactions between non-polar gases by a Lennard-Jones 6-12 potential [19, 20] and approximates diffusion coefficients with strong agreement to experimental data [21]. For a binary

mixture the first approximation of the coefficient of mutual diffusion ($D_{1,2}$) can be calculated using [20]:

$$D_{1,2} = 266.28 \left(\frac{\sqrt{T^3 (M_1 + M_2) / 2 M_1 M_2}}{P \sigma_{1,2}^2 \Omega_{1,2}} \right). \quad (5.8)$$

In Eq. 5.8, $D_{1,2}$ is the mutual diffusion coefficient (in cm^2/s) of a mixture containing gases 1 and 2, P is the pressure (in Pa), T is the temperature (in K), M_1 and M_2 are the molar masses (in g/mol) of the species in the binary mixture. The collisional diameter of the binary mixture is $\sigma_{1,2} = \frac{1}{2}(\sigma_1 + \sigma_2)$ (in Å). $\Omega_{1,2}$ is the interaction potential that is a function of the reduced temperature $T_{1,2}^*$ where $T_{1,2}^* = k_b T / \varepsilon_{1,2}$. The term ε defines the strength of the intermolecular interaction (i.e. the depth of the potential well in the Lennard-Jones 6-12 potential) and in the cases of a binary mixture $\varepsilon_{1,2} = \sqrt{\varepsilon_1 \varepsilon_2}$. Literature values for σ and ε are provided in Table 5.1. This work utilized the values for $\Omega_{1,2}$ corresponding to a Lennard-Jones 6-12 potential which are tabulated in the appendix of ref. [22]. A second order correction may be included into Eq. 5.8 to account for composition of the binary mixture, however, with the parameters of this work the correction is less than 1% [23] and considered trivial in calculations. Therefore the first order approximation of the diffusion coefficient, $D_{1,2}$, described in Eq. 5.8 was used to analyse the data collected for this study.

Table 5.1. Literature values of required for the calculations of the diffusion coefficient of the relevant gases.

Gas	ϵ/k_b (K)	σ (Å)
He	10.22	2.58
N ₂	91.5	3.68
Kr	190	3.61
Xe	229	4.06

Values taken from the appendix of ref. [22].

The behavior of gas diffusion is not only dependent on the property of the gas but is also dependent on the sample. In porous media the gas may collide or interact with the surfaces of the pore altering the observed relaxation. In porous media, there are three distinct diffusion regimes: free diffusion, localization, and motional averaging (see sketch in Figure 5.1). Free diffusion occurs when there is no interaction between the atom of interest and boundaries of the pore. Localization results when the atom of interest diffuses through only a small portion of the pore during the relevant time scale; for example, when the atom only experiences the region near the pore boundary. Motional averaging occurs when the atom of interest experiences the entirety of pore, perhaps multiple times, averaging out the overall gradient it experiences.

The regime is determined by the shortest of the three characteristic length scales which are defined as: (1) the diffusion length, $l_D = \sqrt{D_{1,2}t}$, (2) the dephasing length, $l_G = \sqrt[3]{D_{1,2}/\gamma G}$ (where G is the local, or internal, field gradient), and (3) the size of the pore, l_s [24]. A cleverly chosen model system may attempt to probe a single regime. However, in realistic systems more than one, if not all, regimes may exist due to variation in the sample

and deconvolution of the relaxation from each regime may not be straightforward.

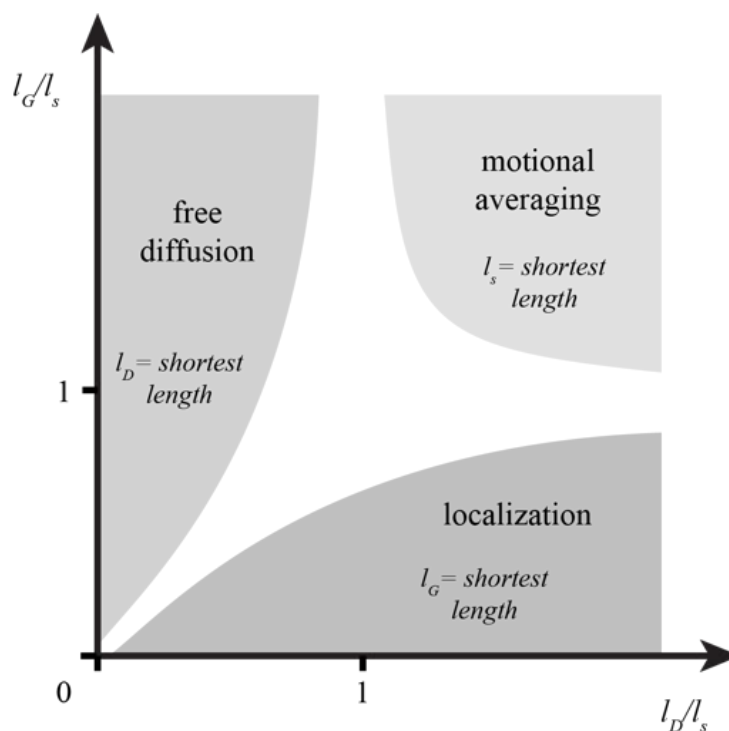


Figure 5.1. Sketch of the three diffusion regimes and their dependence on length scales l_D , l_G , and l_s . The shortest characteristic length scale determines the regime. Figure adapted from Refs. [24, 25].

5.3 Transverse relaxation of ^{129}Xe in single pore

5.3.1 Materials and methods

5.3.1.1 ^{129}Xe spin exchange optical pumping

Spin exchange optical pumping (SEOP) produced hyperpolarized ^{129}Xe using a batch mode technique similar to what was extensively described in *section 3.2* of Chapter 3. The primary difference to the earlier experiment was that this work used an SEOP time of 3 minutes resulting in reduced spin polarization compared to the 6 minutes required for steady state polarization. However, reduced SEOP time produced ample signal for

the single pore (empty glass cell) CPMG experiments while increasing data collection rate.

5.3.1.2 CPMG experiments

The transverse relaxation of ^{129}Xe was measured in a 9.4 T superconducting magnet by means of a CPMG sequence on a Kea 2 spectrometer (Magritek, NZ). A single pore for gas diffusion was created by an empty 12 mm inner diameter (14 mm outer diameter) borosilicate glass detection cell and kept at a temperature of 290-292 K during experiments. Hyperpolarized ^{129}Xe mixture was transferred into an evacuated detection cell via pressure equalization and allowed to pressure and temperature equilibrate in the cell for 30 seconds before the triggering the CPMG pulse sequence. This work studied the gradients inherent in the sample (i.e. no gradients applied by an external mechanism). Example data from a CPMG sequence is shown in Figure 5.2. At each pressure, a simple one-pulse experiment acquired a one-dimensional spectrum to set the ^{129}Xe resonance frequency at that pressure and also to determine T_2^* from the FWHM (ν) using the relation $\nu = 1/\pi T_2^*$. Additional experimental details such as the inter-echo spacing and CPMG train length are provided for each individual CPMG experiment in the Results and Discussion section. Two separate superconducting magnets were used for these experiments: (1) a 9.4 T superconducting magnet (Oxford Instruments) where only superconducting shims are used resulting in a substantial magnetic field gradient over the sample and subsequently a broad linewidth ($T_2^* = 3.06 \pm 0.08$ ms for the free ^{129}Xe gas) and (2) a second 9.4 T superconducting magnet (Bruker Corporation) that employs room temperature shims to improve magnetic

field homogeneity and results in a narrow linewidth ($T_2^* = 83.9 \pm 0.7$ ms for the free ^{129}Xe gas).

5.3.1.3 Data analysis

The signal of the echo train, measured by the integrated peak area of each echo, revealed that the relaxation behavior followed a bi-exponential decay as apparent in the natural logarithm of the data in Figure 5.2 (filled black circles). The T_2^{CPMG} values were extrapolated from the decay curve using:

$$I / I_0(t) = (1 - A) \cdot \exp(-t / T_{2a}) + A \cdot \exp(-t / T_{2b}) \quad (5.9)$$

where T_{2a} and T_{2b} are the two components of the overall T_2^{CPMG} value. All data were fit to the point where the normalized integral (I) was 0.1 of initial value (I_0).

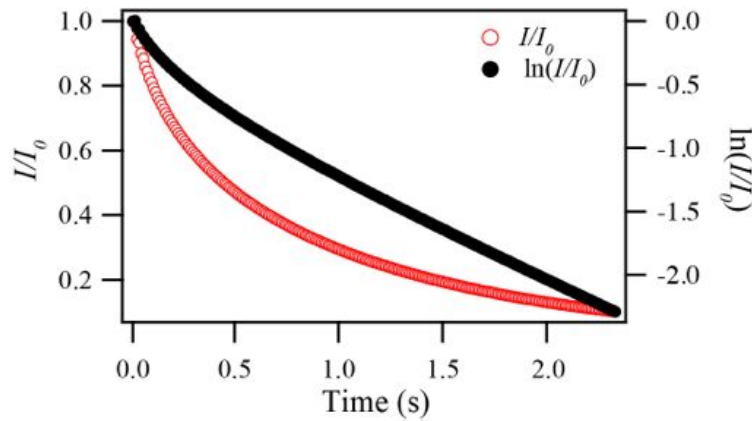


Figure 5.2. Example data from a CPMG experiment of hyperpolarized ^{129}Xe in an empty glass detection cell containing no porous medium at 287.5 kPa of a 25% xenon – 75% nitrogen gas mixture and $\tau = 5.0$ ms. Normalized integrals (I/I_0) and the natural logarithm of these values are shown by open red circles and filled black circles respectively. Note the bi-exponential behavior of the decay shown by the two distinct slope regimes in the $\ln(I/I_0)$ representation of these data.

5.3.2 Results and discussion

Initial experiments investigated the transverse relaxation of ^{129}Xe in a single pore with a 12 mm pore length created by the inner diameter of the glass cell. A benefit of the gaseous experiments was that changing the gas pressure alters the diffusion coefficient of the gas permitting a straightforward probe into the diffusion behavior. Data showing the functional relationship between the transverse relaxation and the pressure is presented in Figure 5.3 using a mixture of 25% xenon - 75% nitrogen with $\tau = 5.0$ ms, 6.0 ms, and 8.0 ms in the broad linewidth system. At least four data points were taken at each pressure for all τ times. Note that the data was not averaged and all data points are shown but generally overlay one another indicating the exceptional reproducibility of this experiment.

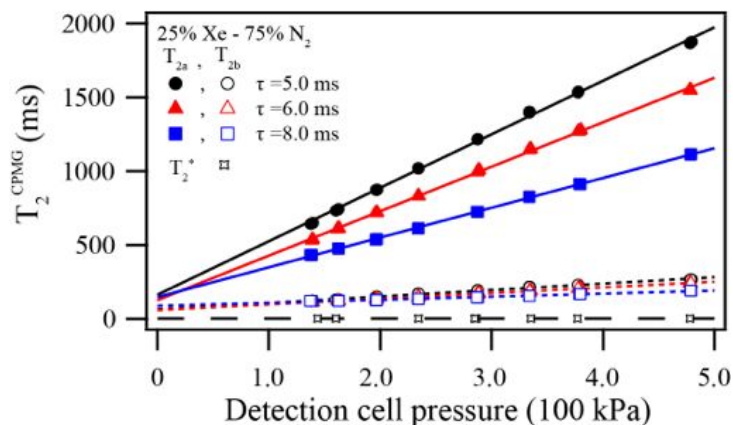


Figure 5.3. Transverse relaxation time (T_2^{CPMG}) of ^{129}Xe as a function of detection cell pressure in the empty glass detection cell that acted as a single pore for diffusion. Data collected using a 25% xenon – 75% nitrogen mixture for $\tau = 5.0$, 6.0 and 8.0 ms in the broad linewidth system. T_{2a} and T_{2b} were extrapolated from the integral of the CPMG echoes using Eq. 5.9. Parameters from the linear fit of these data are presented in Table 5.2.

In Figure 5.3 it was observed that both T_{2a} and T_{2b} had near linear behavior on the investigated pressure range (~140 - 490 kPa) as highlighted by the linear regression analysis of the data (refer to Table 5.2 for values). The linear dependence on pressure suggested that the intrinsic transverse relaxation was small compared to the transverse relaxation caused from diffusion in the external magnetic field gradient as described in Eq. 5.3. T_{2a} was strongly dependent on the pressure of the gas during the CPMG acquisition having a slope 8-10 times larger than the corresponding T_{2b} .

A possible reason for the bi-exponential behavior was that two different regimes were being probed during the experiment. The shortest characteristic length determines diffusion regime as discussed in the *section* 5.2 and shown in Figure 5.1. The first regime was possibly the free diffusion of the gas. The diffusion coefficient was calculated using Eq. 5.8 for a binary mixture of xenon and molecular nitrogen and then inserted into the equation $l_D = \sqrt{D_0 t}$ to determine diffusion length. Using the $\tau = 5$ ms data as an example, at the highest pressure l_D was 0.16 mm between echoes (2τ) and 2.0 mm over the course of the measurements (164 echoes separated by 2τ), while at the lowest pressure l_D was 0.29 mm between echoes and 3.8 mm over the course of the CPMG sequence. If the entire glass cell was considered the pore in this system then $l_s = 12$ mm (inner diameter of the glass cell) indicating that the system was not in the motional averaging regime since $l_D < l_s$. To determine the dephasing length, l_G , the gradient can be calculated using the relation $1/T_2^* = 1/T_2 + 1/T_2^t$ where the transverse relaxation rate due to magnetic field inhomogeneities ($1/T_2^t$) can be

described by $\gamma\Delta B$ assuming the lineshape is Lorentzian [26]. To calculate ΔB the intrinsic transverse relaxation time, T_2 , was approximated as $T_2 = T_2^{CPMG}$ at the highest-pressure value where diffusion was the most restricted due to collisions with surrounding molecules. If it is assumed that the gradient across the sample is linear along the length of the pore, $l_s = 12$ mm then is approximated by $\Delta B/l_s = 58 \pm 2$ $\mu\text{T/m}$. Consequently the dephasing length, l_G , is 0.45 mm using the relation $l_G = \sqrt[3]{D_{1,2}/\gamma G}$ making l_D/l_G equal to 0.36 and 0.64 at high and low pressure respectively, when using the length the gas diffuses between successive echoes. The characteristic length scales indicated that the system was predominately in the free diffusion regime. However, it is possible that because l_D and l_G are close in value that localization makes a significant contribution to the overall behavior.

In the localization regime, edge effects often reduce transverse relaxation nearer to the walls due to a partial restriction to the diffusion [27]. However, the pore boundary may also produce internal magnetic field gradients increasing transverse relaxation in close proximity to the boundary. The fitting parameter A in Eq. 5.9 helped determined the origins of the diffusion caused transverse relaxation in the bi-exponential CPMG results. In the case where diffusion of the gas was kept to a minimum (i.e. high pressure and short τ) the fitting parameter A showed that the contribution of T_{2b} was the least. As greater diffusion distances were present (i.e. lower pressure and longer τ times) the contribution of T_{2b} increased suggesting that larger proportion of gas experienced the pore boundary.

Table 5.2. Results from the linear regression analysis of T_2^{CPMG} in a single pore as a function of pressure. Data extrapolated from Figure 5.3 – 5.5.

Mixture	τ (ms)	Range of A	T_{2a}		T_{2b}	
			Intercept (ms)	Slope (ms/100 kPa)	Intercept (ms)	Slope (ms/100 kPa)
^ABroad linewidth system						
25% Xe -	5	0.33 ^{C,D}	162 ± 8	362 ± 4	65 ± 3	44 ± 1
75% N ₂	6	0.36 ^C -0.35 ^D	128 ± 5	301 ± 4	59 ± 2	38 ± 1
	8	0.50 ^C -0.38 ^D	147 ± 9	202 ± 12	88 ± 8	21 ± 2
		$T_2^* = 3.05 \pm 0.08$ ms ^E				
25% Xe - 10% N ₂ - 65% He	5	0.34 ^C -0.33 ^D	98 ± 3	248 ± 4	58 ± 2	29 ± 2
		$T_2^* = 3.06 \pm 0.08$ ms ^E				
^BNarrow linewidth system						
25% Xe -	8	0.25	517 ± 13	1016 ± 8	78 ± 6	89 ± 3
75% N ₂	10	0.25 ^C -0.26 ^D	396 ± 13	973 ± 9	105 ± 3	71 ± 2
		$T_2^* = 83.9 \pm 0.7$ ms ^E				

^ABroad linewidth data were collected with the sample without room temperature shimming.

^BNarrow linewidth data were collected with room temperature shimming that improved magnet field homogeneity.

^CA at lowest pressure.

^DA at highest pressure.

^E T_2^* was determined from the full width at half maximum of the one-dimensional spectrum. No pressure dependence of T_2^* was observed.

The qualitative trend of the T_{2a} dependence on τ appeared logical when considering Eq. 5.3 where longer τ results in greater diffusion that therefore reduced T_2^{CPMG} time. However, the actual dependence on the echo time appeared not to follow the τ^2 behavior suggested in Eq. 5.3. This possibly occurred because of the regime changes along with the τ change or due to localized magnetic field differences [28].

Data presented in Figure 5.4 were collected using room temperature shimming to improve magnetic field inhomogeneities and facilitate a narrow peak linewidth. The improved homogeneity in the magnetic field greatly increased the T_2^* time by approximately a factor of thirty over the broad peak system. The greater T_{2a} times were clearly from the reduced gradient, G , because the diffusion coefficient is maintained between data in Figures 5.3 and 5.4. Interestingly, although T_{2a} increased drastically with the

improved shimming while T_{2b} was only slightly changed. This outcome supported the argument that T_{2b} was caused from internal magnet field gradients at the glass cell wall because these were inherent to the sample.

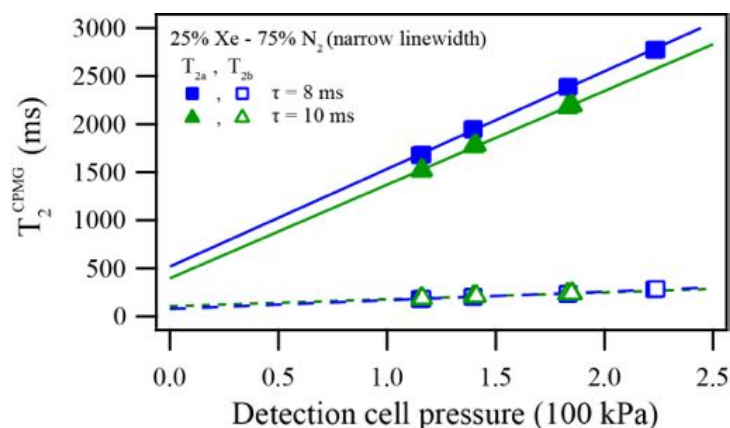


Figure 5.4. ^{129}Xe transverse relaxation time (T_2^{CPMG}) as a function of detection cell pressure during the CPMG sequence with room temperature shimming to make a narrow peak linewidth. T_{2a} and T_{2b} were extrapolated from the integral of the CPMG echoes using Eq. 5.9. Parameters extrapolated from the linear fit of these data are presented in Table 5.2.

Figure 5.5 compares the binary xenon - nitrogen mixture (25% xenon - 75% nitrogen) to one composed primarily of helium (25% xenon - 11% nitrogen - 64% helium). It was observed that T_2^{CPMG} was shorter for the helium containing mixture because helium has a smaller mass, reduced collisional diameter and less interatomic attraction than the diatomic nitrogen it replaced ($m_{\text{He}}/m_{\text{N}_2} = 0.14$, $\sigma_{\text{He}}/\sigma_{\text{N}_2} = 0.70$, $\epsilon^{\text{He}}/\epsilon^{\text{N}_2} = 0.11$), resulting in greater xenon diffusion in agreement with Eq. 5.3. In calculations the ternary mixture was treated as a binary mixture of xenon and helium for simplicity and assumed that the small percentage of nitrogen

did not drastically alter diffusion. At the highest pressure l_D of this mixture was calculated as 0.33 mm between echoes (2τ) and 4.3 mm over the course of the measurements (164 echoes separated by 2τ) approximately twice the diffusion length for the binary xenon and nitrogen mixture. For transverse relaxation studies in the lung, the pressure is not an adjustable variable (i.e. must remain ambient pressure); however, the alterations to the partial pressures of gases in the mixture effect the overall transverse relaxation. Future experiments can be tailored to some degree for specific diffusion lengths as necessary.

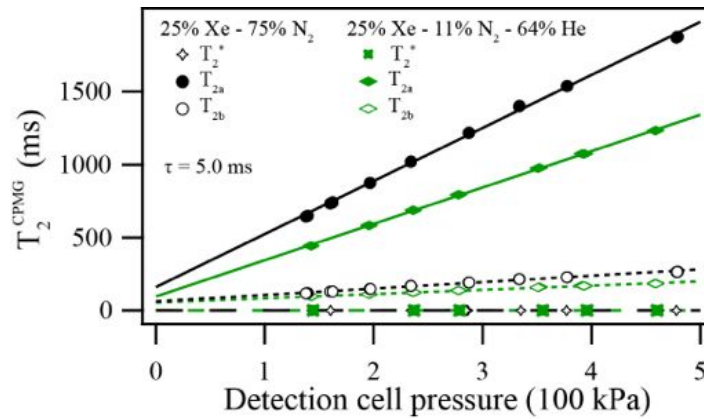


Figure 5.5. ^{129}Xe transverse relaxation time (T_2^{CPMG}) as a function of detection cell pressure during the CPMG sequence for binary (25% xenon – 75% nitrogen) and ternary (25% xenon - 11% nitrogen – 64% helium) gas mixtures with $\tau = 5.0$ ms in the broad linewidth system. T_{2a} and T_{2b} were extrapolated from the integrals of the CPMG echoes using Eq. 5.9. Parameters extrapolated from the linear fit of these data are presented in Table 5.2.

The design of the experiments permitted the determination of internal gradients using Eq. 5.3 by substituting Eq. 5.8 for the diffusion of the sample, making $1/T_2^{\text{CPMG}}$ behave linearly with $1/P$ (the inverse of the pressure) following:

$$1/T_2^{CPMG} = 1/T_2 + 88.76 \sqrt{\frac{T^3 (M_1 + M_2)}{2M_1M_2}} \frac{\gamma^2 G^2 \tau^2}{\sigma_{1,2}^2 \Omega_{1,2}} \cdot \frac{1}{P}. \quad (5.10)$$

Figure 5.6 compares the $1/T_2^{CPMG}$ the $\tau = 5.0$ ms of the broad linewidth data from Figure 5.3 with the $\tau = 8.0$ ms data from the narrow linewidth system from Figure 5.4. Results from the linear regression analysis are presented in Table 5.3.

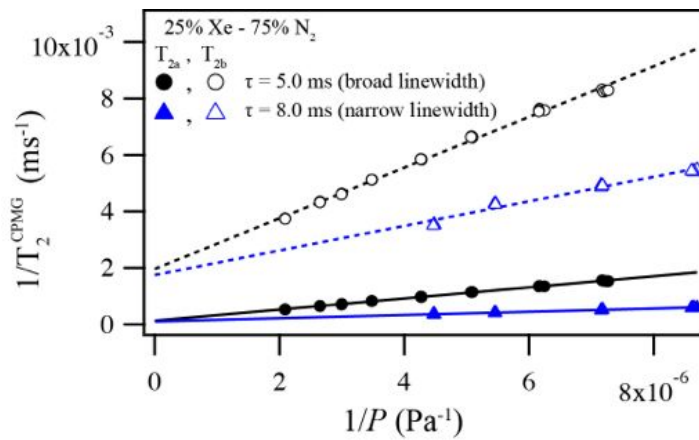


Figure 5.6. ^{129}Xe CPMG transverse relaxation rate ($1/T_2^{CPMG}$) as a function of $1/P$ for the 25% xenon – 75% nitrogen mixture. Comparison between the broad linewidth system with $\tau = 5.0$ ms and the narrow linewidth system with $\tau = 8.0$ ms. Parameters from the linear regression analysis of these data and the corresponding magnetic field gradients are presented in Table 5.3.

Determination of the magnetic field gradient found that, in the broad linewidth system, both T_{2a} and T_{2b} had a magnetic field gradient three times larger than the narrow linewidth system (refer to Table 5.3 for values). The gradient calculated from the slope from the linear regression analysis of Figure 5.6 was larger than the value calculated using T_2^* by nearly an order of magnitude. The disagreement possibly originated from a complication in the treatment of τ . As discussed earlier in this section the data did not

possesses a quadratic dependence on τ contrary to the equation of Torrey presented in Eq. 5.3. The discrepancy may contribute to errors in the calculation of the gradient. Previous work observed a linear, not quadratic, dependence on τ due to the local inhomogeneities in the magnetic field [28]. In Eq. 5.10, if τ in place of τ^2 squared were used in the calculation of the gradient from the slope, resulting value would decrease. The uncertainty in the τ dependence warrants additional investigation in future studies.

Table 5.3. Determination of internal magnetic field gradients in a single pore. Data extracted from Figure 5.6 using linear regression analysis of the relaxation rate ($1/T_2^{CPMG}$) as a function of $1/P$.

MR system	τ (ms)	T_2^* (ms)	$1/T_{2a}$ Slope (ms ⁻¹ /Pa ⁻¹)	$1/T_{2b}$ Slope (ms ⁻¹ /Pa ⁻¹)	From T_2^* ^C	G (μ T/m) From T_{2a}	From T_{2b}
^A Narrow linewidth	8.0	83.9±0.7	56.1±0.2	434±20	2.1±0.1	51±1	140±10
^B Broad linewidth	5.0	3.05±0.08	198±1	896±10	58±2	152±2	430±10

^ANarrow linewidth data were collected incorporating room temperature shimming that improved magnet homogeneity. The linear regression analysis results in intercepts of $1.11±0.02 \times 10^{-4}$ ms⁻¹ and $17.5±1.4 \times 10^{-4}$ ms⁻¹ for $1/T_{2a}$ and $1/T_{2b}$ respectively.

^BBroad linewidth data were collected without room temperature shimming. The linear regression analysis results in intercepts of $1.28±0.05 \times 10^{-4}$ ms⁻¹ and $19.6±0.4 \times 10^{-4}$ ms⁻¹ for $1/T_{2a}$ and $1/T_{2b}$ respectively.

^CThe gradient over the length of the pore $l_s = 12$ mm calculated from the relation: $1/T_2^* = 1/T_2 + 1/T_2^t$, where $1/T_2 = 1/T_2^{CPMG}$ and $1/T_2^t = \gamma\Delta B$.

5.4 Transverse relaxation of ¹²⁹Xe and ⁸³Kr in porous media

5.4.1 Materials and methods

5.4.1.1 ¹²⁹Xe spin exchange optical pumping

Spin exchange optical pumping (SEOP) of ¹²⁹Xe and ⁸³Kr was completed as described in Chapter 3. Steady state polarization of ¹²⁹Xe (6 minute SEOP time) was used to overcome the limited signal due to gas displacement by the glass beads. For ⁸³Kr a near steady state polarization

SEOP time of 8 minutes produced sufficient signal intensity while maintaining an acceptable data collection rate.

5.4.1.2 Preparation of glass beads

Model porous systems of spherical glass beads (BioSpec Products Inc.; Bartlesville, OK, USA) with diameters of 0.5 mm and 1.0 mm were used to investigate transverse relaxation with restricted diffusion. An acrylic detection cell (14.1 mm ID) with a screw cap to enable removal and addition of beads was constructed for the sample container. It was assumed that when inserted into the acrylic detection cell the beads arranged into the closest packing of spheres with the resulting tetrahedral and octahedral holes, of radii 22.3% and 41.4% of the radius of the glass beads, as the pores for restricted diffusion. The cell reached above and below the detection region of the NMR probe to aid with the homogenous packing of the beads through the detection entire region.

Untreated beads (*fresh* beads directly from suppliers) were prepared for the CPMG experiments by placing into the acrylic detection cell and put under vacuum conditions (pressure < 0.1 kPa) for a minimum of 30 minutes before running experiments. In addition to the untreated beads, quantities of both sized glass beads were siloxane treated to coat the surface of the beads to determine the effect of surface chemistry on the transverse relaxation.

Preparation of the siloxane treated beads required washing using potassium hydroxide dissolved in ethanol (pH > 13) for 24 hours to thoroughly clean the surface of the glass. The beads were then rinsed with distilled water until pH equilibration indicated complete removal of the

basic solution. A vacuum oven dried the beads at 110°C for over 20 hours to dehydrate the surface. The beads were then washed in a 1:10 solution of SurfaSil™ (Thermo Fisher Scientific Inc. Waltham, MA, USA) in toluene and rinsed with ethanol. After a second drying in the vacuum oven, the beads were stored in a gas tight container with 200 kPa dry nitrogen until used in experiments.

5.4.1.3 Animal care and preparation

To assist with the design of future experiments, this work investigated the transverse relaxation in *ex vivo* lungs to measure T_2^{CPMG} . Healthy male Sprague-Dawley rats (350 - 400 g, Charles River UK Ltd, Margate, UK) were euthanized by an overdose of pentobarbital (Sigma-Aldrich Ltd, Gillingham, UK) in accordance with local animal welfare guidelines and A(SP)A 1986 (Animals for Scientific Procedures Act 1986). After death a catheter was inserted into the caudal vena cava and blood was flushed from the heart and pulmonary system with 20 – 30 cm³ heparin 100 IU/cm³ (Wockhardt UK Ltd, Wrexham, UK) in 0.9% saline solution (Baxter Healthcare Ltd, Thetford, UK) followed by phosphate buffer solution (PBS, Sigma-Aldrich Ltd, Gillingham, UK). A PTFE adapter tube was inserted 5 - 10 mm above the carina and sutured into place. The heart and lungs were removed from the animal and suspended trachea downward in an acrylic ventilation chamber in a 5% glucose solution (weight/volume). For additional details refer to the description and diagrams in Chapter 4 and ref. [29].

5.4.1.4 CPMG experiments

The transverse relaxation of ^{129}Xe and ^{83}Kr was measured in a 9.4 T superconducting magnet by means of a CPMG sequence on a Kea 2 spectrometer. In the glass bead experiments, the acrylic sample cell containing the beads was kept at 290 – 292 K while situated in the superconducting magnet. Hyperpolarized noble gas mixture was transferred into a pre-evacuated detection cell via pressure equalization and allowed to pressure and temperature to equilibrate in the cell for a few seconds before triggering the CPMG pulse sequence. At various pressures, a simple one-pulse experiment acquired a one-dimensional spectrum to determine T_2^* from the FWHM. An example result from a CPMG sequence is shown in Figure 5.7. Relaxation measurements taken in the *ex vivo* rat lungs used a modified CPMG sequence on a Bruker Avance III system using the hyperpolarized ^{83}Kr and ^{129}Xe delivery technique described in Chapter 4.

5.4.1.5 Data analysis

Contrary to the single pore data the relaxation in the beads did not show substantial bi-exponential behavior. The CPMG decay of ^{129}Xe signal from a $\tau = 0.375$ ms, 1865 kPa in the 0.5 mm glass beads is displayed in Figure 5.7. Since no bi-exponential behavior was observed the T_2^{CPMG} value was extrapolated using:

$$I/I_0 = \text{int} + A \cdot \exp\left(-t/T_2^{\text{CPMG}}\right). \quad (5.11)$$

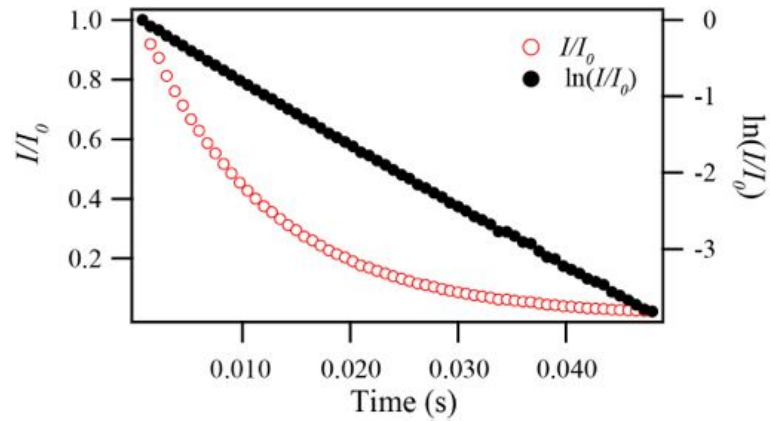


Figure 5.7. Example CPMG result in 0.5 mm untreated glass beads collected using 186.5 kPa of a 25% xenon – 10% nitrogen – 65% helium mixture with $\tau = 0.375$ ms. Normalized integrals (I/I_0) of the echo train are shown by open red circles. The natural logarithm of the normalized integrals ($\ln(I/I_0)$) are shown by filled black circles. Note the bi-exponential behavior observed in the empty glass cell was not apparent in the beads as shown by the single slope in the $\ln(I/I_0)$ representation of these data.

5.4.2 Results and discussion

5.4.2.1 Transverse relaxation of ^{129}Xe in glass beads

The experiments in this section investigated the transverse relaxation of ^{129}Xe arising from diffusion of the gas in a model porous system of spherical glass beads with the intention of determining the internal magnetic field gradients in the sample. To probe the diffusion behavior of ^{129}Xe in the porous system, data were collected investigating the relationship between the measured T_2^{CPMG} value and the pressure of the gas mixture in an acrylic cell containing the glass beads. These experiments were modelled after the single pore experiments described in *section 5.3.2*. T_2^{CPMG} was extrapolated from individual CPMG experiments using Eq. 5.11. Figure 5.8 displays T_2^{CPMG} of ^{129}Xe in 1.0 mm glass beads at various gas pressures in the sample cell during detection. Data from pressures greater than 50 kPa showed a

linear dependence of T_2^{CPMG} on the gas pressure, similar to the result from the single pore.

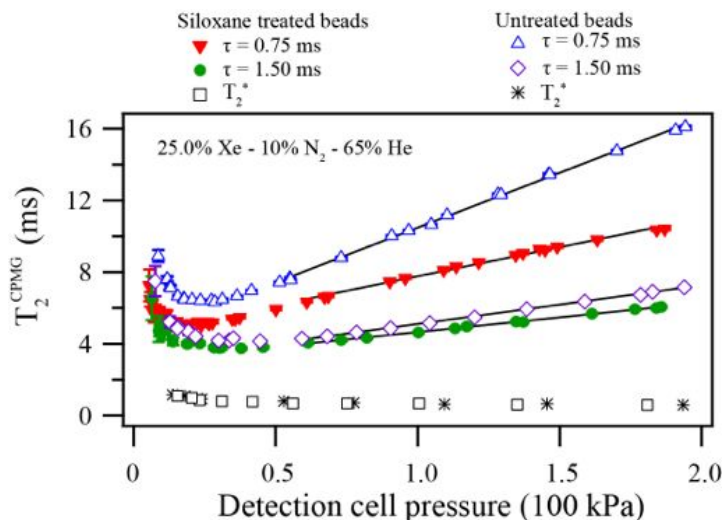


Figure 5.8. T_2^{CPMG} of ^{129}Xe as a function of the gas pressure in the acrylic detection cell containing 1.0 mm glass beads using a 25% xenon – 10% nitrogen – 65% helium gas mixture. Plotted lines are included solely to highlight linearity of data.

The results were particularly interesting for pressures less than 50 kPa where the T_2^{CPMG} time increased. The complete change in behavior indicated a change of the diffusion regime that may be explained by characteristic length scales. At 25 kPa the diffusion length, l_D , was 0.6 mm (2τ) between echoes and 4.5 mm over the entire experiment (64 echoes space by 2τ). It was likely that the system was in the motional averaging regime since the 1.0 mm beads contained pores of only 0.22 mm and 0.41 mm, for tetrahedral and octahedral holes respectively (see *Preparation of glass beads* in section 5.4.1). As the pressure was reduced further from this point an increase in motional averaging occurred and the gradient that the gas experienced was averaged out whereby increasing T_2^{CPMG} .

To test this theory, the transverse relaxation of ^{129}Xe in 0.5 mm diameter glass beads was measured with results presented in Figure 5.9. Theoretically the smaller beads should make motional averaging more prevalent because the reduction in pore size. Tetrahedral pores are 0.11 and the octahedral pores 0.21 mm in the 0.5 mm beads, while the diffusion length remained the same as the experiments for the 1 mm beads. In Figure 5.9 it is apparent that the minimum T_2^{CPMG} value occurs at a higher pressure than the 1.0 mm glass beads in agreement with the proposed explanation. At low pressures the increase in T_2^{CPMG} was more substantial for the 0.5 mm beads than the 1.0 mm beads. Data revealed insignificant differences between surface treatments of the glass beads indicating that the magnetic field gradients were not affected by the surface coating. In future studies these results may have importance in using pulmonary magnetic resonance imaging where the small pore size of alveoli would result in the motional averaging regime. This means that using a mixture containing substantial amounts of helium may be beneficial because it actually increases T_2^{CPMG} due to greater motional average from the increased diffusion length.

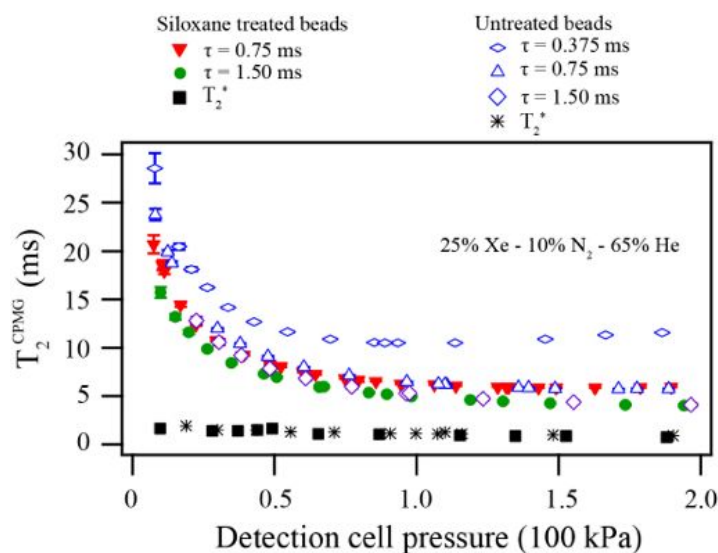


Figure 5.9. T_2^{CPMG} of ^{129}Xe as a function of the gas pressure in the acrylic detection cell containing 0.5 mm glass beads using a 25% xenon – 10% nitrogen – 65% helium gas mixture.

To demonstrate the robust nature and reproducibility of the transverse relaxation measurements, the glass beads were removed from the acrylic sample cell and re-inserted into the cell at a later date for repeated CPMG experiments (see Figure 5.10 for repeated data). The siloxane treated beads were removed then replaced into the acrylic cell while a completely different sample untreated beads of like dimensions were used for repeated experiments. The repeated data for both treated and untreated glass beads show strong agreement to original data.

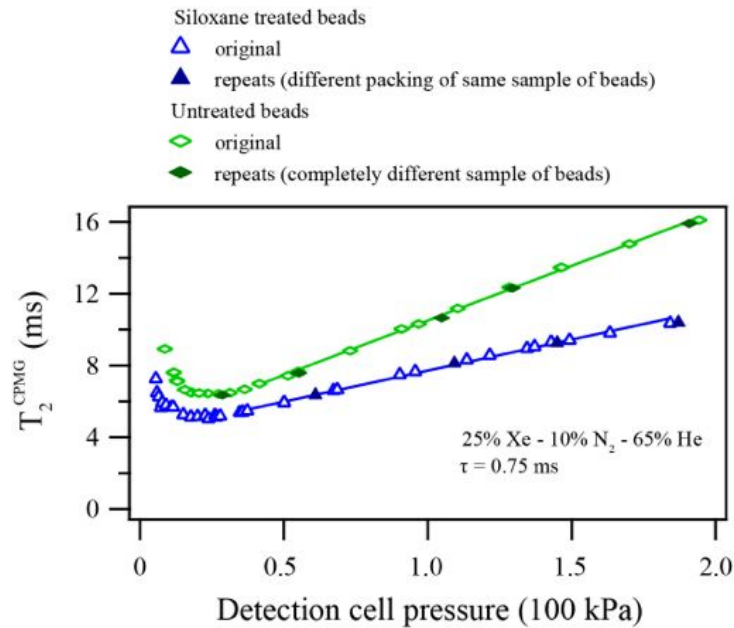


Figure 5.10. Repeat data for T_2^{CPMG} of ^{129}Xe as a function of the gas pressure in the acrylic detection cell containing 1.0 mm glass beads using a 25% xenon – 10% nitrogen – 65% helium gas mixture. The repeats (filled icons) showed that the experiments were very robust and reproducible. Lines are included solely to highlight linearity of data.

Internal gradients in the glass beads were determined following the method described for the single pore (empty glass cell) experiment. In the case of the 1.0 mm beads and $\tau = 0.75$ ms data for the 25% xenon – 10% nitrogen – 65% helium mixture (from Figure 5.10), the transverse relaxation rate as a function of $1/P$ revealed linear behavior at pressures greater than 100 kPa as shown in Figure 5.11. Using the slope from the linear regression analysis the internal gradient was calculated as 950 ± 20 $\mu\text{T/m}$ and 920 ± 30 $\mu\text{T/m}$, for the siloxane treated and untreated beads respectively, supporting the hypothesis that the surface coating did not alter the internal gradients in the pore. Therefore the transverse relaxation significantly depended on pore size and was predominately insensitive to the surface chemistry of the pore.

This observation was interesting since it contradicted the typically behavior for longitudinal relaxation where chemistry of a surface substantially affects the relaxation [30, 31], for example, relaxation from paramagnetic materials in the surface [32]. The line broadening due to internal magnetic field gradients caused by the glass beads resulted in a very short T_2^* time and a large gradient of $13000 \pm 300 \mu\text{T/m}$ using a pore length of $l_s = 0.22 \text{ mm}$. Unlike the case of the single pore the calculation of the gradient from T_2^* is substantially larger than the value gradient calculated using the data in Figure 5.11. A possible cause for the difference was that the broadening of the peak in the glass beads may have resulted in a non-Lorentzian lineshape whereby making the assumption that $\nu = 1/\pi T_2^*$ invalid. Unfortunately, the ambiguity in the τ dependence makes the origins of this of the difference uncertain (refer to *section 5.3.2* for discussion on τ dependence).

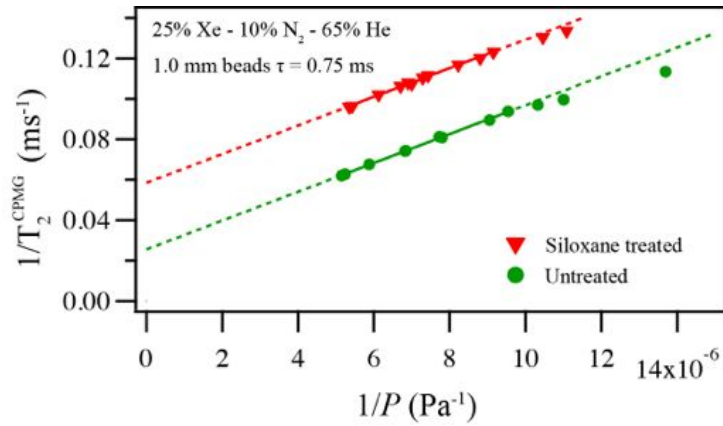


Figure 5.11. $1/T_2^{CPMG}$ of ^{129}Xe as a function of the $1/P$ in the acrylic detection cell containing 1.0 mm glass beads using a 25% xenon – 10% nitrogen – 65% helium gas mixture. Linear regression analysis was performed only on for pressures over 100 kPa (i.e. $1/P < 10^{-5} \text{ Pa}^{-1}$) which was the linear regime of the data. The fitted region is indicated by the solid line while the dashed line is an extension of the linear fitting provided to guide the eye the full length of the graph. Note that data from less than 70 kPa in Figure 5.10 are not included.

Using a gradient of 935 $\mu\text{T/m}$ (average between two surface treatments), the dephasing length (l_G) at 150 kPa for this mixture is 0.43 mm while the diffusion length (l_D) at this pressure was calculated as 0.23 mm between echoes (2τ) making the diffusion length on the order of the size of the pore (0.22 mm and 0.41 mm, for tetrahedral and octahedral pores respectively). However at 15 kPa, where the increase in T_2^{CPMG} was observed, the dephasing length (l_G) was 0.93 mm, assuming that the magnitude of the internal gradient is unchanged at low pressure, while the diffusion length (l_D) is 0.73 mm between echoes (2τ) and the pore size remained 0.22 and 0.41 mm in tetrahedral and octahedral respectively; suggesting motional averaging behavior.

5.4.2.2 *Transverse relaxation of ^{83}Kr in glass beads*

The insensitivity of ^{129}Xe transverse relaxation to the surface coating may have significant implications for future experiments, particularly for work using hyperpolarized ^{83}Kr . ^{83}Kr has shown T_1 contrast to both surface chemistry [33-35] and surface to volume ratio [34] and isolation of the particular origins of the longitudinal relaxation may be difficult. The transverse relaxation on the other hand appears to depend only on pore size and not surface chemistry and may provide a pathway to identify the origin of the longitudinal relaxation.

Experiments investigating the transverse relaxation of ^{83}Kr were completed by Mathieu Baudin while he was an intern at the University of Nottingham. Mr. Baudin determined the transverse relaxation of ^{83}Kr in 1.0 mm untreated glass beads with results shown in Figure 5.12. The T_2^{CPMG} times were significantly longer for ^{83}Kr than ^{129}Xe . This can be explained by the significantly reduced gyromagnetic ratio ($\gamma_{^{83}\text{Kr}}/\gamma_{^{129}\text{Xe}} = 0.139$) that reduces the transverse relaxation rate as described by Eq. 5.3. The increased T_2^{CPMG} permitted a relatively long $\tau = 5.0$ ms in the glass beads.

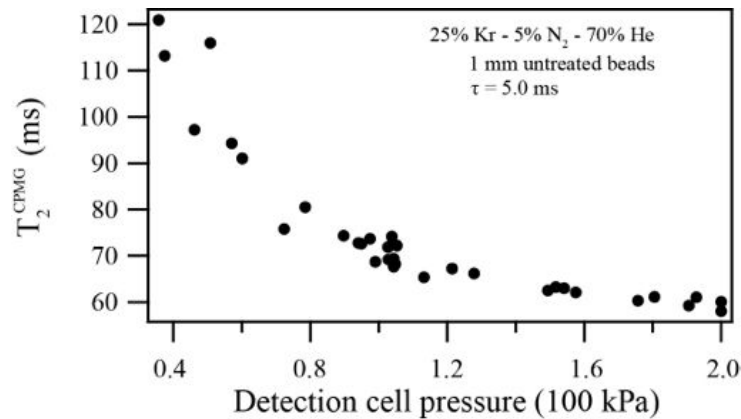


Figure 5.12. T_2^{CPMG} of ^{83}Kr as a function of the gas pressure in the acrylic detection cell containing 1.0 mm glass beads using a 25% krypton – 5% nitrogen – 70% helium gas mixture. Data collected by Mathieu Baudin.

Data for ^{83}Kr in 1.0 mm beads were more similar to the 0.5 mm bead data than the 1.0 mm bead data of ^{129}Xe (i.e. the minimum T_2^{CPMG} value was at a higher pressure). The diffusion coefficient unlikely caused the change in the pressure of the minimum T_2^{CPMG} value between the two isotopes. For instance, at a pressure of 25 kPa the diffusion length for ^{83}Kr was 1.58 mm between echoes (2τ) while the diffusion length for ^{129}Xe was 1.46 mm on the same time scale. More significantly, however, is the fact that ^{83}Kr was much less affected by diffusion through magnetic field gradients than ^{129}Xe , due to the reduced gyromagnetic ratio. The reduction in gyromagnetic ratio allowed the CPMG sequence to use longer τ times and therefore probe larger diffusion lengths. For example, at 25 kPa, the diffusion length (l_D) for ^{83}Kr was 1.58 mm between echoes ($2\tau = 10.0$ ms) while the diffusion length (l_D) was 0.56 mm between echoes ($2\tau = 1.5$ ms) for ^{129}Xe with the parameters described in Figure 5.10.

Assuming that the magnetic field gradient in the untreated 1.0 mm glass bead sample was $920 \pm 30 \mu\text{T/m}$ (determined from ^{129}Xe experiments) the dephasing length (l_G) was calculated for ^{83}Kr and subsequently the diffusion regime was determined. At 150 kPa of krypton in a mixture with helium and diffusion time of $2\tau = 10.0 \text{ ms}$, the characteristic length scales were $l_D = 0.62 \text{ mm}$, $l_G = 0.88 \text{ mm}$, and $l_s = 0.22 \text{ mm}$ and 0.41 mm , in the tetrahedral and octahedral pores, respectively; indicating that the system was in the motional averaging regime even at the relative high pressure. Lower pressures increased both diffusion length (l_D) and the dephasing length (l_G) while the pore size (l_s) remained the same increasing the motional averaging in the system and subsequently T_2^{CPMG} .

5.4.2.3 Transverse relaxation of ^{129}Xe and ^{83}Kr in ex vivo rat lungs

The model porous system of glass beads was chosen with the purpose of approximating the alveolar dimensions of lungs since a single human alveolus has an average diameter of 0.200 mm [36]. In this work the transverse relaxation time of ^{129}Xe and ^{83}Kr was measured in *ex vivo* rat lungs taken from healthy animals using the CPMG experiment. The average Sprague-Dawley rat alveolus diameter is approximately 0.100 mm with a inhalation volume similar to that used in this work [37]. Inhaling 5 ml of a $25\% \text{ xenon} - 75\% \text{ nitrogen}$ mixture with $\tau = 5.0 \text{ ms}$ resulted in a ^{129}Xe T_2^{CPMG} of $32.9 \pm 0.5 \text{ ms}$ (see Figure 5.13 blue icons). Inhaling 8 ml of a $25\% \text{ krypton} - 75\% \text{ molecular nitrogen}$ mixture and using $\tau = 5.0 \text{ ms}$ resulted in an ^{83}Kr T_2^{CPMG} of $166 \pm 11 \text{ ms}$ (see Figure 5.13 green icon). Corresponding T_2^* in the *ex vivo* rat lungs conditions were $1.77 \pm 0.37 \text{ ms}$ and $13.1 \pm 0.8 \text{ ms}$ for ^{129}Xe and ^{83}Kr respectively.

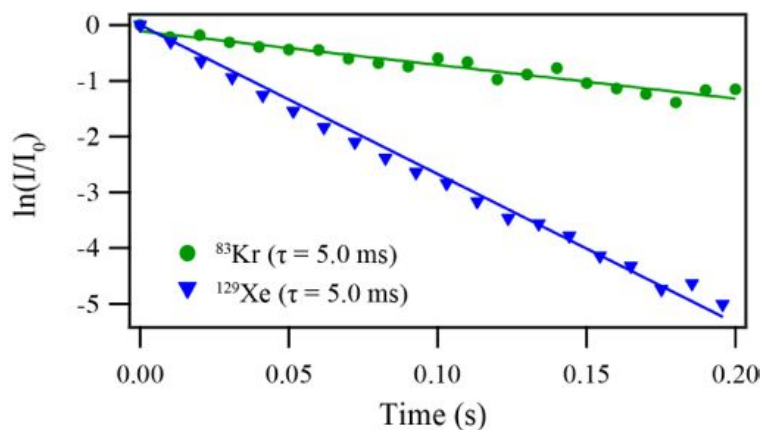


Figure 5.13. Semi-logarithmic plot of I/I_0 of the CPMG echoes for both ^{129}Xe and ^{83}Kr in *ex vivo* rat lungs. A 25% xenon – 75% nitrogen mixture and $\tau = 5$ ms resulted in a T_2^{CPMG} of 32.9 ± 0.5 ms for ^{129}Xe (blue triangles). A 25% krypton – 75% nitrogen mixture and $\tau = 5.0$ ms resulted in a T_2^{CPMG} of 166 ± 11 ms for ^{83}Kr (green circles).

5.5 Conclusions

This study investigated the transverse relaxation of gaseous ^{129}Xe and ^{83}Kr caused by diffusion through internally generated magnetic field gradients. A single pore was probed using an empty glass cell having 12 mm inner diameter. Two definite cases of relaxation were seen in the single pore system as observed by bi-exponential signal attenuation during the CPMG sequence. One component of the bi-exponential decay came from the free diffusion of the gas near the center of the glass cell while the second component likely came from the gas localized in close proximity to the boundary of the pore where internal magnetic field gradients caused increased relaxation. A linear dependence of T_2^{CPMG} on the gas pressure during the CPMG sequence signified that the intrinsic transverse relaxation was small compared to the transverse relaxation caused by diffusion.

A model porous system of glass beads enabled restricted diffusion of the gas in the tetrahedral and octahedral pores formed from the closest packing of spheres. Mono-exponential decay of the signal intensity was observed in contrast to the bi-exponential result in the empty glass cell. This was likely because all the gas was in close proximity to the glass surface and experienced similar internal magnetic field gradients opposed to the mixture of localization and free diffusion regimes observed in the single pore. The data revealed a linear dependence of T_2^{CPMG} at relatively high pressures; however, the behavior at sufficiently low pressure deviated from the linear relationship. Data suggests that the deviation from linearity was caused from a transition to the motional averaging regime as observed by an increase in the T_2^{CPMG} time continually lower pressures.

Transverse relaxation measurements of ^{83}Kr resulted in 5 – 7 times longer T_2^{CPMG} and T_2^* times than for ^{129}Xe in comparable experiments caused by the reduced gyromagnetic ratio of the isotope. As with ^{129}Xe , ^{83}Kr also showed the increase in T_2^{CPMG} in the case of restricted diffusion when pressure was reduced. In fact the increase was more pronounced for ^{83}Kr , occurring at higher pressures than for ^{129}Xe , primarily because longer diffusion lengths were probed using increased τ times. Long τ times were permitted by the low gyromagnetic ratio that made ^{83}Kr relatively insensitive to magnetic field gradients.

Internal magnetic field gradients were quantified exploiting the linear behavior of the transverse relaxation rate as a function of the inverse of the pressure. In the single pore system (*section 5.3.2*) the internal magnetic field gradients calculated from T_2^* were smaller than the values from the linear

relationship of the CPMG transverse relaxation rate with the inverse of the pressure. In the glass bead sample (*section 5.4.2*), the calculated magnetic field gradient was drastically different between the value calculated from T_2^* and from the linear regression analysis of the CPMG transverse relaxation rate as a function of inverse pressure, possibly as a result of non-Lorentzian line broadening. Siloxane treated and untreated 1.0 mm glass beads generated internal magnetic field gradients of $950 \pm 20 \mu\text{T/m}$ and $920 \pm 30 \mu\text{T/m}$, respectively, the pores indicating the surface treatment did not alter the internal gradients of the sample. The insensitivity of transverse relaxation on the surface coating may provide a pathway to determine whether the longitudinal relaxation of ^{83}Kr arises from surface chemistry or pore size.

Unfortunately, the described method only determines internal magnetic field gradients in systems where large changes to the pressure are possible. It may prove beneficial to use the stimulated echo experiment proposed by Song et al. [38] where the diffusion length acts as the independent variable to investigate characteristic of the pore. Future studies of the transverse relaxation of gaseous ^{129}Xe and ^{83}Kr may use the information presented in this work in conjunction with the method of Song and colleagues to quantify the internal magnetic field gradients for isobaric experiments such as studies of the pulmonary system.

As a final remark the long T_2 time of ^{83}Kr due to the low gyromagnetic ratio and subsequently considerable motional averaging of the gradient in the duration of τ for the small pores in *ex vivo* rat lungs (approximately 0.100 mm in the experimental conditions of this work) may have particular

importance by permitting imaging sequences such as echo planar imaging (EPI). EPI may help in future hyperpolarized ^{83}Kr SQUARE MRI where fast T_1 relaxation constrains the fast low-angle shot (FLASH) or variable flip angle (VFA) FLASH techniques that acquire one line of k-space per radio frequency pulse. EPI has the possibility of also increasing the signal intensity by approximately a factor of five since a full $\pi/2$ (90°) pulse can be used to initiate the EPI train in place of the small percentage of magnetization per line of k-space in the VFA FLASH protocol discussed in Chapter 4.

5.6 References

- [1] E.L. Hahn, SPIN ECHOES, *Physical Review*, 80 (1950) 580-594.
- [2] H.Y. Carr, E.M. Purcell, Effects of Diffusion on Free Precession in Nuclear Magnetic Resonance Experiments, *Phys. Rev.*, 94 (1954) 630-638.
- [3] H.C. Torrey, Bloch equations with diffusion terms, *Physical Review*, 104 (1956) 563-565.
- [4] R. Weisskoff, C.S. Zuo, J.L. Boxerman, B.R. Rosen, Microscopic susceptibility variation and transverse relaxation: theory and experiment, *Magn. Reson. Med.*, 31 (1994) 601-610.
- [5] M.S. Katsiotis, J.A. Gomez, M. Fardis, E. Karakosta, G. Diamantopoulos, G. Papavassiliou, NMR and MRI Analysis of Rock Core Samples From Oil Wells, in: *EUROMAR 2013*, Hersonissos, Crete, Greece, 2013.
- [6] Y.-Q. Song, Magnetic Resonance of Porous Media, in: *EUROMAR 2013*, Hersonissos, Crete, Greece, 2013.
- [7] V.D.M. Koroleva, S. Mandal, Y.-Q. Song, M.D. Hurlimann, Broadband CPMG Sequence with Composite Excitation and Short Composite Refocusing Pulses in: *ICMRM 12*, Cambridge, England, United Kingdom, 2013.
- [8] S. Vogt, A.B. Sanderlin, J.D. Seymour, S.L. Codd, Displacement-Relaxation Correlations of Biofilm Growth in Porous Media, in: *ICMRM 12*, Cambridge, England, United Kingdom, 2013.
- [9] R.L. Kleinberg, M.A. Horsfield, Transverse relaxation processes in porous sedimentary rock, *Journal of Magnetic Resonance* (1969), 88 (1990) 9-19.
- [10] M.D. Hurlimann, K.G. Helmer, L.L. Latour, C.H. Sotak, Restricted Diffusion in Sedimentary Rocks. Determination of Surface-Area-to-Volume Ratio and Surface Relaxivity, *Journal of Magnetic Resonance, Series A*, 111 (1994) 169-178.
- [11] G. Goelman, M.G. Prammer, The CPMG Pulse Sequence in Strong Magnetic Field Gradients with Applications to Oil-Well Logging, *Journal of Magnetic Resonance, Series A*, 113 (1995) 11-18.
- [12] G.H. Sorland, H.W. Anthonsen, J.G. Seland, F. Antonsen, H.C. Wideroe, J. Krane, Exploring the separate NMR responses from crude oil and water in rock cores, *Appl. Magn. Reson.*, 26 (2004) 417-425.
- [13] J.G. Seland, K.E. Washburn, H.W. Anthonsen, J. Krane, Correlations between diffusion, internal magnetic field gradients, and transverse relaxation in porous systems containing oil and water, *Physical Review E*, 70 (2004) 051305.
- [14] R.W. Mair, D.G. Cory, S. Peled, C.-H. Tseng, S. Patz, R.L. Walsworth, Pulsed-Field-Gradient Measurements of Time-Dependent Gas Diffusion, *Journal of Magnetic Resonance*, 135 (1998) 478-486.
- [15] R.W. Mair, G.P. Wong, D. Hoffmann, M.D. Hurlimann, S. Patz, L.M. Schwartz, R.L. Walsworth, Probing porous media with gas diffusion NMR, *Phys. Rev. Lett.*, 83 (1999) 3324-3327.

- [16] E. Stejskal, J. Tanner, Spin diffusion measurements: spin echoes in the presence of a time-dependent field gradient, *The journal of chemical physics*, 42 (1965) 288.
- [17] X.J. Chen, H.E. Moller, M.S. Chawla, G.P. Cofer, B. Driehuys, L.W. Hedlund, G.A. Johnson, Spatially resolved measurements of hyperpolarized gas properties in the lung in vivo. Part I: Diffusion coefficient, *Magn. Reson. Med.*, 42 (1999) 721-728.
- [18] H.J. Cho, E.E. Sigmund, Y. Song, Magnetic Resonance Characterization of Porous Media Using Diffusion through Internal Magnetic Fields, *Materials*, 5 (2012) 590-616.
- [19] J.O. Hirschfelder, C.F. Curtiss, R.B. Bird, Kinetic Theory of Dilute Gases, in: *Molecular Theory of Gases and Liquids*, John Wiley and Sons, New York, 1964, pp. 441-513.
- [20] J.O. Hirschfelder, C.F. Curtiss, R.B. Bird, Transport Phenomena of Dilute Gases, in: *Molecular Theory of Gases and Liquids*, John Wiley and Sons, New York, 1964, pp. 514-610.
- [21] J.O. Hirschfelder, C.F. Curtiss, R.B. Bird, Transport Phenomena of Dilute Gases: The Coefficient of Diffusion, in: *Molecular Theory of Gases and Liquids*, John Wiley and Sons, New York, 1964, pp. 581.
- [22] J.O. Hirschfelder, C.F. Curtiss, R.B. Bird, *Molecular Theory of Gases and Liquids*, John Wiley and Sons, New York, 1964.
- [23] T.R. Marrero, E.A. Mason, Gaseous Diffusion Coefficients, *Journal of Physical and Chemical Reference Data*, 1 (1972) 3-118.
- [24] M.D. Hurlimann, K.G. Helmer, T.M. Deswiet, P.N. Sen, Spin echoes in a constant gradient and in the presence of simple restriction, *Journal of Magnetic Resonance Series A*, 113 (1995) 260-264.
- [25] P.T. Callaghan, *Translational Dynamics & Magnetic Resonance*, Oxford University Press, Oxford, 2011.
- [26] A. Abragam, *The Principles of Nuclear Magnetism*, Oxford University Press, Oxford, UK, 1961.
- [27] P.T. Callaghan, A. Coy, L.C. Forde, C.J. Rofe, Diffusive Relaxation and Edge Enhancement in NMR Microscopy, *Journal of Magnetic Resonance Series A*, 101 (1993) 347-350.
- [28] P. Fantazzini, R.J.S. Brown, Initially linear echo-spacing dependence of $1/T_2$ measurements in many porous media with pore-scale inhomogeneous fields, *Journal of Magnetic Resonance*, 177 (2005) 228-235.
- [29] K.F. Stupic, N.D. Elkins, G.E. Pavlovskaya, J.E. Repine, T. Meersmann, Effects of pulmonary inhalation on hyperpolarized krypton-83 magnetic resonance T-1 relaxation, *Physics in Medicine and Biology*, 56 (2011) 3731-3748.
- [30] W. Heil, H. Humblot, E. Otten, M. Schafer, R. Sarkau, M.I. Leduc, Very long nuclear relaxation times of spin polarized helium 3 in metal coated cells, *Physics Letters A*, 201 (1995) 337-343.
- [31] B. Driehuys, G.D. Cates, W. Happer, Surface Relaxation Mechanisms of Laser-Polarized Xe-129, *Phys. Rev. Lett.*, 74 (1995) 4943-4946.
- [32] R.E. Jacob, B. Driehuys, B. Saam, Fundamental mechanisms of He-3 relaxation on glass, *Chemical Physics Letters*, 370 (2003) 261-267.
- [33] G.E. Pavlovskaya, Z.I. Cleveland, K.F. Stupic, T. Meersmann, Hyperpolarized Krypton-83 as a New Contrast Agent for Magnetic

Resonance Imaging, Proceedings of the National Academy of Sciences of the United States of America, 102 (2005) 18275-18279.

[34] K.F. Stupic, Z.I. Cleveland, G.E. Pavlovskaya, T. Meersmann, Quadrupolar Relaxation of Hyperpolarized Krypton-83 as a Probe for Surfaces, Solid State Nuclear Magnetic Resonance, 29 (2006) 79-84.

[35] Z.I. Cleveland, K.F. Stupic, G.E. Pavlovskaya, J.E. Repine, J.B. Wooten, T. Meersmann, Hyperpolarized ^{83}Kr and ^{129}Xe NMR Relaxation Measurements of Hydrated Surfaces: Implications for Materials Science and Pulmonary Diagnostics, Journal of the American Chemical Society, 129 (2007) 1784-1792.

[36] M. Ochs, J.R. Nyengaard, A. Jung, L. Knudsen, M. Voigt, T. Wahlers, J. Richter, H.J.r.G. Gundersen, The Number of Alveoli in the Human Lung, American Journal of Respiratory and Critical Care Medicine, 169 (2004) 120-124.

[37] R.R. Mercer, J.M. Laco, J. Crapo, Three-dimensional reconstruction of alveoli in the rat lung for pressure-volume relationships, Journal of Applied Physiology, 62 (1987) 1480-1487.

[38] Y.-Q. Song, S. Ryu, P.N. Sen, Determining multiple length scales in rocks, Nature, 406 (2000) 178-181.

Chapter 6: *In situ* MRI of combustion

The method of producing hyperpolarized noble gases presented in Chapter 3 has led to a number of experiments that use hyperpolarized noble gas for purposes other than pulmonary imaging. One such set of experiments has resulted in a peer reviewed publication in the Royal Society of Chemistry journal: Physical Chemistry Chemical Physics entitled *Combustion resistance of the ^{129}Xe hyperpolarized nuclear spin state* [1]. This work was completed by Karl F. Stupic, Joseph S. Six, Michael D. Olsen, Galina E. Pavlovskaya, and Thomas Meersmann. Dr. Stupic performed the initial experiments assessing the feasibility of SEOP with methane fuel that preceded the experiments presented in this work. Dr. Stupic and Mr. Olsen designed and fabricated the combustion probe insert that enabled combustion inside the micro-imaging system. Dr. Pavlovskaya programmed the imaging sequences and also helped edit the paper. Mr. Six conducted the experiments presented in the paper and wrote the paper with Prof. Meersmann.

6.1 Introduction

To date, *in situ* magnetic resonance imaging (MRI) of combustion processes reported in literature is limited to work by Glover et al. [2] although on-going research was recently presented by Pines and co-workers

with focus on demanding hyperpolarized ^{129}Xe flow field measurements [3]. The difficulties of *in situ* MRI of combustion are caused to some extent by the thermal effects on magnetic resonance hardware, however sufficient cooling can usually be applied to study high temperature processes safely [2, 4-6]. More fundamental challenges lie in the very short relaxation times associated with the combustion process due to radical reaction mechanisms, the low spin density in the combustion zone, and the unfavorable Boltzmann equilibrium spin population at the high temperatures of approximately 1700 K for premixed methane - air combustion [7]. These problems were demonstrated by Glover et al. [2] whose ^1H magnetic resonance images show the methane entering the combustion zone but not in the combustion region itself despite the employment of SPRITE [8], an MRI technique that allows for the study of media with short T_1 or T_2^* times and enables magnetic resonance study of fast and turbulent flowing systems. Alternatively, it is possible to use condensation products of combustion for ^1H MRI as reported by Axelson and Wooten [9] and Dufour et al. [10] recently demonstrated *in situ* NMR spectroscopy of pyrolysis products. Although the fuel entering the reaction zone and the combustion exhaust can be observed through the ^1H MRI, the combustion zone itself remains elusive.

The fast relaxation within the combustion processes may also render hyperpolarized molecules useless for these studies, unless a system is chosen that does not radicalize in the combustion process. Using SEOP to generate hyperpolarized ^{129}Xe [11], Anala et al. demonstrated that the hyperpolarized mixture can be added to fuel for usage as a 'spy' in 2D

EXCSY NMR spectroscopy of methane combustion [6]. However, it remained to be shown whether the hyperpolarized state is sustainable throughout the entire combustion process. Since combustion in a stable flame takes place under steady state conditions where ‘location in space’ is closely associated with ‘point in time’ of the reaction, hyperpolarized ^{129}Xe MRI may provide the answer.

6.2 SEOP of fuel-xenon mixtures

It is crucial for the MRI experiments that an uninterrupted constant flow of the fuel - hyperpolarized ^{129}Xe mixture is provided. Continuous flow SEOP is often performed using dilute xenon mixtures containing nitrogen and helium. A high xenon containing mixture can be used in continuous flow but a reduction in polarization results, limiting the benefits of increasing the xenon concentration [12]. Unfortunately, an additional dilution of the hyperpolarized ^{129}Xe occurs when the fuel is added, exacerbating the problem [6]. To reduce the inert gas content the hyperpolarized ^{129}Xe can be accumulated using cryogenic separation [13]. However, the separation process interrupts the supply of gas effectively making a ‘batch mode’ experiment. In this work, instead of adding hyperpolarized ^{129}Xe to a fuel after SEOP, direct SEOP of the fuel-xenon mixture was explored, leading to the batch mode results in Figure 6.1.

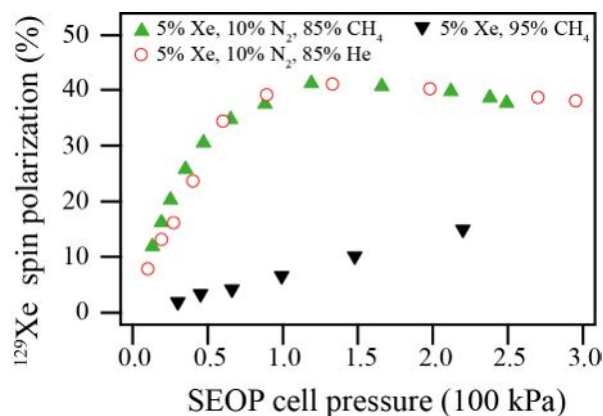


Figure 6.1. ^{129}Xe polarization as a function of SEOP cell pressure for three different gas mixtures (detailed in the legend) in batch mode SEOP. Reproduced from *Phys. Chem. Chem. Phys.*, 15, 2013, 94-7 with permission of the Royal Society of Chemistry.

The very reactive vapor phase rubidium in the SEOP process will not readily react with saturated hydrocarbons such as methane [14]. Figure 6.1 demonstrates the feasibility of batch mode SEOP [15] with a 5% xenon - 95% methane mixture, but the generated spin polarization P stays below 15% and falls short compared to $P > 40\%$ obtained in batch mode SEOP with a xenon – nitrogen – helium mixture. The low polarization and the SEOP pressure dependence of the polarization [15] may be explained by methane's insufficient capability to quench radiation trapping [14, 16], a spin depolarizing process during SEOP [17]. Unlike methane, molecular nitrogen can effectively quench the fluorescence through energy transfer into its vibrational mode [17]. Therefore, the situation can be improved by using a ternary SEOP gas mixture of xenon, methane, and nitrogen. The results with 5% xenon - 10% nitrogen - 85% methane are shown in Figure 6.1 and are nearly identical to the counterpart mixture with helium,

suggesting that methane can replace helium as an SEOP buffer gas, if required.

To gain further insight into the SEOP process the D_2 fluorescence of the rubidium vapor (~ 780 nm) may be monitored. Measurement of the D_2 fluorescence provides an approximation for the D_1 fluorescence which cannot be measured straight forwardly due to the irradiation of the laser light at that wavelength [12]. An optical spectrometer (Ocean Optics HR2000+) measured the D_2 fluorescence at the front of the SEOP cell where laser power density is the greatest as shown in the batch mode apparatus sketched in Figure 6.2.

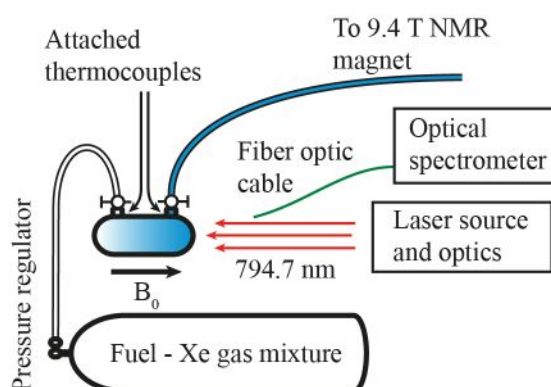


Figure 6.2. Experimental apparatus for batch mode SEOP experiments. The fringe field of the 9.4 T superconducting magnetic used for NMR detection provides the magnetic field parallel to the SEOP cell and circularly polarized laser beam. The optical spectrometer measures the D_2 fluorescence (~ 780 nm) at the front of the SEOP cell via a fiber optic cable.

Hyperpolarization of ^{129}Xe was completed in a borosilicate glass SEOP cell (length = 120 mm, inner diameter = 28 mm) containing ~ 1 g of rubidium. The fringe field of a 9.4 T superconducting magnet supplied a 0.05 T magnetic field (B_0) along the axis of the SEOP cell. The SEOP cell

was positioned in a temperature controlled oven maintaining a measured temperature of 378 ± 6 K at the front of the SEOP cell. It is important to note that although the thermocouples measured the temperature of the glass surface of the SEOP cell the actual temperature conditions inside the cell are unknown. Methods have been developed to determine the actual temperature in the SEOP cell using Raman scattering from the nitrogen quenching gas [18]. To quantitatively describe the behavior of the fluorescence an accurate determination of the SEOP cell temperature is necessary to determine the amount of rubidium in the vapor phase. For this qualitative study of the fluorescence maintaining consistent SEOP cell temperature was sufficient.

A line narrowed (0.25 nm) diode array laser (Comet Module, Spectral Physics, Santa Clara, CA, USA) with polarizing optics provided 23 W of circularly polarized photons resonant with the D_1 transition of rubidium (794.7 nm) for the SEOP process. The propagation of the laser beam was aligned parallel to the external magnetic field B_0 . Polarization measurements utilized 6 minutes of SEOP before shuttling hyperpolarized gas to an evacuated borosilicate detection cell in a 9.4 T superconducting magnet via pressure equalization. NMR experiments were performed using a Magritek Kea 2 spectrometer with custom-built probe tuned to the resonance frequency of ^{129}Xe at 9.4 T (110.56 MHz). Polarization was determined by comparison of the signal enhancement over a thermally polarized sample of xenon at room temperature (~ 295 K) as described elsewhere [19].

Fluorescence measurements were acquired after 3 minutes at each SEOP cell pressure. Data points consist of four averaged measurements presented with the standard deviation. To account for variations in position of the fiber optic between SEOP cells the fluorescence was normalized to the fluorescence observed under SEOP with a 5% xenon – 10% nitrogen – 85% helium standard mixture at 50 kPa.

To circumvent the need for nitrogen in the SEOP mixture, the use of a fuel that quenches radiation trapping would be beneficial. Hydrogen could be used as an alternative to methane in binary SEOP mixture for combustion studies. The use of hydrogen has been proposed to quench radiation trapping in hyperpolarized noble gas experiments [20], however, data confirming the feasibility of using hydrogen as a radiation quenching agent for SEOP of noble gases are limited to studies by Volk et al. [21] early in the field of hyperpolarized noble gases. The achievable polarization of ^{129}Xe using current polarization techniques remains unknown.

Hydrogen has a larger quenching cross section than methane making it significantly more efficient at quenching radiation trapping when compared to methane [14]. Therefore, using hydrogen to quench radiation trapping during SEOP achieves improves spin polarization when replacing methane in binary mixtures as seen in Figure 6.3.

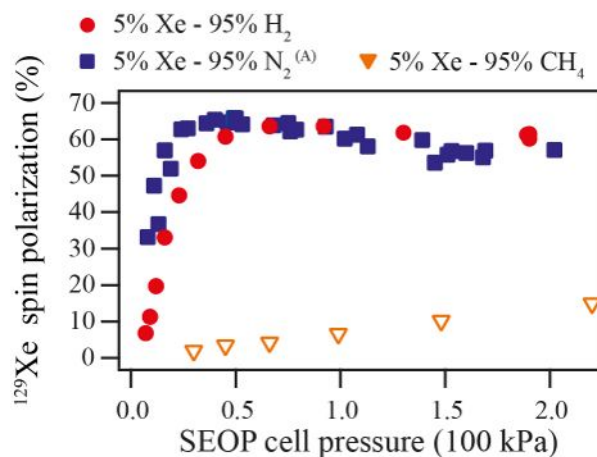


Figure 6.3. ^{129}Xe spin polarization as a function SEOP cell pressure for three mixtures containing different gases to quench radiation trapping. See legend for icon explanation of gas mixtures. ^(A) Spin polarization data taken from ref. [19]. Note that the polarization found when using hydrogen to quench radiation trapping is similar to nitrogen data from a similar experiment.

In Figure 6.3 the data of the hydrogen – xenon mixture are compared to mixtures containing nitrogen (taken from ref. [19]) or methane to quench radiation trapping. When compared to the methane – xenon mixture it is evident that the ^{129}Xe spin polarization is much improved when using hydrogen to quench radiation trapping. The achieved polarizations using the hydrogen – xenon were remarkably high reaching values similar to the nitrogen – xenon mixture at SEOP cell pressure greater than 100 kPa. The degree of the similarity was not anticipated since the spin exchange cross section for collisions between the rubidium and hydrogen atoms are efficient at depolarizing the electronic polarized rubidium [22]. It is important to note that the spin polarization values have small variations between different SEOP cells [19] and the resemblance between the two curves should not be over interpreted. Nevertheless, the 60% ^{129}Xe spin

polarization that is attained using batch mode SEOP with hydrogen to quench radiation trapping is desirable.

An explanation for the deviation between the nitrogen – xenon mixture and hydrogen – xenon mixture below 100 kPa SEOP cell pressure is seen in the effective cross-section to quench radiation trapping of $58 \pm 12 \text{ \AA}^2$ for nitrogen and $6 \pm 2 \text{ \AA}^2$ for hydrogen while $<1 \text{ \AA}^2$ for methane [14].

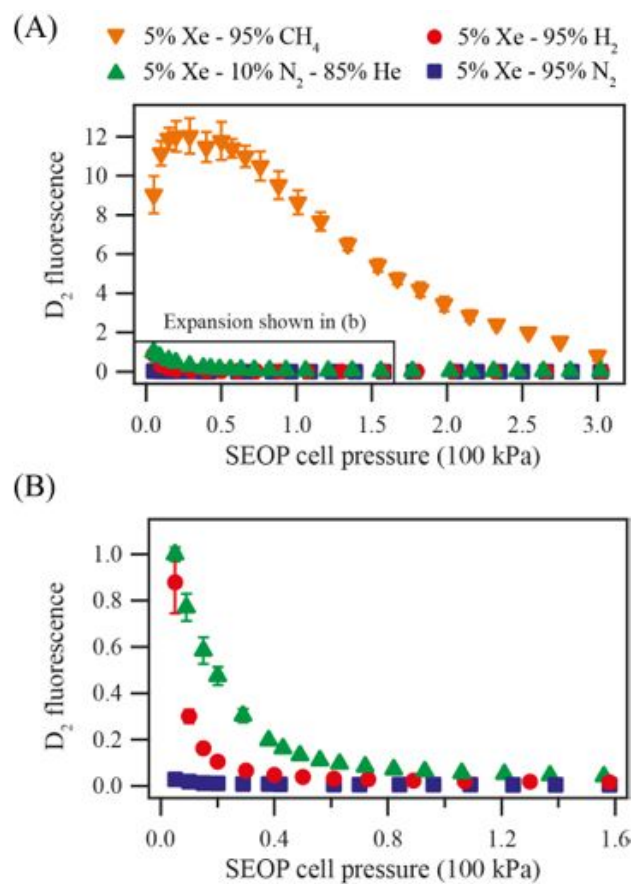


Figure. 6.4. D₂ fluorescence as a function of SEOP cell pressure for the mixtures detailed in the legend. (A) The full pressure range of curves, and (B) an expansion of the lower pressure and lower intensity regime. The fluorescence was normalized to the experimental value of the 5% xenon – 10% nitrogen – 85% helium mixture at 50 kPa.

Figure 6.4A displays the fluorescence corresponding to the spin polarization versus SEOP pressure curves shown in Figure 6.4. The fluorescence of the 5% xenon – 10% nitrogen – 85% helium standard mixture is included for comparison. As observed in Figure 6.4A, methane does not efficiently quench fluorescence contributing to the low polarization values seen in Figure 6.1 (also shown in Figure 6.3). Hydrogen, however, is a superior quenching agent as observed by the measured fluorescence. The hydrogen – xenon mixture displayed substantially less D_2 fluorescence for the mixture than the methane – xenon mixture. From the expansion of the data shown in Figure 6.4B the hydrogen – xenon mixture behaves similarly to the standard mixture that contains 10% molecular nitrogen.

The hydrogen – xenon system has been studied thoroughly as a function of mixture composition with results presented in Figure 6.5. In Figure 6.5A it is evident the increased xenon concentration reduces the overall polarization as seen previously with mixtures containing nitrogen in Chapter 3 (and ref. [19]). This reduction is caused by the increased relaxation due to the increased quantity of xenon at a given pressure.

In contrast to nitrogen – xenon data that reported an increase in spin polarization when pressure was reduced, the hydrogen – xenon mixtures did not exhibit this benefit. Although the spin polarization observed at 200 kPa is similar between the two mixtures, substantial differences occur at lower pressure. The likely reason is the increase in radiation trapping as observed by the D_2 fluorescence. Figure 6.5B shows the D_2 fluorescence for each mixture. The increase in radiation trapping limits the benefits of going to reduce pressure for SEOP of hydrogen – xenon mixtures.

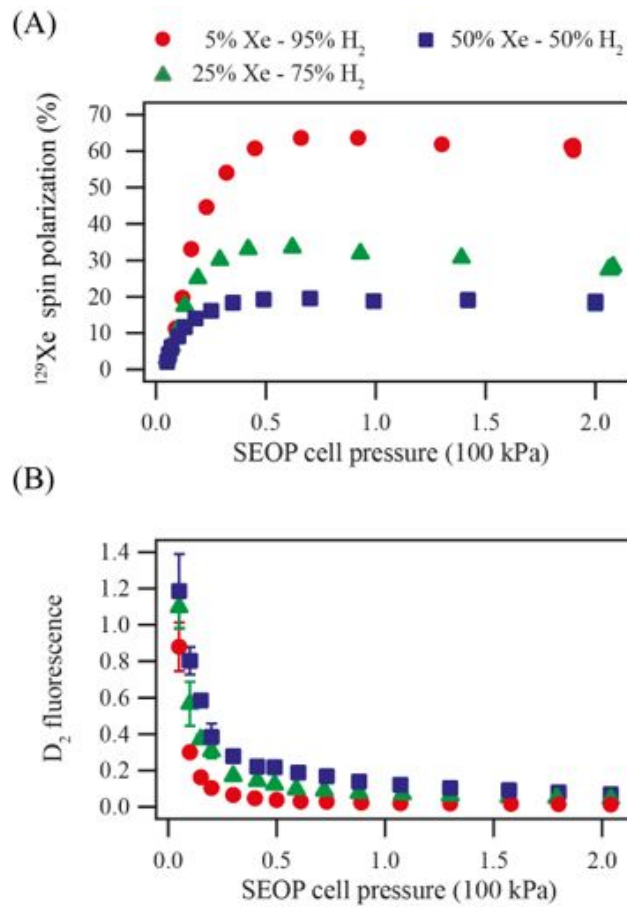


Figure 6.5. (A) ^{129}Xe spin polarization of three hydrogen – xenon mixtures (for details of mixture composition see legend) as a function of SEOP cell pressure. (B) Corresponding D_2 fluorescence as a function of SEOP cell pressure. The fluorescence data were normalized to the experimental value of the 5% xenon – 10% nitrogen – 85% helium mixture at 50 kPa.

6.3 *In situ* MRI of combustion

To permit combustion studies, continuous flow SEOP provided an uninterrupted source of hyperpolarized fuel-xenon mixtures. Continuous flow SEOP of the fuel – hyperpolarized xenon mixture negates cumbersome post SEOP mixing of the gases. For the continuous flow production in this

work, an SEOP pressure slightly above ambient was chosen to allow for the least demanding experimental conditions. As shown in Figure 6.1, ambient pressure SEOP of 5% xenon - 10% nitrogen - 85% methane obtains reasonable results at this pressure and this mixture was used for all MRI experiments in this work. SEOP at higher pressure would allow for the nitrogen concentration to be reduced further. Note that only xenon gas with natural abundance of 26.4% ^{129}Xe was used in this work.

Due to shorter residence time in the SEOP cell, the spin polarizations generated under continuous flow conditions are typically reduced compared to that obtained in batch mode SEOP shown in Figure 6.1. The reduction in spin polarization was amplified because the flow rates used in the experiments were optimized for combustion and not for the SEOP process. The polarization produced through the setup sketched in Figure 6.6 achieved a ^{129}Xe spin polarization of $P = 7\%$ for a flow rate of 40 mL/min and $P = 6\%$ for a flow rate of 15 mL/min.

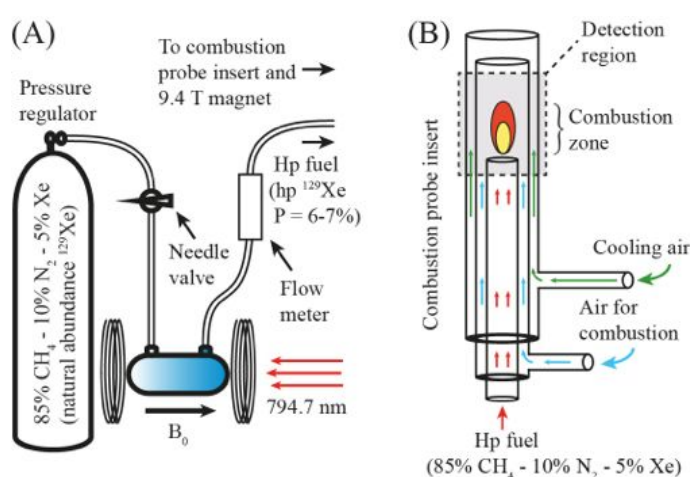


Figure 6.6. **(A)** Experimental setup for continuous flow SEOP. **(B)** Sketch of the combustion probe insert made of Pyrex and quartz. Reproduced from *Phys. Chem. Chem. Phys.*, 15, 2013, 94-7 with permission of the Royal Society of Chemistry.

The continuous flow setup, shown in Figure 6.6A, supplied an uninterrupted source of methane for combustion that contained hyperpolarized ^{129}Xe probe for MRI detection. The flow rates of the fuel mixture were regulated by a needle valve before the SEOP cell. In the SEOP cell hyperpolarization of ^{129}Xe is obtained via spin-exchange with laser pumped rubidium vapor as described in the previous section. The hyperpolarized ^{129}Xe gas mixture continuously exits the SEOP cell and the flow rate is measured before the mixture goes into the combustion probe placed in a 9.4 T superconducting magnet. The location of the flow meter at the exit of the SEOP cell was chosen in the interest of keeping cell contamination at a minimum. Losses in spin polarization due to the flow meter were deemed acceptable and are included in the polarization values reported in this work.

The combustion probe insert outlined in Figure 6.6B (15 mm outer diameter) was placed into a custom built bird-cage resonator probe head tuned to 110.69 MHz corresponding to the NMR frequency of ^{129}Xe at 9.4 T. The combustion probe insert was made of Pyrex except for the heat resistant quartz end piece of the hyperpolarized fuel delivery line. Air as an oxidation agent was delivered through a secondary tube surrounding the hyperpolarized fuel line. Cooling air, supplied by a third tube that enclosed both inner tubes, reduced the maximum wall temperatures of the insert to 313 K. Additional temperature insulation was provided by the spacing between the 15 mm outer diameter of the insert and the 25 mm inner diameter of the custom made micro-imaging probe. After passing the

magnetic resonance detection region, the hot combustion products were mixed with the cooling air and were exhausted through the vertical room temperature bore of the 9.4 T superconducting magnet (Bruker Avance III, MICRO 2.5) without any obstruction. Images were acquired with 90 degree pulses using 32 linearly ordered increments (maximum gradient 0.126 T/m) for a standard gradient echo imaging sequence with a read gradient of 0.084 T/m to form the gradient echo. For each increment 128 scans were collected resulting in a total image acquisition time of approximately 20 minutes.

Two different flame profiles were imaged: (1) a 'large' flame with a hyperpolarized mixture flow rate of 40 mL/min and an air flow rate of 600 mL/min; and (2) a 'small' flame with a hyperpolarized gas mixture flow rate of 15 mL/min and an air flow rate 400 mL/min. The resulting *in situ* hyperpolarized ^{129}Xe MRI of the hyperpolarized fuel mixtures after ignition are shown in Figures 6.7B and 6.7E (i.e. high and low flow respectively); for comparison, Figures 6.7A and 6.7D (i.e. high and low flow respectively) show *in situ* hyperpolarized ^{129}Xe MRI of the same flow rates but without ignition. Figures 6.7C and 6.7F show photographs of the respective flames. The hyperpolarized ^{129}Xe is seen strongly in the central channel where its density is the greatest before entering the combustion zone where the signal then diminishes as the hyperpolarized gas mixes with a high flow of air.

Although there is a decrease in the observed ^{129}Xe signal with ignition, it is apparent that the hyperpolarized state survived the harsh and reactive conditions of combustion. Furthermore, the reduction of the signal is partially caused by a decrease in gas density at the high combustion temperatures (i.e. > 1000 K, as opposed to 290 K without ignition).

Even with the reduction in density, substantial signal is observed in the flame and exhaust regions. To further verify the combustion resistance of the hyperpolarized nuclear spin state, the exhaust of the hyperpolarized fuel was collected after combustion through a glass syringe (i.e. with the combustor insert removed from the magnet for this purpose), injected into a sample container, and a one-dimensional NMR spectrum was taken that revealed considerable hyperpolarized ^{129}Xe polarization remained.

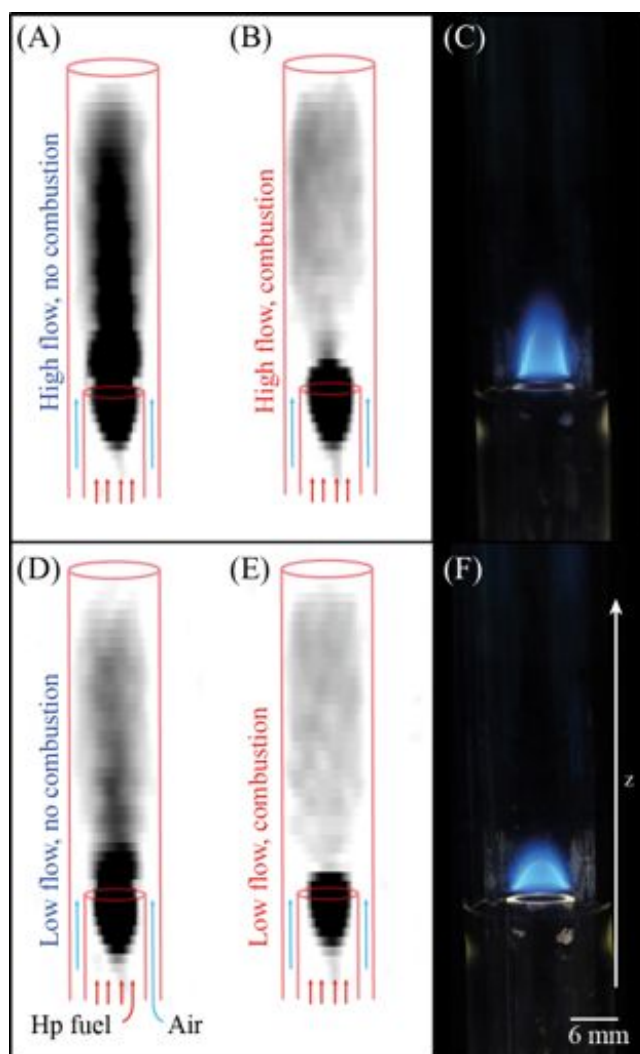


Figure 6.3. Hyperpolarized ^{129}Xe MRI of combustion using natural abundance xenon in methane. The upper portion displays images using the flow rates of the large flame (hyperpolarized fuel at 40 mL/min, air at 600 mL/min). **(A)** MRI of hyperpolarized ^{129}Xe mixture without ignition, **(B)** MRI of hyperpolarized ^{129}Xe with ignition, and **(C)** photograph of combustion in probe insert. The lower portion displays MR images using the flow rates of the small flame (hyperpolarized fuel at 15 mL/min, air at 400 mL/min). **(D)** MRI of hyperpolarized ^{129}Xe mixture without ignition, **(E)** MRI of hyperpolarized ^{129}Xe with ignition, and **(F)** photograph of combustion. An overlay of the approximate position of the combustion probe insert is provided in the MR images. Reproduced from *Phys. Chem. Chem. Phys.*, 15, **2013**, 94-7 with permission of the Royal Society of Chemistry.

The combustion resistance of the hyperpolarized state of the ^{129}Xe nuclear spins enables spatial-velocity measurements throughout the combustor. As a proof of principle, this work investigated velocities using the flow rates of the large flame in Figure 6.7. The methodology of acquiring spatial-velocity profiles of hyperpolarized ^{129}Xe was similar to that described in detail by Kaiser et al. [23] where the displacement of the gas was encoded. The sequence utilized 16 linearly incremented flow encoding gradients with $\delta = 0.3$ ms, and $\Delta = 1$ ms. The displacement encoding gradient was applied parallel to the spatial encoding gradient and the bulk flow gas (i.e. +z direction) in order to observe the substantial velocity increase of the gas due to combustion. The velocity in the +z direction was calculated from the displacement of the gas over time period $\Delta = 1$ ms. The gradient was chosen to correspond to a maximum velocity of 60 cm/s (determined during calibration experiments). Additional information about the combustion process can be extrapolated from the dispersion of gas perpendicular to the flow by changing the direction of the displacement encoding gradient; however, this was not attempted in this study. Unlike previous work [23], a stimulated echo was not employed because signal lost from transverse relaxation was acceptable in the short duration of Δ .

Figure 6.8 shows the velocity of ^{129}Xe in the z-axis (V_z , movement parallel to the direction of the bulk flow), as a function of z position. The relatively simple $V_z(z)$ profiles (i.e one spatial and one velocity dimension) demonstrate the drastic changes in velocity between non-ignited flow and combustion (see Figures 6.8A and 6.8B respectively).

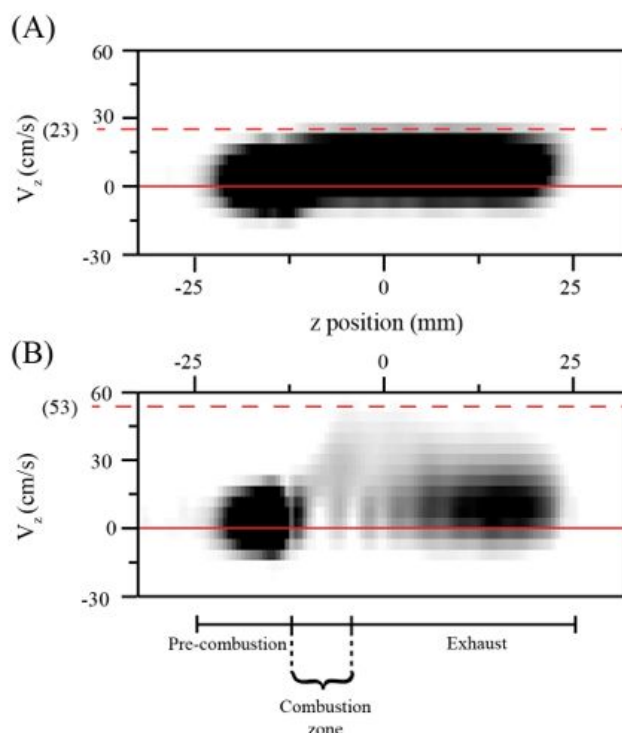


Figure 6.8. Hyperpolarized ^{129}Xe spatial-velocity profile displaying velocity V_z as a function of z position **(A)** without ignition and **(B)** with ignition. The pre-combustion, combustion, and exhaust regions are approximated. Reproduced from *Phys. Chem. Chem. Phys.*, 15, **2013**, 94-7 with permission of the Royal Society of Chemistry.

Figure 6.8A displays $V_z(z)$ without ignition of the hyperpolarized mixture. A maximum velocity of 18 cm/s is observed in the pre-combustion region. After mixing with the air the maximum velocity increases to 23 cm/s and then remains constant for the remainder of the detection region. Conversely, with ignition the velocity profile changes dramatically as seen in Figure 6.8B. The inlet region is nearly identical to the profile acquired without ignition. However, the maximum velocity near the combustion region is greatly increased to 53 cm/s. The maximum velocity then reduces with distance from the combustion zone. The greater distributions of velocities contribute to the apparent decrease in signal intensity. The gap of

observed signal at -13 cm is possibly an artefact arising from the migration of spins between flow encoding and spatial encoding, thus creating an error in the observed position. The $V_z(z)$ profile took less than 20 min to record and it should be possible to extend the measurement to complete flow field images. The MRI may be improved by utilization of fast imaging techniques such as SPRITE [8].

In conclusion, these data show the first *in situ* MRI of combustion by using hyperpolarized ^{129}Xe as a probe into the combustion process. These experiments were possible because of a novel approach to dope the fuel with hyperpolarized ^{129}Xe . Stopped flow experiments demonstrated that hyperpolarized ^{129}Xe was possible with methane present in the SEOP cell and generally high spin polarization can be obtained by the use of a ternary mixture that included molecular nitrogen. Additionally, hyperpolarization of ^{129}Xe in binary hydrogen – xenon mixtures resulted in high spin polarization values comparable with nitrogen – xenon mixtures. The ability to perform continuous flow SEOP with the fuel in the mixture simplifies the delivery of the hyperpolarized ^{129}Xe for prolonged MRI data acquisition.

The combustion resistance of the hyperpolarized ^{129}Xe nuclear spin state found in this work permits the collection of images that cover not only the pre-combustion region but also the combustion region and the exhaust. This work also demonstrated the feasibility of simple $V_z(z)$ spatial-velocity profiles covering the pre-combustion, combustion, and exhaust regions.

The preservation of the hyperpolarized nuclear spin state through the combustion process may allow for MRI to be used as an effective tool for investigating the fluid dynamics of combustion processes. Since the reaction

conditions in low temperature catalyzed reactions are milder than the open combustion used in this work, hyperpolarized ^{129}Xe MRI should be extendable to study heterogeneously catalyzed combustion [7]. Catalyzed combustion is used to avoid the build up of nitrogen oxides in gas powered turbines [24], allows for micro combustors [25], and can be used for example for the generation of synthetic fuels and selective partial combustion reactions [26]. Hyperpolarized ^{129}Xe MRI may be used for the study of flow fields within catalytic combustors and provide a better understanding of gas exchange with their porous surfaces [27]. Finally, as a cautionary note, the non-invasive nature of MRI for combustion within high magnetic fields remains unproven, in particular when fast moving ions are being generated.

6.4 References

- [1] K.F. Stupic, J.S. Six, M.D. Olsen, G.E. Pavlovskaya, T. Meersmann, Combustion resistance of the Xe-129 hyperpolarized nuclear spin state, *Phys. Chem. Chem. Phys.*, 15 (2013) 94-97.
- [2] P.M. Glover, B. Newling, C. Poirier, B.J. Balcom, A novel high temperature H-1 NMR imaging probe for combustion studies: The behaviour of both a lit and unlit methane gas jet, *Journal of Magnetic Resonance*, 176 (2005) 79-86.
- [3] J.P. Mustonen, H.D. Shin, D. Graziani, T. Theis, X. Zhou, V.S. Bajaj, A. Pines, CSI and Velocimetry of Enclosed Flames Using Hyperpolarized 129Xe, in: *EUROMAR 2011*, Frankfurt, 2011.
- [4] J.F. Stebbins, E. Schneider, J.B. Murdoch, A. Pines, I.S.E. Carmichael, New probe for high-temperature NMR spectroscopy with ppm resolution, *Review of Scientific Instruments*, 57 (1986) 39-42.
- [5] D. Massiot, D. Trumeau, B. Touzo, I. Farnan, J.C. Rifflet, A. Douy, J.P. Coutures, Structure and dynamics of CaAl₂O₄ from liquid to glass: a high-temperature Al-27 NMR time-resolved study, *Journal of Physical Chemistry*, 99 (1995) 16455-16459.
- [6] S. Anala, G.E. Pavlovskaya, P. Pichumani, T.J. Dieken, M.D. Olsen, T. Meersmann, In situ NMR spectroscopy of combustion, *Journal of the American Chemical Society*, 125 (2003) 13298-13302.
- [7] R.E. Hayes, S.T. Kolaczkowski, *Introduction to Catalytic Combustion.*, Gordon and Breach Science Publishers, Amsterdam, 1997.
- [8] B.J. Balcom, R.P. MacGregor, S.D. Beyea, D.P. Green, R.L. Armstrong, T.W. Bremner, Single-point ramped imaging with T-1 enhancement (SPRITE), *Journal of Magnetic Resonance Series A*, 123 (1996) 131-134.
- [9] D.E. Axelson, J.B. Wooten, Magnetic resonance imaging characterization of intact smoked cigarettes, *Journal of Analytical and Applied Pyrolysis*, 78 (2007) 214-227.
- [10] A. Dufour, M. Castro-Diaz, N. Brosse, M. Bouroukba, C. Snape, The Origin of Molecular Mobility During Biomass Pyrolysis as Revealed by In situ 1H NMR Spectroscopy, *Chemsuschem*, 5 (2012) 1258-1265.
- [11] D. Raftery, H. Long, T. Meersmann, P.J. Grandinetti, L. Reven, A. Pines, High-Field NMR of Adsorbed Xenon Polarized by Laser Pumping, *Phys. Rev. Lett.*, 66 (1991) 584-587.
- [12] M.G. Mortuza, S. Anala, G.E. Pavlovskaya, T.J. Dieken, T. Meersmann, Spin-exchange optical pumping of high-density xenon-129, *Journal of Chemical Physics*, 118 (2003) 1581-1584.
- [13] I.C. Ruset, S. Ketel, F.W. Hersman, Optical pumping system design for large production of hyperpolarized Xe-129, *Phys. Rev. Lett.*, 96 (2006) 053002.
- [14] E.S. Hrycyshyn, L. Krause, Inelastic Collisions between Excited Alkali Atoms and Molecules .7. Sensitized Fluorescence and Quenching in Mixtures of Rubidium with H₂, HD, N₂, CD₄, C₂H₂, and C₂H₆, *Canadian Journal of Physics*, 48 (1970) 2761-2768.

- [15] J.S. Six, T. Hughes-Riley, K.F. Stupic, G.E. Pavlovskaya, T. Meersmann, Pathway to cryogen free production of hyperpolarized krypton-83 and xenon-129, Plos One (in press), (2012).
- [16] N.D. Zamoski, W. Rudolph, G.D. Hager, D.A. Hostutler, A study of collisional quenching and radiation-trapping kinetics for Rb(5p) in the presence of methane and ethane using time-resolved fluorescence, Journal of Physics B-Atomic Molecular and Optical Physics, 42 (2009) 245401.
- [17] W. Happer, Optical-Pumping, Reviews of Modern Physics, 44 (1972) 169-249.
- [18] D.K. Walter, W.M. Griffith, W. Happer, Energy transport in high-density spin-exchange optical pumping cells, Phys. Rev. Lett., 86 (2001) 3264-3267.
- [19] J.S. Six, T. Hughes-Riley, K.F. Stupic, G.E. Pavlovskaya, T. Meersmann, Pathway to Cryogen Free Production of Hyperpolarized Krypton-83 and Xenon-129, PLOS ONE, 7 (2012) e49927.
- [20] W. Happer, G.D. Cates Jr, M.V. Romalis, C.J. Erickson, Alkali metal hybrid spin-exchange optical pumping, in, The Trustees of Princeton University, United States, 2001.
- [21] C.H. Volk, T.M. Kwon, J.G. Mark, Y.B. Kim, J.C. Woo, Measurement of the Rb-Xe-131 Spin-Exchange Cross-Section in Xe-131 Relaxation Studies, Phys. Rev. Lett., 44 (1980) 136-139.
- [22] J. Stenger, C. Grosshauser, W. Kilian, B. Ranzenberger, K. Rith, First experimental verification of spin temperature equilibrium in a high flow spin-exchange source for polarized hydrogen atoms, Phys. Rev. Lett., 78 (1997) 4177-4180.
- [23] L.G. Kaiser, J.W. Logan, T. Meersmann, A. Pines, Dynamic NMR microscopy of gas phase Poiseuille flow, Journal of Magnetic Resonance, 149 (2001) 144-148.
- [24] J.G. McCarty, Methane combustion - Durable catalysts for cleaner air, Nature, 403 (2000) 35-36.
- [25] C.M. Spadaccini, X. Zhang, C.P. Cadou, N. Miki, I.A. Waitz, Preliminary development of a hydrocarbon-fueled catalytic micro-combustor, Sensors and Actuators a-Physical, 103 (2003) 219-224.
- [26] S.M. Lang, T.M. Bernhardt, R.N. Barnett, U. Landman, Temperature-Tunable Selective Methane Catalysis on Au-2(+): From Cryogenic Partial Oxidation Yielding Formaldehyde to Cold Ethylene Production, Journal of Physical Chemistry C, 115 (2011) 6788-6795.
- [27] R.E. Hayes, S.T. Kolaczowski, P.K.C. Li, S. Awdry, The palladium catalysed oxidation of methane: reaction kinetics and the effect of diffusion barriers, Chemical Engineering Science, 56 (2001) 4815-4835.

Chapter 7: Conclusions

Techniques were developed for the production of hyperpolarized noble gases that have a nuclear electric quadrupolar moment. Nuclear isotopes possessing a nuclear electric quadrupolar moment cannot be easily separated from spin exchange optical pumping (SEOP) buffer gases using cryogenic accumulation, a process commonly performed for ^{129}Xe , due to rapid relaxation of the hyperpolarized spin state in the solid phase. This work developed a method that uses high noble gas concentration mixtures to decrease the need for cryogenic separation. These methods have also been found useful at producing hyperpolarized ^{129}Xe with great efficiency.

Low (below ambient) pressure SEOP of ^{83}Kr in a 5% krypton – 95% nitrogen mixture produced a maximum polarization of $P = 26.5\%$ at 54 kPa SEOP cell pressure using 23 W of laser power. The low partial pressure of krypton in the SEOP mixture resulted in an apparent polarization (i.e. the polarization accounting for dilution of buffer gases) of only 1.3%. A 25% krypton – 75% nitrogen mixture produced a lower maximum ^{83}Kr polarization of $P = 17.7\%$ but resulted in a higher apparent polarization of $P_{app} = 4.4\%$ because less dilution from nitrogen gas. Polarization values achieved in this work are currently the highest reported in literature for ^{83}Kr . Hyperpolarized ^{83}Kr with the maximum apparent polarization was produced at a rate of $2 \text{ cm}^3/\text{min}$. Low pressure spin exchange optical pumping

improved the hyperpolarization of ^{83}Kr in high krypton containing mixtures by reducing quadrupolar driven relaxation during the SEOP process. ^{83}Kr was the only quadrupolar isotope investigated in this work; however, the principles discussed in this thesis should benefit the production of hyperpolarized ^{21}Ne and ^{131}Xe .

In the case of ^{129}Xe , low pressure SEOP of a 5% xenon – 95% nitrogen mixture produced a maximum of $P = 64.7\%$ polarization at 46 kPa SEOP cell pressure using 23 W of laser power. A 50% xenon – 50% nitrogen mixture achieved the highest apparent polarization of $P_{app} = 15.5\%$ at 22 kPa SEOP pressure with production rate of $1.8 \text{ cm}^3/\text{min}$.

Current theory provided a qualitative understanding of the SEOP dependence of polarization on the gas pressure in the SEOP cell. Several simplifications and assumptions were required because of limited data in literature. The field would benefit from further systematic studies that determine physical parameters of the SEOP process. This work explored a new method to increase precision in extracting spin exchange optical pumping rates from build up curves by using an inversion recovery type of experiment where the circular polarization was reversed for a precisely timed recovery period.

The low pressure technique described in Chapter 3 (and ref. [1]) required development of hyperpolarized gas extraction-compression units to extract the below ambient pressure hyperpolarized gas in the SEOP cell and then compress this gas back to ambient pressure for use in pulmonary imaging. Development of extraction-compression strategies is detailed in ref. [2] and implemented to produce the first spatially resolved

demonstration of surface quadrupolar relaxation of ^{83}Kr in Chapter 4 (and ref. [3]). This methodology is also used to validate functional MRI of *ex vivo* rodent lungs using hyperpolarized ^{129}Xe published elsewhere [4] and a number of other studies currently in progress [5, 6]. The noble gas community as a whole may benefit from the proposed strategies, particularly the hyperpolarization of ^{129}Xe . To date, research into hyperpolarized ^{83}Kr is limited to the Translational Imaging Group of Thomas Meersmann at the University of Nottingham. However, the signal enhancement achieved by the low pressure ^{83}Kr SEOP technique permitted the first demonstration of surface quadrupolar relaxation pulmonary MRI which may cultivate further interest in this new contrast agent.

There are a number of future improvements that will benefit this low pressure technique. For example, an improved extraction unit made of glass instead of acrylic may help reduce longitudinal relaxation of ^{83}Kr during extraction and allow longer residence times in the unit, lessening the speed requirements for the transfer of gas. The delivery technique will also profit from computer automation that can help reduce variations between experiments, simplify image acquisition, and reduce the personnel required during experiments. Automation of the delivery process is in the early stages with preliminary programs written using LabVIEW (National Instruments, Austin, TX, USA).

Furthermore, the low pressure method produced only limited quantities of hyperpolarized gas suitable for the small inhalation volumes of *ex vivo* rat lungs. Greater quantities of hyperpolarized gas are needed for studies involving larger animal lungs. Increasing the SEOP cell size requires greater

laser power to maintain the current power density but this should not be a problem since 23 – 30 W were used in this work and much higher power lasers are readily available. Alternatively, multiple units can be run in parallel combining the gas in the extraction unit during the extraction process.

Optimised imaging strategies will improve the images using the current equipment and hyperpolarization methods described previously. An imaging sequence that uses compressed sensing has the potential to increase the image resolution keeping the current acquisition time or reduce acquisition time while maintaining current image resolution [7]. Compressed sensing may be useful for ^{83}Kr where imaging speed is imperative because of the short T_1 times in the lung. Compressed sensing may also improve SNR since fewer phase encoding steps uses a larger initial flip angle in the variable flip angle fast low angle shot (VFA FLASH) imaging sequence.

Alternatively, the long T_2 time of ^{83}Kr in *ex vivo* rat lungs values may permit imaging sequences based on echo planar imaging (EPI). EPI has the potential to increase the signal intensity by approximately a factor of five over the VFA FLASH since a full $\pi/2$ (90°) pulse is used for the EPI train in place of a small flip angle. Recent advancements in EPI strategies [8, 9] may further the potential of this technique by reducing commonly observed artefacts associated with EPI.

Future work involving ^{83}Kr will also benefit from the construction of an improved imaging coil. The double saddle coil used in the imaging experiments presented in this has poor sensitivity in the center of the coil (i.e. where the lung is placed during experiments). A quality built birdcage

coil or Litz coil [10] will improve the signal intensity and the quality of future ^{83}Kr images. However, size constraints in the 9.4 T vertical bore magnet may limit the feasibility of these options. Ideally a quality dual tuned coil would allow acquisition of high-resolution images of ^{129}Xe that then can be overlaid by an ^{83}Kr surface sensitive relaxation T_1 map that will register the ^{83}Kr data with the exact anatomical location without the need to change the coil.

The next experimental phase is to investigate the surface quadrupolar relaxation of ^{83}Kr pulmonary MRI in a diseased model of rat lungs. The first disease to examine is a model of emphysema where the surface to volume ratio inside the lungs is decreased from destruction to the alveoli architecture [11]. ^{83}Kr surface quadrupolar relaxation may observe the changes in surface to volume ratio in the lung caused by the disease due to less interaction with the surface. A pilot study is currently underway [12] in collaboration with Mark Birrell and Maria Belvisi from Imperial College London using an elastase model [13] of emphysema.

A necessary advancement will be to demonstrate surface quadrupolar relaxation of hyperpolarized ^{83}Kr pulmonary MRI *in vivo*. The initial steps towards this experiment have begun with the construction of a new noble gas hyperpolarizer that will be installed in the Brain and Body Centre at the University of Nottingham in the near future. This hyperpolarizer was designed by Karl F. Stupic, David M.L. Lilburn and Joseph S. Six and assembled by David M.L. Lilburn and Joseph S. Six. University of Nottingham machinist Alan Dorkes has fabricated many of the components for the hyperpolarizer.

A method was developed to determine internal magnetic field gradients in model systems from diffusion dependent transverse relaxation of ^{129}Xe . Unfortunately the method must allow for large changes in pressure and is not suitable for experiments that require isobaric conditions such as pulmonary NMR spectroscopy or imaging. In the model porous system the transverse relaxation was strongly dependent on the pore size. Additionally, internal magnetic field gradients were found unchanged by surface chemistry of glass beads. The insensitivity of transverse relaxation on the surface coating may provide a pathway to determine origins of ^{83}Kr longitudinal relaxation.

Overall the work presented in this document has shown a large step towards developing hyperpolarized ^{83}Kr as an MRI contrast agent for pulmonary studies. Hyperpolarized ^{83}Kr MRI is unlikely to match the signal intensity, and therefore resolution, of current ^3He and ^{129}Xe images because of quadrupolar relaxation limits the achievable polarization. However, with the signal enhancement achieved in this work, hyperpolarized ^{83}Kr may serve as a contrast agent that can investigate the surfaces of the lung in a manner unavailable for ^3He and ^{129}Xe because of the potential for surface quadrupolar relaxation MRI.

An SEOP technique was also developed that hyperpolarized ^{129}Xe as part of fuel mixture and permitted the first *in situ* MRI of combustion. ^{129}Xe was hyperpolarized in a fuel mixture containing either methane or hydrogen providing a continuous source of hyperpolarized fuel for combustion. It was found that the hyperpolarized spin state of ^{129}Xe survived the combustion zone enabling the acquisition of spatial-velocity profiles to characterize the flame. This technique may be extended to study flow in catalytic

combustors. The combustion experiments focused on ^{129}Xe , but of the concepts from the combustion study will be expanded to isotopes with a nuclear electric quadrupole moment in the near future.

7.1 References

- [1] J.S. Six, T. Hughes-Riley, K.F. Stupic, G.E. Pavlovskaya, T. Meersmann, Pathway to Cryogen Free Production of Hyperpolarized Krypton-83 and Xenon-129, *PLOS ONE*, 7 (2012) e49927.
- [2] T. Hughes-Riley, J.S. Six, D.M.L. Lilburn, K.F. Stupic, A.C. Dorkes, D.E. Shaw, G.E. Pavlovskaya, T. Meersmann, Cryogenics free production of hyperpolarized ^{129}Xe and ^{83}Kr for biomedical MRI applications, *Journal of Magnetic Resonance*, 237 (2013) 23-33.
- [3] J.S. Six, T. Hughes-Riley, D.M.L. Lilburn, K.F. Stupic, D.E. Shaw, P. Morris, I. Hall, G.E. Pavlovskaya, T. Meersmann, Lung surface sensitive MRI contrast using hyperpolarized ^{83}Kr MRI, (2013).
- [4] D.M.L. Lilburn, T. Hughes-Riley, J.S. Six, K.F. Stupic, D.E. Shaw, G.E. Pavlovskaya, T. Meersmann, Validating Excised Rodent Lungs for Functional Hyperpolarized Xenon-129 MRI, *PLoS ONE*, 8 (2013) e73468.
- [5] D.M.L. Lilburn, A. Tatler, J.S. Six, C. Lesbats, D.E. Shaw, G. Jenkins, T. Meersmann, Evaluation of ovalbumin induced asthma in ex vivo rat lungs using hyperpolarized ^{129}Xe , University of Nottingham, Unpublished work, Nottingham, UK, 2013.
- [6] D.M.L. Lilburn, A. Habgood, A. Tatler, C. Lesbats, J.S. Six, D.E. Shaw, G. Jenkins, G.E. Pavlovskaya, T. Meersmann, Investigation of idiopathic pulmonary fibrosis in ex vivo rat lungs using hyperpolarized ^{129}Xe and ^{83}Kr , University of Nottingham, Unpublished work, Nottingham, UK, 2013.
- [7] S. Ajraoui, K.J. Lee, M.H. Deppe, S.R. Parnell, J. Parra-Robles, J.M. Wild, Compressed Sensing in Hyperpolarized (^3He) Lung MRI, *Magn. Reson. Med.*, 63 (2010) 1059-1069.
- [8] N. Ben-Eliezer, Y. Shrot, L. Frydman, High-definition, single-scan 2D MRI in inhomogeneous fields using spatial encoding methods, *Magnetic Resonance Imaging*, 28 (2010) 77-86.
- [9] N. Ben-Eliezer, M. Irani, L. Frydman, Super-resolved spatially encoded single-scan 2D MRI, *Magn. Reson. Med.*, 63 (2010) 1594-1600.
- [10] F. David Doty, G. Entzminger, Litz Coils for High Resolution and Animal Probes, Especially for Double Resonance, in: *eMagRes*, John Wiley & Sons, Ltd, 2007.
- [11] W.M. Thurlbeck, Internal Surface Area and Other Measurements in Emphysema, *Thorax*, 22 (1967) 483-496.
- [12] D.M.L. Lilburn, J.S. Six, C. Lesbats, T. Hughes-Riley, D.E. Shaw, G.E. Pavlovskaya, M.G. Belvisi, M.A. Birrell, T. Meersmann, MRI of hyperpolarized ^{83}Kr surface quadrupolar relaxation in an ex vivo model of emphysema, University of Nottingham, Unpublished work, Nottingham, UK, 2013.
- [13] M.A. Birrell, S. Wong, D.J. Hele, K. McCluskie, E. Hardaker, M.G. Belvisi, Steroid-resistant inflammation in a rat model of chronic obstructive pulmonary disease is associated with a lack of nuclear factor-kappa B pathway activation, *American Journal of Respiratory and Critical Care Medicine*, 172 (2005) 74-84.